FINAL TECHNICAL REPORT
May 7, 2010 to August 28, 2015

Chemical Process Alternatives for Radioactive Waste

Date submitted:

August 28, 2015

Principal Investigator:

Leonel E. Lagos, Ph.D., PMP®

Florida International University Collaborators:

Dwayne McDaniel, Ph.D., P.E. (Project Manager)
Amer Awwad, M.S., P.E.
Seckin Gokaltun, Ph.D.
Romani Patel, M.S.
Tomas Pribanic, M.S., P.E.
David Roelant, Ph.D.
Jario Crespo
Georgio Tachiev, Ph.D., P.E.
Jose Varona, M.S.
Anthony Abrahao, M.S.
Hadi Ferkmanidi, Ph.D.
Aparna Aravelli
DOE Fellows

Prepared for:

U.S. Department of Energy
Office of Environmental Management
Under Cooperative Agreement DE-EM00000598

FIU | Applied Research Center
Florida International University

FIU STUDENTS DIRECTLY SUPPORTING DOE EM PROJECTS

DOE Fellows from the DOE-FIU Science & Technology Workforce Development Program as well as FIU Graduate Research Assistants provide direct support to DOE EM projects around the complex. The following DOE Fellows and FIU Graduate Research Assistants supported the high-level waste research tasks for the Hanford Site under FIU Project 1:

DOE Fellows: Anthony Fernandez, John Conley
Mentors: Amer Awwad, Jairo Crespo
Project Task: Development of Alternative Unplugging Technologies

DOE Fellows: John Conley, Anthony Fernandez
Mentors: Amer Awwad, Dwayne McDaniel
Project Task: Evaluation of Nonmetallic Components in the Waste Transfer System

DOE Fellow: Dayron Chigin
Mentors: David Roelant, Dwayne McDaniel
Project Task: Evaluation of FIU's SLIM for Rapid Measurement of HLW Solids on Tank Bottoms

DOE Fellow: Deanna Moya
Mentor: Romani Patel
Project Task: Computational Simulation and Evolution of HLW Pipeline Plugs

DOE Fellow: Brian Castillo
Mentors: Dwayne McDaniel, Aparna Aravalli
Project Task: Pipeline Corrosion and Erosion Evaluation

DOE Fellow: Ryan Sheffield
Mentors: Dwayne McDaniel, Hadi Fekrmandi
Project Task: Development of Inspection Tools for DST Primary Tanks

DOE Fellows: Michael Abbott, Sasha Philius, Maximiliano Edrei
Mentor: Seckin Gokaltun
Project Task: Computational Fluid Dynamics Modeling of HLW Processes in Waste Tanks

A complete list of DOE Fellows supporting the DOE EM research efforts can be found in the Year End Report for Project 5, section 8, "DOE Fellows Directly Supporting DOE EM Projects" on pages 57-58.

Addendum:

This document represents one (1) of five (5) reports that comprise the Final Technical Reports for the period of May 18, 2014 to August 28, 2015 (FIU Year 5) prepared by the Applied Research Center at Florida International University for the U.S. Department of Energy Office of Environmental Management (DOE-EM) under Cooperative Agreement No. DE-EM0000598. A summary of FIU Year 1 to FIU Year 4 (May 7, 2010 to May 17, 2014) is also included.

The complete set of FIU's Final Technical Reports for this reporting period includes the following documents and is available at the DOE Research website for the Cooperative Agreement between the U.S. Department of Energy Office of Environmental Management and the Applied Research Center at Florida International University (http://doeresearch.fiu.edu):

Project 1: Chemical Process Alternatives for Radioactive Waste
Document number: FIU-ARC-2015-800000393-04b-237

Project 2: Rapid Deployment of Engineered Solutions for Environmental Problems
Document number: FIU-ARC-2015-800000438-04b-228

Project 3: Remediation and Treatment Technology Development and Support
Document number: FIU-ARC-2015-800000439-04b-232

Project 4: Waste and D&D Engineering and Technology Development
Document number: FIU-ARC-2015-800000440-04b-229

Project 5: DOE-FIU Science & Technology Workforce Development Initiative
Document number: FIU-ARC-2015-800000394-04b-090

Each document will be submitted to OSTI separately under the respective project title and document number as shown above.

TABLE OF CONTENTS

LIST OF FIGURES

LIST OF TABLES

PROJECT 1 OVERVIEW

The Department of Energy's (DOE's) Office of Environmental Management (EM) has a mission to clean up the contaminated soils, groundwater, buildings and wastes generated over the past 60 years by the R&D and production of nuclear weapons. The nation's nuclear weapons complex generated complex radioactive and chemical wastes. This project is focused on tasks to support the safe and effective storage, retrieval and treatment of high-level waste (HLW) from tanks at Hanford and Savannah River sites. The objective of this project is to provide the sites with modeling, pilot-scale studies on simulated wastes, technology assessment and testing, and technology development to support critical issues related to HLW retrieval and processing. Florida International University (FIU) engineers work directly with site engineers to plan, execute and analyze results of applied research and development.

Although a number of tasks have been initiated and completed over the course of the 5 year reporting period, at the end of FIU Year 5 (FY14), there were 7 active tasks/subtasks. These tasks are listed below and this report contains a detailed summary of the work accomplished for FIU Year 5 (FY14). All research conducted prior to FY14 is summarized for each task for the relevant years.

Task 2.1 – Asynchronous Pulsing System: The objective of this task is to complete the experimental testing of the asynchronous pulsing system and position the technology for future deployment at DOE sites. Extensive experimental testing has been conducted on bench-scale as well as engineering-scale test beds. Future efforts will be defined by site engineers with tasks that lead to the deployment of the technology.

Task 2.2 – Computational Simulation and Evolution of HLW Pipeline Plugs: The objective of this task is to utilize computational fluid dynamics (CFD) software to simulate the formation of plugs in HLW pipelines. Research efforts focus on understanding how pipeline geometry including elbows, tees and reducers can affect the formation of plugs.

Task 17.2 – CFD Modeling of HLW Processes in Waste Tanks: The objective of this task is to provide the sites with mathematical modeling, validation, and testing of computer programs to support critical issues related to HLW retrieval and processing. Specifically, FIU is developing a CFD model based on the Star-CCM+ framework to simulate the turbulent jet-flow in non-Newtonian fluids that show Bingham plastic behavior.

Task 18.1 – Evaluation of FIU's Solid-Liquid Interface Monitor (SLIM) for Rapid Measurement of HLW Solids on Tank Bottoms: The objective is this task is to evaluate the SLIM for its ability to rapidly image and quantify HLW solids left at the bottom of mixing tanks in small regions of interest while solids are being mixed inside these tanks. Pilot-scale testing will be performed to determine the system's ability to image solids in short time periods during a single pulse jet mixing cycle.

Task 18.2 – Development of Inspection Tools for DST Primary Tanks: The objective of this task is to develop inspection tools that will assist engineers in identifying the location of leaks in the AY-102 double-shell tank at the Hanford Site. The effort led to the development of two inspection tools, both able to provide live visual feedback: a magnetic wheeled miniature motorized rover that will travel through the refractory cooling channels under the primary tank, and a pneumatic pipe crawler that will inspect the tank ventilation header pipes.

Task 19.1 – Pipeline Erosion and Corrosion Evaluation: The objective of this task is to provide the sites with analysis of data obtained from primary and secondary pipelines as well as components in jumper pits, evaporators, and valve boxes. Information regarding the initial and current thickness for various components was obtained, in addition to transfer history, and wear rates were determined.

Task 19.2 – Evaluation of Non-metallic Components in the Waste Transfer System: The objective of this task is to provide the Hanford Site with data obtained from experimental testing of the hose-in-hose transfer lines, Teflon® gaskets, EPDM O-rings, and other nonmetallic components used in their tank farm waste transfer system under simultaneous stressor exposures. The stressor exposure experiments will be limited to various combinations of simultaneous stressor exposures of caustic solutions, high temperatures and high pressure. Evaluation of baseline materials will be conducted and compared with materials that have been conditioned with the various stressors.

TECHNICAL PROGRESS FROM FIU YEAR 1 to FIU YEAR 4

TASK 2 SUMMARY – PIPELINE UNPLUGGING AND PLUG PREVENTION (FIU YEAR 1 TO FIU YEAR 4)

In previous years, Florida International University (FIU) has tested and evaluated a number of commercially available pipeline unplugging technologies. Two of the more promising technologies (AIMM Technologies' Hydrokinetic Method and NuVision's wave erosion technology) were further evaluated and found to have shortcomings associated with their processes. Based on the lessons learned from the evaluation of the technologies, two alternative approaches were proposed by FIU. These are an asynchronous pulsing system (APS) and a peristaltic crawler. The APS is based on the principle of creating pressure waves in the pipeline filled with water from both ends of the blocked section in order to break the bonds of the blocking material with the pipe wall via forces created by the pressure waves. The waves are created asynchronously in order to shake the blockage as a result of the unsteady forces created by the waves. The peristaltic crawler is a pneumatically operated crawler that propels itself by a sequence of pressurization/depressurization of cavities (inner tubes). The changes in pressure result in the translation of the vessel by peristaltic movements. This section summaries research conducted on the APS and peristaltic crawler. An additional effort was incorporated into the task which focused on the simulation of the formation of plugs using multi-physics computer software. This section also has a brief summary of this research effort.

Asynchronous Pulsing System

In FIU Year 1, the first phase of the experimental testing of the APS was conducted. The infrastructure that includes the pulse generation unit, initial testbed, instrumentation, and data acquisition unit was developed and assembled. The hydraulic powered pulse generation unit was designed and procured having a maximum pulsing frequency of 20 Hz. The software required to control the unit was developed, allowing for the generation of pressure pulse waves having a sinusoidal or square profile. The initial testbed consisted of a 40-ft 3-in-diameter pipeline having a solid aluminum cylinder in the middle to emulate a plug. Each side of the pipeline consists of two 10-ft sections with a 90° elbow. The pipeline is heavily instrumented with pressure transducers, accelerometers and thermocouples to capture the changes resulting from the pressure pulses generated. Tests were performed for pulse frequencies ranging from 0.125 Hz to 10 Hz. Results show clear asynchronous pressures at each of the sides of the aluminum cylinder for frequencies lower than 2 Hz. Results were inconclusive for higher frequencies.

Using the capability of the pulse generation unit, a second set of tests was conducted in an attempt to resonate the water column. These tests were carried out using half of the testbed. The frequencies generated ranged from 2 Hz to 20 Hz. To evaluate the effect of the air in the pipeline, the pipeline was tested with 100% water and also for 87.5% and 75% water to air. Only trials with the hydraulic oil set to 300 psi and 25% air demonstrated a significant increase in vibration response. This occurred at the 2-6 Hz range.

In FIU Year 2, experiments were conducted to validate the APS's ability to unplug a small-scale pipeline testbed and to compare its performance to the data obtained from a CFD model developed for the system. The unplugging experiments consisted of placement of K-mag based plugs within a test pipeline loop and using the system to unplug the pipeline. The results obtained during the experimental phase included pressures and vibration measurements that capture the propagation of the pulses generated by the system.

The pulse-loop response verification testing phase compared the performance of the APS to the data obtained from a CFD model developed for the system. The model predicts resulting pressure amplification as a response to a single step pulse input, with the amplification contingent on the pipeline length and geometry. These tests evaluated a single-cycle pulse amplification caused by various piston pump drive pressures, drive times, and drive profiles.

In FIU Years 3 and 4, experiments were conducted to validate the APS's ability to unplug a large-scale pipeline testbed and compare the performance of the APS to the data obtained from the testing conducted on small-scale testbeds. The unplugging experiments consisted of placement of 3-ft kaolin-plaster plugs within a test pipeline loop which consists of two 135-foot runs on either side of a plug and using the system to unplug the pipeline. The pipelines were instrumented with accelerometers and pressure transducers that can capture vibration and pressure data in the pipeline. Various conditions within the pipeline were evaluated including lines with and without entrained air. Studies were conducted prior to the engineering scale testing to determine how air entrainment can be mitigated. For the engineering scale testing, parametric trials were conducted using an exemplar plug to determine the effects of varying static pressure, amplitude of the pulse pressure and pulse frequency. Research efforts also focused on manufacturing a plug that had the necessary material characteristics and could not be removed with static pressures less than 300 psi. Unplugging trials were conducted based on the results obtained from the parametric testing. Trials included using sine, triangle and saw tooth wave types as well as pulse frequencies of 1, 2 and 3 Hz under a static pressure of 50 psi. A successful unplugging was obtained during each trial.

Peristaltic Crawler

In FIU year 1, a second generation peristaltic crawler was designed, assembled and experimentally tested, building on an initial crawler that was built as a proof-of-concept. Improvements on the materials and design of the unit were implemented to improve its durability and maximum pressure rating. Edge-welded and hydro-formed stainless steel bellows were evaluated and tested. Improvements on the front and back cavities were also developed to minimize possible leaks and increase the anchoring force of the crawler to the pipeline. The control systems for the crawler were automated to provide a joystick controlled forward and backward motion. Experimental testing of the crawler included a speed test, yielding a maximum speed of 0.5 ft/min. The maneuverability test indicated that the crawler was able to navigate through a 90° PVC elbow having a radius of 5.56 inches in a time of approximately 7.5 minutes. The maximum pulling force achieved by the crawler was 110 lb of force when providing 90 psi of pressure to the bellow. Two high pressure water nozzles were used to test the crawler's unplugging ability: 1) a rotating nozzle and 2) a 15° nozzle. Results demonstrated that the 15° nozzle provided the most effective unplugging effect on clay and salt based plugs.

In FIU Year 2, efforts focused on implementing improvements to the crawler design based on previous bench-scale testing. Improvements included the reduction of the crawler's outer diameter and the use of an edge-welded bellow in the body assembly. The crawler was re-manufactured and tested to determine its navigational capability and pipeline unplugging effectiveness. Other improvements included the design and testing of a 500-ft multi-line tether assembly, design and procurement of a tether-reel system and evaluation of an on-board control valve system. Experimental testing of the new design included two speed tests, one using a 15-foot tether and the other using a 500-ft tether. The tests demonstrated a maximum speed of 21 ft/hour for the 15-foot tether and 1 ft/hour for the 500-foot tether. Maneuverability tests indicated that the crawler was able to navigate through a 90° elbow in a time lapse of 11 minutes and 23 seconds. The maximum pulling force achieved by the crawler was 133 lbs of force when providing 60 psi of pressure to the bellow assembly.

In the following year, design improvements were implemented to increase the navigational speed of the crawler which included relocation of the pneumatic valves from the control box to a trailing capsule 1 ft from the rear of the crawler and the replacement of the outer bellow with a thinner wall bellow of similar dimensions. These changes improved the speed of the crawler from 1 ft/hr to 38 ft/hr. Bench scale navigational tests conducted using a 90° elbow showed a time of 11 min for the crawler to clear the elbow. Pull force tests demonstrated that the crawler could create a maximum pulling force of 108 lb with a supply pressure of 50 psi. An engineering scale testbed, with a total length of 430 ft, was also assembled and navigational tests were conducted. During testing, it was observed that the inner diameter of schedule 10 pipe sections caused the flexible cavities of the crawler to over expand, resulting in a drastic decrease of the fatigue life of the cavities. Options to increase the fatigue life of the cavities were evaluated and it was found that increasing the distance between the clamps to 1 inch provided a total of 15,000 cycles prior to failure. It was estimated that a total of approximately 3,600 cycles was required for the crawler to completely navigate the 430 ft testbed. Pull force tests conducted by manually routing the tether through the pipeline showed that a force of 8 lb is required for every 21 ft straight section of pipeline after the first 21 ft section. A stainless steel wire was then wound around the tether to decrease the friction force and contact area between the tether and the pipeline.

In FIU Year 4, efforts also focused on the continuation of the engineering-scale testing of the peristaltic crawler. The previous year testing demonstrated that the front and rear cavities of the crawler had unforeseen durability issues. After conducting fatigue tests on the cavities, it was determined that stress risers around the circumference of the clamps caused the cavity material to rupture prematurely. A number of design options were considered and the design was improved to have a 1-inch distance between the clamps to provide more material available for expansion.

Manual tether pull tests were conducted to determine the axial load requirements on the unit as the tether length increased and as friction resistance increased with the addition of 90° elbows. In order to reduce the frictional force (axial load), the pipeline was flooded with water. After flooding the pipeline, the maximum axial force requirement after the second elbow was reduced to approximately 45 lb. Using the information from the tether load tests, the crawler’s response to axial loads was evaluated using a pulley-weight system. The largest load recorded was 25 lb with a maximum speed of 6.05 ft/hr. Other improvements included the addition of a ring on the bellow to aid the crawler’s navigation through elbows. Navigational tests continued to have durability issues associated with the pneumatic lines and cavities. Premature failure of the cavities was likely caused by stress risers resulting from the axial deflection of the rubber material as the axial load increased. Alternative designs to improve the durability of the cavities need to be investigated.

Computational Simulation and Evolution of HLW Pipeline Plugs

Pipeline plug formation is caused by changes in the chemistry and flow patterns within the pipe transfer system at Hanford. A better understating of the interactions between the chemical species leading to precipitate formation is required to reduce the risk of pipe plugging. A need exists for a computational tool that can predict plug formation by considering the chemistry dynamics coupled with fluid particle interactions. The use of computational fluid dynamics (CFD) software has been explored in the past to predict plug formation based on the settling of solids. Even though the efforts were promising, the models lacked incorporation of chemical reactions kinetics. Hence, a new task was initiated as part of FIU's research efforts to develop a multi-physics model using CFD software that could simulate the coupled flow and chemistry kinetics and aid in understanding the plug formation process. In particular, how the process is affected by pipeline geometry.

A literature review was conducted using major search engines to advance the plug formation knowledgebase, with specific applications to the Hanford Site. The review focused on four areas: (i) Overview of the waste transfer system at Hanford, (ii) Plugging mechanisms and waste transfer dynamics, (iii) Current analysis tools-capabilities and limitations, and (iv) Use of CFD modeling to predict the plug formation process.

The simulation of the plug formation process requires solving the coupled equations of flow and transport. Three interfaces were used to facilitate this: 1) flow interface, 2) chemical reaction interface and 3) mixture interface. The flow interface was used to simulate flow fields along the pipe length. The transport of chemical reactions interface was used to model multicomponent transport and evolution of chemical reaction between multiple species ($A+B \rightarrow C$). The mixture interface was used to investigate multiphase interactions and solids growth in a pipeline was modeled.

During FIU Year 4, several virtual scenarios representing multi-phase flow conditions in a pipe were simulated to study the settling dynamics in a pipeline. A parametric analysis was carried out, simulating settling of solids as a function of flow velocity, particle size, solids density and volume fraction of solids. The results were validated by experimental results and critical velocity correlations. The modeling efforts within the multi-phase domain were also directed towards the simulation of precipitation kinetics such as solids growth in the plug formation process. A conceptual model was proposed and efforts continued to investigate the ability of Comsol to model the precipitation events.

TASK 15 SUMMARY - EVALUATION OF ADVANCED INSTRUMENTATION NEEDS FOR HLW RETRIEVAL (FIU YEAR 2 TO FIU YEAR 4)

As the DOE's Hanford Site begins preparations for the transfer of high-level waste (HLW) from double-shell tanks (DST) to the Waste Treatment and Immobilization Plant (WTP), the influence of waste feed consistency on the final stabilized waste form is currently under analysis. In order to characterize feed consistency, a suite of instrumentation will be required to monitor the waste preparation and mixing process in real time. FIU has focused its instrumentation efforts during this performance period on the improvement of *in situ*, near-real time monitoring of the mixing process. This task worked with personnel responsible for the preparation of waste feed into the WTP in identifying innovative technologies applicable for in-tank monitoring during the mixing process.

This task began with a review of the current state of technology applicable to the monitoring of HLW feed during the mixing and transfer process. The review examined the previous works by PNNL, the site contractors, and academia in identifying and implementing technologies that can monitor critical physical and rheological parameters of the waste. Discussions with site representatives established the current technology implementation plan for the double-shell tanks that will be used to stage waste feed for WTP; these discussions were also a reference to minimize duplicative efforts into areas that had already been evaluated by other parties.

After the current technology baseline plan and previous research efforts were reviewed, FIU began an extensive literature and technology search for applicable systems that could provide waste parameters within the HLW tank environment. The literature search focused on available methodologies for *in situ* analysis of slurries, emulsions and suspensions applied in all industries. In particular, the monitoring of bulk density and/or particle concentration/characteristics measurements was the focus of the search. For the technology search, vendors of applicable techniques were identified and contacted. The searches resulted in several academic, commercial and governmental reports/articles applicable to the monitoring needs of the HLW tanks. Instrumentation specifications were collected and reviewed to identify the technology capabilities and limitations. These capabilities were also used for a comparative analysis between technologies. Based on the information, all the technologies were down selected to five applicable systems/methods that could provide useful information if deployed in a HLW tank. The five applicable methods applicable to the *in situ* monitoring of the waste feed consistency were focused beam reflectance measurement (FBRM), optical back-reflectance measurement (ORM), ultrasonic spectroscopy (USS), Lamb/Stoneley wave viscosity measurement, and vibration-based densitometers. Based on the literature results and commercial options, the ultrasonic and vibration-based techniques showed the most promise for developing a technology that could be used for *in situ* measurements within the aggressive environment of a HLW tank. Specifically, the vibration-based and USS systems can provide information on the density and concentrations of the mixed slurry. These techniques can be engineered for monitoring at various depths within the tank.

Once the most promising techniques were selected, an experimental approach was defined. The approach would look at technology monitoring limitations in two phases; phase I would determine how the technologies could measure the slurry parameter, and how that measurement compared to laboratory or baseline techniques. This phase would be used as a go/no-go point to determine if further investigation into the technology is warranted. The second phase would focus on which specific factors and interactions would influence the measurement (particle size, carrier fluid density, etc). The USS would be compared to a commercially available density meter that utilizes an accurate and repeatable technique for density measurement. A setup was conceived that allowed the testing of the USS and a commercially-available Coriolis mass flow meter side-by-side. The setup used a 10-gallon tank for agitation of the simulated slurry mixtures, with both systems sampling at the same location; the USS system probe was lowered into the tank, while a pick-up tube was used to transfer mixture to the Coriolis meter. In addition, the USS was subjected to several tests using a benchtop setup for more controlled evaluations of its concentration tracking capabilities. Both these systems were subjected to solutions and suspensions that would simulate the extreme bounds of the physical and rheological properties of the HLW slurry found in AZ-102. The simulated slurries consisted of one to three distinct solids suspended in a water or $NaNO_3$ solution as the supernatant.

The USS system was installed, and training performed by ITS. The system had several technical issues at the outset, particularly relating to the software performance. The USS was subjected to concentration ladders of solid $Al(OH)_3$ in an ultrapure reverse osmosis/de-ionized water supernatant to evaluate its ability to tracks changes in concentration in a suspension. Several of the tests determined that software issues were calculating incorrect values for the separation and delay in the time-of-flight measurements, giving large errors in ultrasonic group velocity measurement. The technical issues delayed the completion of this phase.

The system was subsequently returned to the vendor as a result of a hardware fault. A new system was sent to FIU and was used to complete testing. The results indicate that the technology can provide a measurement of density, but the frequency at which it occurs varies with slurry characteristics. If one frequency is selected for analysis, the density values vary more than 10% when compared to the reference value. One major issue that occurred during testing was that the spectral response profile of the USS system changed between hardware changes, and this was something that the vendor attributed to an issue with the reference file used for the tests.

In order to address issues with system inconsistency, additional bench-scale tests were prepared at ITS facilities during the first quarter of FY12. The testing utilized similar materials, concentration profiles for $NaNO_3$ and solids loading profiles in an attempt to determine the root cause for the inconsistency of results, as well as to compare the results to the FIU data. The USS utilized consisted of a through-transmission configuration, which had a slightly larger transducer than those tested at FIU. The ITS test results indicated good agreement between the measured and calculated densities for solutions, and certain material and water/$NaNO_3$ suspension. The technology showed significant variance between the measured and calculated densities for complex mixtures (multiple solids). This variance was again attributed to the significant attenuation of the acoustic pulse after traversing the suspension. This attenuation caused issues in the detection of the correct return echo from the suspensions. With incorrect detection, the measured density value showed significant errors (> 20%).

Based on the results of the testing at the ITS facilities, it is evident that the technology still requires the following: applied research in the design and selection of the necessary transducers to provide the needed sensitivity; additional engineering analysis to improve signal acquisition and detection at low signal levels; and basic research into the influence of complex mixtures that contain matter that displays an inverse relationship between speed of sound and concentration. With these limitations, the technology is not at the readiness level required for deployment at the

WTP waste feed mixing tank AY-102. The USS has several technical limitations that must be addressed before system would be at a TRL readiness level commensurate with a potential deployment in 2-3 years.

TASK 17(12) SUMMARY - ADVANCED TOPICS FOR MIXING PROCESSES (FIU YEAR 1 TO FIU YEAR 4)

Many engineering processes at various U.S. Department of Energy sites include the fluid flow of more than one phase such as air and water. Slurry mixing methods such as pulsed-air mixers, air sparging, and pulsed-jet mixing (PJM) are a few examples where more than one fluid phase can exist in contact with another phase. The lattice Boltzmann method (LBM) is a computational fluid dynamics (CFD) method that can provide insight into the behavior of multiphase flows by capturing the interface dynamics accurately during the process and the effects of structures on multiple fluid phases. Florida International University (FIU) conducted computational research during FY2009 – FY2014 in order to develop LBM-based computer codes that could be used by the U.S. DOE scientists and engineers as a prediction tool for understanding the physics of fluid flow in nuclear waste tanks during regular operations and retrieval tasks.

In FY2009, a thorough literature review was conducted to identify the most suitable multiphase fluid modeling technique in LBM and a single-phase multi-relaxation-time (MRT) based LBM code was developed. In FY2010, FIU identified and evaluated a multiphase LBM using a single-relaxation-time (SRT) collision operator and updated the collision process in the computer code with an MRT collision model. For static bubbles, it was found that the SRT and MRT multiphase LBM were successful in capturing the surface tension force at the interface while the MRT results showed a slight increase in spurious velocities. In terms of dynamic bubbles, the bubble shapes obtained with the SRT and the MRT LBMs were found to be different, caused by the relaxation parameters used in the MRT method.

In FY2011, the MRT LBM code was extended into three dimensions and the serial computer code was converted into a parallel code. For static bubbles, it was found that MRT multiphase LBM were successful in capturing the surface tension force at the three dimensional bubble interface. In terms of dynamic bubbles, the MRT LBM was found to be capable of simulating various scenarios of bubble rising conditions. LBM requires attention when the fluid interface between multiple phases comes in contact with solid surfaces in order to yield the correct molecular forcing exerted on the fluids by the surface. In FY2012, a contact angle method was implemented and a feature was developed to import complex geometries into LBM. A procedure to incorporate complex geometries into the LBM simulation was also presented.

In the tanks found at the Hanford Site, there is a thick layer of a slurry-like fluid composed of radioactive and chemical products, which are known to generate gases that are flammable. The strength and geometry of these slurries have a direct impact on gas release, which is shown to be characterized by one single physical property, their initial shearing/yielding strength. As such, mixing and storage systems were analyzed during normal operation with waste slurries exhibiting a non-Newtonian rheology to determine their ability to achieve safe and controllable release of flammable gasses. To combat the problem of gas formation with unintended release, a technique of mixing was employed that is able to release these bubbles in a controlled way; this same method is used for processing and transport. One practice used is known as pulsed jet mixing and is characterized by a vacuum extracting the waste and then re-introducing it back into the tank, resulting in mixing. The physical characteristics of the slurry being mixed have a direct impact on the mixing behavior as well as the zone of influence and cavern formation. Bingham fluids in the tank have shear rates and viscosities that vary extensively, from extremely high near the jet pump and nozzle exit to negligibly small in regions away from the influence of the jet itself. Because of this behavior and the large variation in fluid viscosity, there will be a large variation in the mixing behavior. The other technique employed is air sparging and this method is faced with the same issues that are found with pulse jet mixers when dealing with non-Newtonian slurries. In FY2012, a literature review was conducted in order to investigate the applicability of LBM for the simulation of non-Newtonian fluids since this feature should be incorporated in the engineering calculations for accurate estimations of the performance of various waste removal and handling operations. Various turbulence models such as the Large Eddy Simulation model were also investigated for the multiphase LBM code developed at FIU due to the nature of the fluid dynamics of the jet created by the PJMs.

In FY2013, it was shown that the LBM has the ability to model the behavior of multiphase, stress-dependent flow of viscoplastic materials. It was observed that the software package with all of its existing features needed additional development to be ready for deployment at DOE sites, mostly in the simulation of turbulent, high velocity jet penetration flows to replicate the PJM behavior in waste tanks.

In FY2014, an LBM was presented that could model multiphase non-Newtonian flows accurately and efficiently. Special attention was given to flow injection simulations with fluids characterized as Bingham plastics. The nonlinear stress and strain relationship in Bingham plastics has been produced by a certain threshold of stress imposed in the simulations in order for yielding and flow to occur. The LBM presented was able to provide stable and accurate simulations of Bingham plastics and the interactions between the fluid and the gas phases when there is a flow velocity induced in the multiphase system caused by an injection from an open boundary.

In sum, this study at FIU revealed that the extension of the lattice Boltzmann method for the simulation of complex fluid flows including turbulent flows and non-Newtonian fluids is possible via various approaches, although a well-established method has not yet been achieved. FIU’s literature review showed that the incorporation of non-Newtonian fluid properties in the LBM simulations have been presented more consistently in the scientific community in contrast to the turbulence models proposed for LBM. The LES-LBE applications show more promise in terms of turbulence modeling with LBM due to its simpler implementation and higher accuracy over the two-equation models. It should be noted that FIU was not able to find an application of LBM for turbulent flows in a multiphase flow configuration; therefore, the task to simulate turbulent flows in nuclear tanks with multiple phases of fluids using an LBM-based CFD code would be a challenging and scientifically important effort, especially if both of the subgrid models and Bingham plastic effects could be incorporated simultaneously in the viscosity definition of the lattice Boltzmann equation.

TASK 18 SUMMARY - TECHNOLOGY DEVELOPMENT AND INSTRUMENTATION (FIU YEAR 4)

As the Hanford Site prepares for retrieval operations, improved instrumentation will be required to ensure appropriate mixing and delivery of waste to meet the Waste Treatment and Immobilization Plant (WTP) waste acceptance criteria. Until WTP comes online, space in double-shell tanks (DST) is limited. Tank waste is also held in staging tanks prior to being sent for vitrification at WTP and understanding the amount of solids in both the DSTs and staging tanks is of critical importance. FIU has worked with several site engineers to identify the fundamental technology requirements for instrumentation that can be used to identify solid layers in tanks and quantify the amount of residual solid waste in staging tanks.

As part of this task, FIU's solid-liquid interface monitor (SLIM) has been evaluated for its future use in Hanford's HLW mixing tanks. The waste processing operations need to ensure that mixing by pulse-jet mixers (PJMs) is thorough and that solids are completely suspended and removed with each batch. Therefore, a technology that could see through the turbulent liquid and entrained solids during mixing and verify that no solids remained on the floor would allow operators to know that the waste was completely suspended and able to be transferred out of the tank for further processing.

FIU successfully demonstrated the bench-scale testing, proof of concept, for the application of SLIM in mixing tanks for short imaging periods (< 1 minute). With proof of concept testing successful, FIU developed a Phase II Test Plan for the continued evaluation of SLIM. The built-in commercial sonar imaging software does not function with sparse sonar data sets such as those generated in times less than 1 minute. Thus, a 3-D sonar imaging software has been developed for quick scans and has been refined by incorporating new data filters.

The goal of Phase II testing of SLIM is to verify that the technology will meet all functional requirements for a technology deployment into a high-level radioactive waste mixing tank. The functional requirements include data quality objectives for the accuracy, speed and other performance requirements for SLIM components (i.e., mechanical deployment system, sonar and software systems). The functional requirements also include safety analyses, deployment and operating procedures, and other requirements needed for any technology deployed in HLW at Hanford.

As part of Task 18, FIU has also begun developing inspection tools for the evaluation of tank integrity at Hanford. Recently, small amounts of waste have been found in the annulus of AY-102, prompting the need for developing inspection tools that can identify the cause and exact location of the leak. Three separate access paths can be used to obtain information regarding the tank bottom condition. This includes: 1) refractory air slots though the annulus, 2) 4-in. annulus air supply pipe to central air slots, and 3) 6-in. leak detection pit drain from the central sump. FIU has been requested to investigate developing a technology that will utilize the access through the annulus into the refractory air slots and provide visual feedback of the condition within the air slots. The refractory air slots range from 1 inch to 3 inches in width and provide a complex maze to navigate through, including four 90° turns to reach the center of the tank.

Based on design requirements provided by engineers at Hanford, a design was proposed that consists of a small tank type body which can house a camera and the necessary motors that propel the wheels and tank tread. To avoid existing debris in the air slots and potentially damaging the refractory pad, the proposed design has magnets placed at the base of the unit which allows it to move upside-down along the bottom of the carbon steel tank.

To demonstrate the concept, FIU has developed a 2D simulation model in Abaqus that can be used to make design modifications in a virtual environment. In order to develop the design and obtain initial specifications for the 2D simulation model, information on commercially available off-the-shelf components was compiled. The tool was modeled using four rigid bodies: two for the wheels, one for the tool body, and one representing the tank floor. Additionally, a flexible body was used to model the track that fits around the wheels. The inspection tool body encompasses the weight of all of the components except for the tether, wheels and track. To obtain an initial approximation for the weight in the simulation, the weight for two motors, magnets and a camera were used. Other system properties obtained and provided as input to the model included coefficients of friction, magnet strength and hypereleastic constants.

The length that the inspection tool can travel will be limited by the drag force created by the tether (for video feedback and control). Results from the simulation demonstrated that a maximum pulling force of 2.888 lb was achieved when applying a torque of 0.089 in-lb. Torques greater than the maximum value did not provide higher pulling forces due to slippage of the wheel and the track.

TASK 19 SUMMARY – PIPELINE INTEGRITY AND ANALYSIS (FIU YEAR 4)

Washington River Protection Solutions (WRPS) has implemented a fitness-for-service program which will evaluate the degraded condition of the tank farm waste transfer system. The Tank Farms Waste Transfer System Fitness-for-Service Requirements and Recommendations, includes a requirement to inspect primary piping, encasements, and jumpers for corrosion/erosion.

As part of this study, several jumpers from the 242-A Evaporator Pump room and the AW-02E Feed Pit were removed and inspected via ultrasonic thickness measurements. The jumpers in the 242-A Evaporator Pump room included 18-4, C-4&5, J-13A, 13-K, and 19-5. All of these jumpers were removed permanently except for jumper 19-5 which will be reinstalled for further service. The jumpers from the AW-02E Feed Pit included 1-4 and B-2.

This task provides analysis for the aforementioned jumpers as well as the estimated remaining useful life for the components based on the wall thinning measured (ultrasonic thickness). This analysis includes wear trends and correlations with the volume of fluid transferred.

Jumper 18-4 has not transferred any waste and can be used as a baseline for comparing C-4&5 and 19-5 which transferred approximately 11 and 42 Mgal of slurry, respectively. Average thickness measurements for the sections in Jumper 18-4 were slightly above the manufacture's nominal thickness. Average thicknesses for the sections evaluated in Jumper C-4&5 were very similar with only Straight-5 having an average thickness of 0.001 inch below nominal. This suggests that no erosion has occurred in Jumper C-4&5.

Jumpers J-13A and 13-K transferred approximately 29 and 86 Mgal of supernatant, respectively. Average thicknesses for the sections evaluated in Jumper J-13A were slightly different, demonstrating that there was no erosion trend. Average thickness measurements for the sections in Jumper 13-K were all above the manufacture's nominal thickness and in three of the sections, significantly above nominal. Jumper 13-K transferred approximately three times the supernatant that Jumper J-13A transferred, yet did not have any component below the manufacturer's nominal thickness. This suggests that the variations observed are not due to erosion.

Jumper 1-4 transferred at least 17 Mgal of feed waste in addition to an unknown amount of recirculation waste. This uncertainty makes it difficult to assess erosion trends between the two jumpers. Regardless, average thickness measurements for the sections analyzed for both the 1-4 and B-2 jumpers were above the manufacturer's nominal values.

TASK 2.1
DEVELOPMENT OF ALTERNATIVE UNPLUGGING TECHNOLOGIES (FIU YEAR 5)

EXECUTIVE SUMMARY

In previous years, Florida International University (FIU) has tested and evaluated a number of commercially available pipeline unplugging technologies. Based on the lessons learned from the evaluation of the technologies, two alternative approaches have been developed by FIU. These are an asynchronous pulsing system (APS) and a peristaltic crawler. The APS is based on the principle of creating pressure waves in the pipeline filled with water from both ends of the blocked section in order to break the bonds of the blocking material with the pipe wall via forces created by the pressure waves. The waves are created asynchronously in order to shake the blockage as a result of the unsteady forces created by the waves. The peristaltic crawler is a pneumatically operated crawler that propels itself by a sequence of pressurization/depressurization of cavities (inner tubes). The changes in pressure result in the translation of the vessel by peristaltic movements.

For this performance period, additional experiments were conducted to further validate the asynchronous pulsing system's ability to unplug a large-scale pipeline test bed and compare the performance of the APS to the data obtained from the testing conducted on small-scale test beds.

As in the previous year's work, the unplugging experiments consisted of placement of 3-ft kaolin-plaster plugs within a test pipeline loop which consists of two 135-foot runs on either side of a plug and using the system to unplug the pipeline. The pipelines were instrumented with accelerometers and pressure transducers that can capture vibration and pressure data in the pipeline. Various conditions within the pipeline were evaluated including lines with and without entrained air. Initial studies concentrated on determining how air entrainment can be mitigated.

For the engineering scale unplugging testing, parametric trials were conducted using a dummy plug to determine the effects of varying static pressure, amplitude of the pulse pressure and pulse frequency. Research efforts also focused on manufacturing a plug that had the necessary material characteristics and could not be removed by static pressures less than 300 PSI. Unplugging trials were conducted based on the optimal results obtained from the parametric testing. Trials included using sine, triangle and saw tooth wave types as well as pulse frequencies of 1, 2 and 3 Hz under a static pressure of 50 psi. The results obtained during the experimental phase of the project are presented which include pressures and vibration measurements that capture the propagation of the pulses generated by the system.

INTRODUCTION

As Hanford moves into a more aggressive retrieval and disposal program, site engineers will increase waste transfer activities using their cross-site pipelines. This increased activity comes with a corresponding increase in the probability of a pipeline plugging. In the past, some of the pipelines have plugged during waste transfers, resulting in schedule delays and increased costs. Furthermore, pipeline plugging has been cited as one of the major issues that can result in unplanned outages at the Hanford Waste Treatment Plan (WTP), causing inconsistent waste throughput. As such, the availability of a pipeline unplugging tool/technology is crucial to ensure smooth operation of the waste transfers and to ensure Hanford tank farm cleanup milestones are met. Current commercially available pipeline unplugging technologies do not provide a safe, cost-effective and reliable means to address the current problems [1]. The Applied Research Center (ARC) at FIU has evaluated the lessons learned from previous technology testing, and has developed two pipeline unplugging concepts that can be added to the site's "toolbox" [2]. The concepts that FIU has developed will address various plug scenarios with improved deploy-ability and performance. One of the concepts developed is called the asynchronous pulsing system (APS). This document presents a summary of the technology development as well as the results from the experimental testing for APS performed at FIU.

EXPERIMENTAL TESTING OF THE ASYNCHRONOCUS PULSING SYSTEM

Background

In order to clear plugged radioactive waste transfer lines, non-invasive techniques can have significant advantages over invasive devices by avoiding worker exposure to radioactive waste and potential spread of contamination. During previous work, FIU evaluated two technologies that fall into this category: NuVision's wave erosion method and AIMM Technologies' hydrokinetics method. These technologies fill the plugged pipeline with water up to an operating pressure level and induce a pressure variation at the inlet of the pipeline to dislodge the plug. Using the experience obtained during experimental evaluations of both technologies, FIU has developed a non-invasive unplugging technology called the asynchronous pulsing system (APS) that combines the attributes of the previously tested technologies. The APS is based on the idea of creating pressure waves in the pipeline filled with water from both ends of the blocked section in order to dislodge the blocking material via forces created by the pressure waves. The waves are generated asynchronously in order to break the mechanical bonds between the blockage and the pipe walls as a result of the vibration caused by the unsteady forces created by the waves. A pipeline unplugging technology using similar principles for generating pressure pulses in pipelines has previously been tested at the Idaho National Laboratory (INL) by Zollinger and Carney [2]. The most relevant difference of the current technology from the unplugging method developed at INL is that both sides of the pipeline are used to create the asynchronous pulsing in the current technology. Figure 1 shows a sketch of how this technology can be utilized for a typical plugging scenario. This year's work involved conducting a larger engineering scale test matrix. Testing included conducting parametric tests to determine the optimal operating parameters as well as applying these parameters to unplug the pipeline. The experiments consisted of placement of a 3-ft. kaolin-plaster plug in between two 135-foot pipeline sections.

Figure 1. Pipeline unplugging scenario in a horizontal pipe.

General Description

The asynchronous pulsing method is based on the idea of creating asynchronous pressure waves in a blocked section of a pipeline filled with water in order to dislodge the blockage by the forces created by the pressure waves. The waves break the mechanical bonds between the blockage and the pipe walls as a result of the vibration caused by the unsteady forces that are created by the waves. Figure 2 illustrates the basic principle and components of the technology.

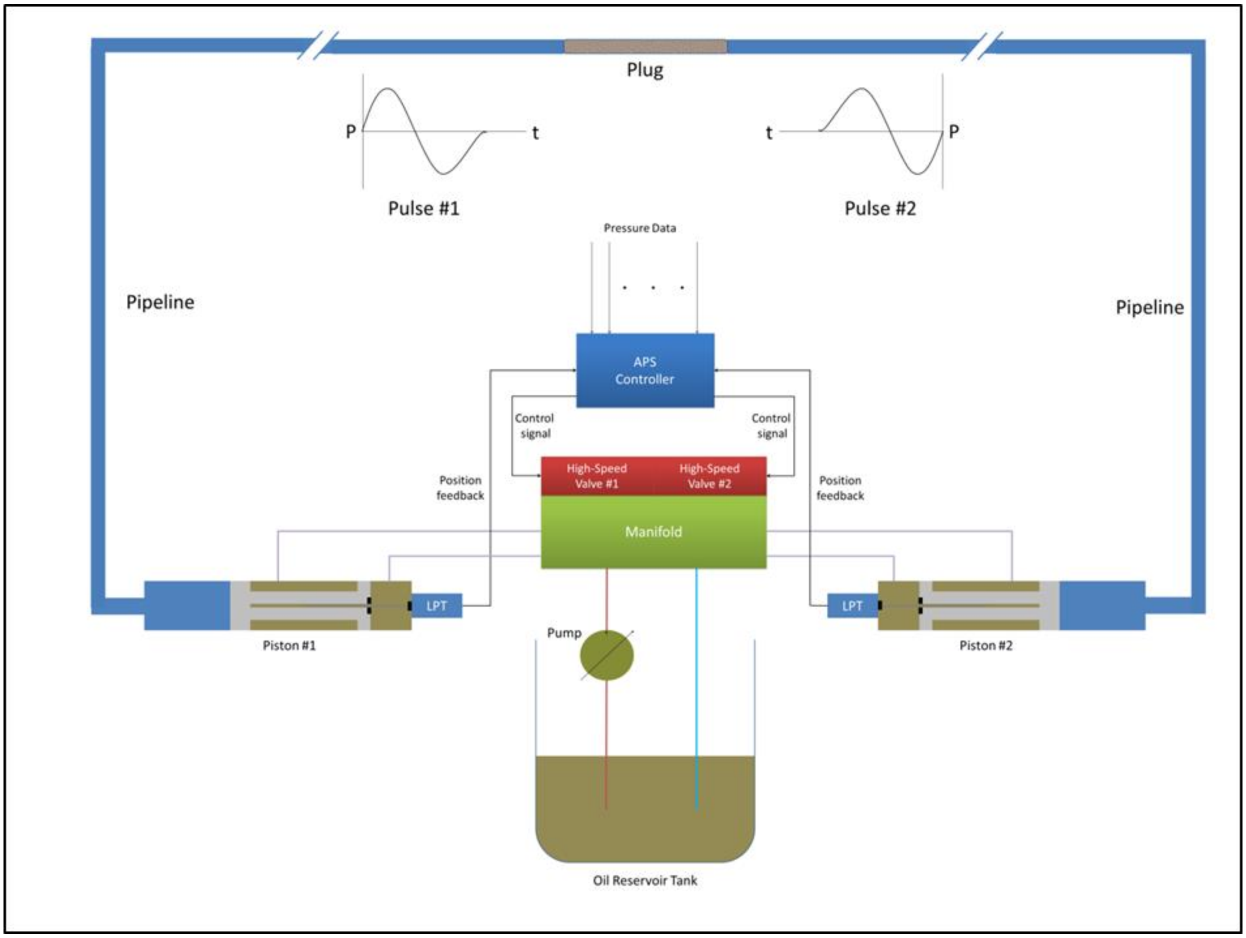

Figure 2. Principles of asynchronous pulsing method with major components labeled.

The pressure waves are created by a pair of hydraulically operated piston water pumps that are attached to both ends of the pipeline. The hydraulic oil that drives the pumps is provided by a hydraulic unit that is powered by a 10 HP 240-volt 3-phase electric motor which drives a hydraulic oil pump to generate oil pressure. The hydraulic unit is equipped with an oil pressure regulator to control the pressure of the oil leaving the unit to between 100 and 2000 PSI. A pair of rapid-acting proportional valves control the direction and quantity of oil entering each of the water pumps. This controls the position, direction of movement and speed of each water pump's piston. By varying the hydraulic oil pressure along with the opening speed of the proportioning valves, each water pump is used to create a pressure pulse into the pipeline.

TESTING AND RESULTS - ASYNCHRONOCUS PULSING SYSTEM

Engineering Scale Testbed

Figure 3 shows the piping and instrumentation diagram of the engineering scale loop which consists of two 135-foot runs on either side of a plug. The elevations of the pipeline supports were surveyed and adjusted to provide a pipeline slope of 0.14 degrees. As can be seen in Figure 4, the hydraulic power unit was placed inside a shed to protect it from the rain.

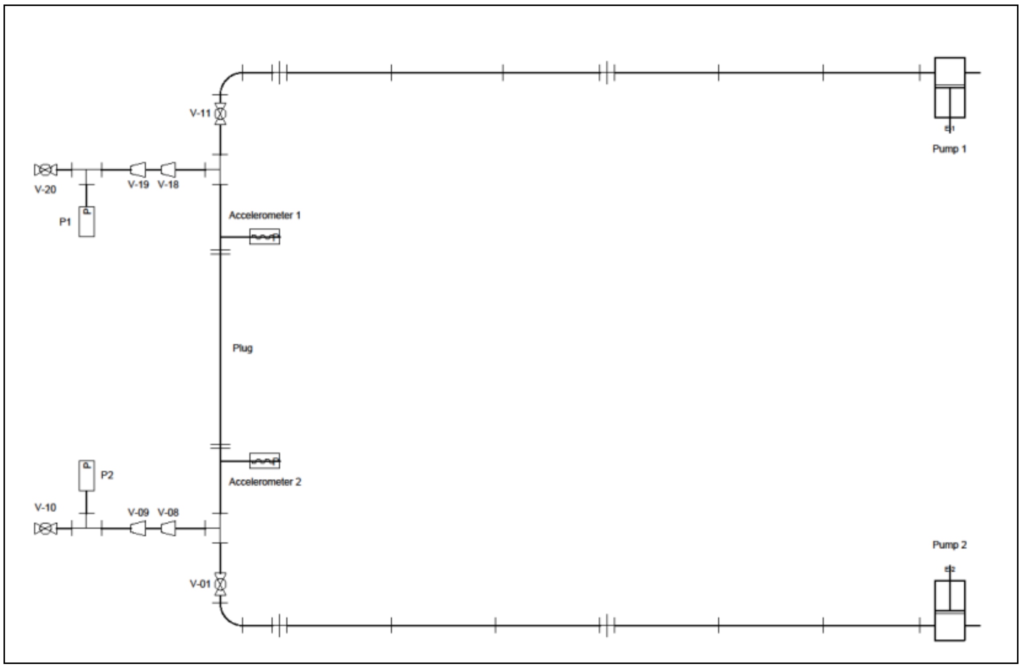

Figure 3. Engineering scale asynchronous pulsing test loop piping and instrumentation diagram.

Figure 4. Engineering scale testbed images for asynchronous pulsing system.

Unplugging Tests

Unplugging experiments were conducted using triangle, square, and sine waves at frequencies of 1, 2 and 3 Hz. A total of nine experiments were conducted and unplugging was achieved during each experiment. Table 1 shows the results of each test, including the signal type, frequency, the average peak, trough and amplitude of both static and dynamic pressures, as well as the number of cycles and cycle time needed to unplug the pipeline.

Table 1. Unplugging Test Results

Signal Type	Frequency (Hz)	Static Pressure Transducer			Dynamic Pressure Transducers			Cycle Count	Cycling Time (sec)
		Average Peak (psi)	Average Trough	Average Amplitud	Average Peak (psi)	Average Trough	Average Amplitud		
Triangle	1	192.5	0	192.5	60.5	-6.75	67.25	1973	1973
Triangle	2	141.5	45	96.5	31.5	-3.4	34.9	2805	1403
Triangle	3	142.5	50	92.5	30	-6.5	36.5	15818	5273
Square	1	192.5	30	162.5	34	-31.5	65.5	2708	2708
Square	2	156	32.5	123.5	17	-35	52	4344	2172
Square	3	142	45	97	31.5	-15	46.5	9892	3297
Sine	1	197.5	17	180.5	58	-6	64	1816	1816
Sine	2	148	42	106	33	-5	38	5113	2557
Sine	3	137.5	55	82.5	9	-29	38	8162	2721

An example of the pressure data obtained during the unplugging trials is provided in Figure 5. Prior to the unplugging occurring, the pressure profile on each side of the plug face has a sharp peak, while after unplugging, the profile amplitude is reduced and develops a flat peak. This change in the profile is due to water leaking past the blockage.

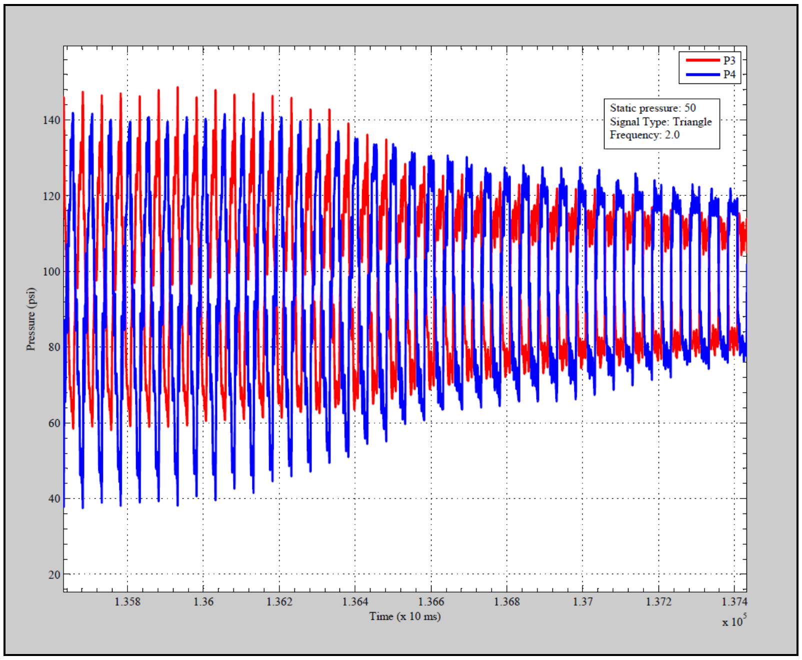

Figure 5. Unplugging pressure profile for a triangle wave at 2 Hz.

While analyzing the data, it was discovered that two unplugging trials had significantly shorter unplugging times than a majority of the trials. Figure 6 shows pressure responses at each face of the plug for one of these trials. Since all plugs were manufactured using the same batch of kaolin and plaster of Paris, it was concluded that the deviation was due to manufacturing variances, which has been well documented in simulants made with kaolin clay. A second set of trials were performed using plugs manufactured with the same material and procedure. Operational parameters for the trials were repeated and the results were similar (in terms of unplugging times) with the general trends. Figure 7 shows the results from a repeated trial.

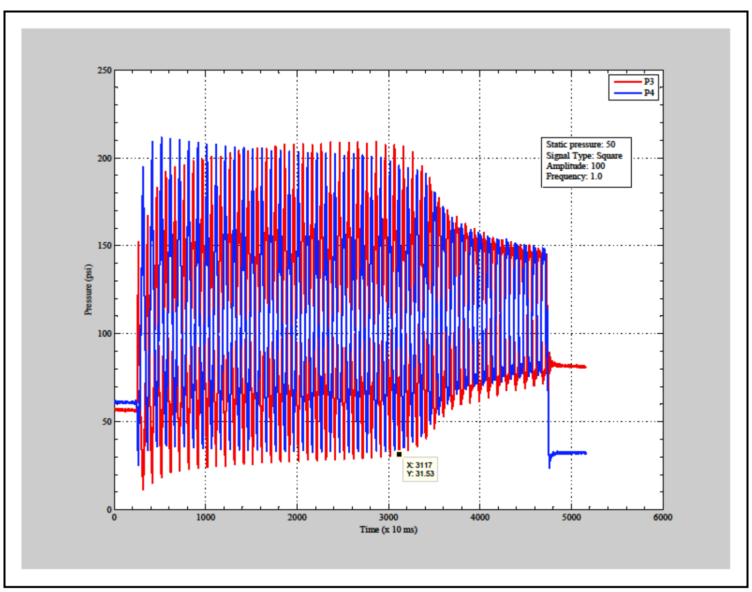

Figure 6. Pressure responses of an unplugging trial with significantly shorter unplugging time.

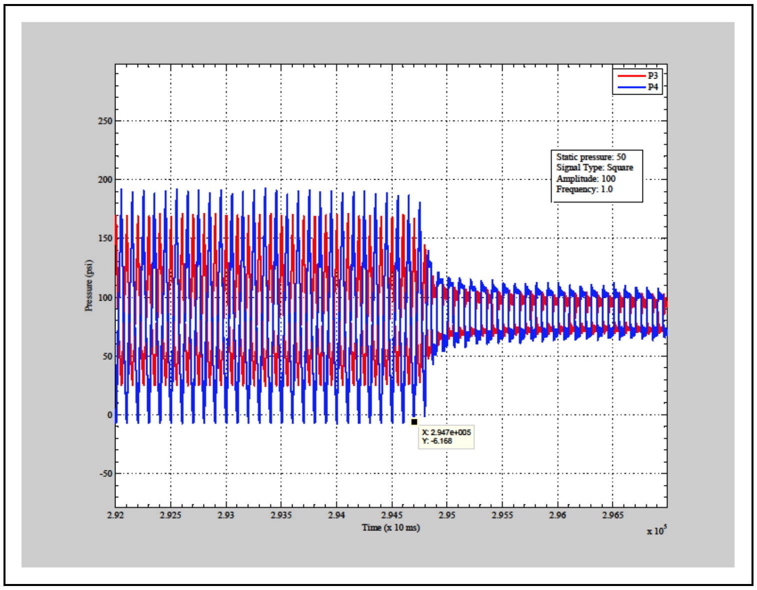

Figure 7. Pressure results from a repeated unplugging trial.

Following the repeating of the unplugging trials for the asynchronous pulsing system, data analysis resumed, comparing pressure differentials, dynamic responses and cycle counts. During the analysis, it was observed that even though the plugs were unplugging, the system was not delivering the optimal pressure pulses to the plug. As can be seen in Figure 8 and Figure 9, pressure transducer 4 recorded a higher reading than transducer 3. Since both transducers were calibrated before installation, the difference in pressure is likely explained by small amounts of residual air trapped within the pipeline on the transducer 3 side.

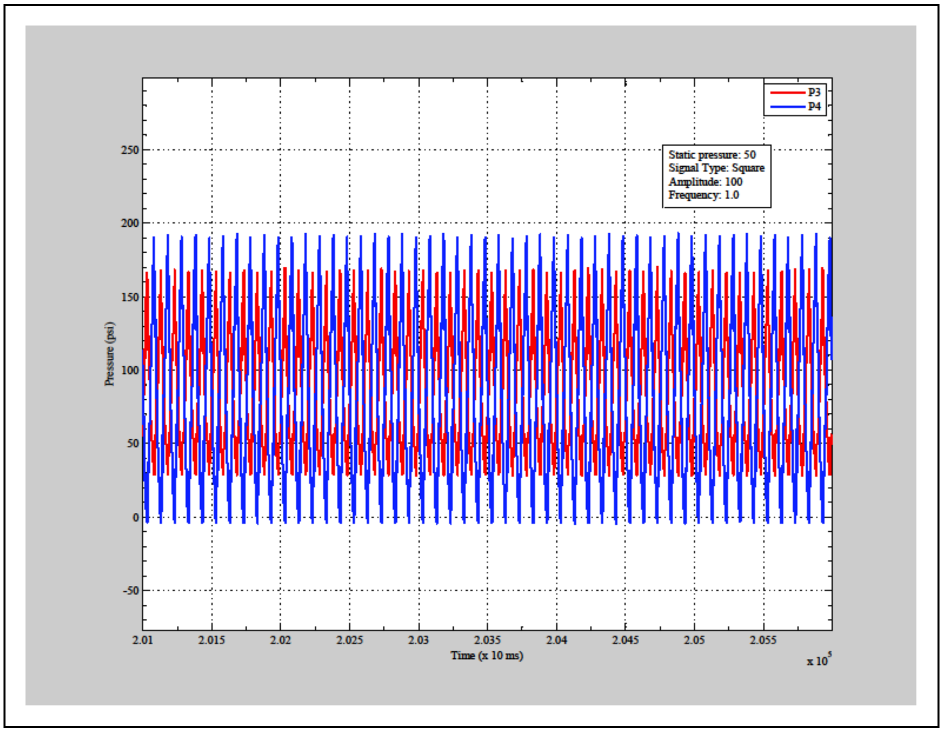

Figure 8. Square wave pulse at 1 Hz.

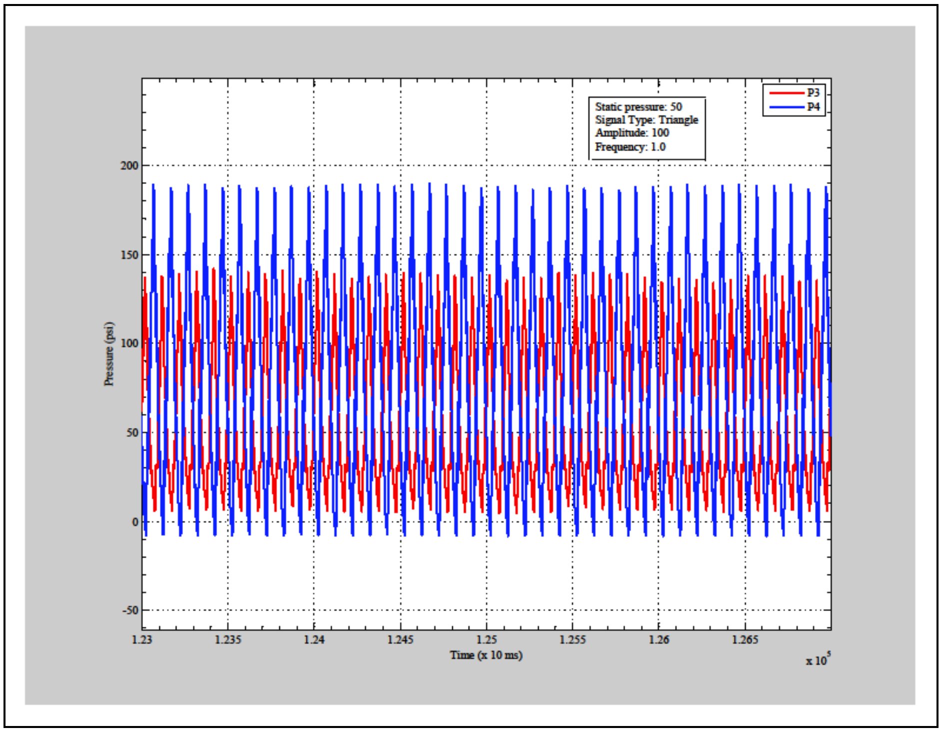

Figure 9. Triangle wave pulse at 1 Hz.

Efforts next concentrated on developing several test strategies to systematically determine the system's limitations when air is entrapped in the engineering scale pipeline system. Since similar trials had been performed in the past with smaller pipe loops, we used this data to estimate the effects and mitigation techniques for the larger pipeline. The tests served as a validation and included a variable that wasn't present previously: the inclusion of a sample test plug during the air mitigation process. The main concern is that applying the mitigation techniques would pre-fatigue the test plug before being able to accurately perform the unplugging testing. The previous test process included a resting time to allow the air to agglomerate and travel, followed by applying a minor vacuum combined with several pulses to vibrate the water column. The vacuum serves to expand air pockets that may be trapped in crevices while the column vibration aids the air in traveling towards the venting points. This mitigation process was performed in the past without a sample plug since this was conducted as part of performing parametric and baseline testing. The air mitigation process was performed with real plugs installed in the test loop without any effects on the plugs.

Once it was determined that the plugs were not affected by the air mitigation process, work began to determine the effect of air on the system's performance. Tests were run without air as well as with a half a piston stroke volume of air. Each experiment was run twice for each test scenario. For the unplugging tests without air, the average unplugging duration was 4.3 hours while the average duration for the half stroke and full stroke volume was 6.0 and 9.75 hours, respectively. These verification tests demonstrated that the system was capable of unplugging the pipeline with and without air entrained. After all the tests were completed, data from the tests were analyzed. Table 2 shows the results from unplugging trials.

Table 2. APS Unplugging Trials

Air Quantity	Trail	Unplugged (Y/N)	Time Elapsed (Hrs)	Amplitude (A)	Frequency (Hz)	Wave Type
No Air	1	Y	4	100/150	1,2,3	Square
	2	Y	3	150	1	Square
	3	Y	6	150	1	Square
Half-Stroke	1	Y	4.5	150	1	Sine
	2	Y	8	150	1	Square
	3	Y	5.5	150	1	Square
Full-Stroke	1	Y	9.5	150	1	Square
	2	Y	10	150	1	Square

After analyzing the data, the following observations were made:

- With no air in the system, the plug was unplugged at an average of 4 hours and 20 minutes.
- With a half stroke of air in the system, the plug was unplugged at an average of 6 hours.
- With a full stroke of air in the system, the plug was unplugged at an average of 9 hours and 45 minutes.

Below are two samples of unplugging data: one includes results from baseline tests with no air and another with a half of stroke of air. Shown in the graphs are pressures from each side of the plug face. The pressures clearly act in an asynchronous and oscillatory manner, maximizing the forces which cause the plug to dislodge. The change in amplitude corresponds to either a breach in the plug or movement of the plug.

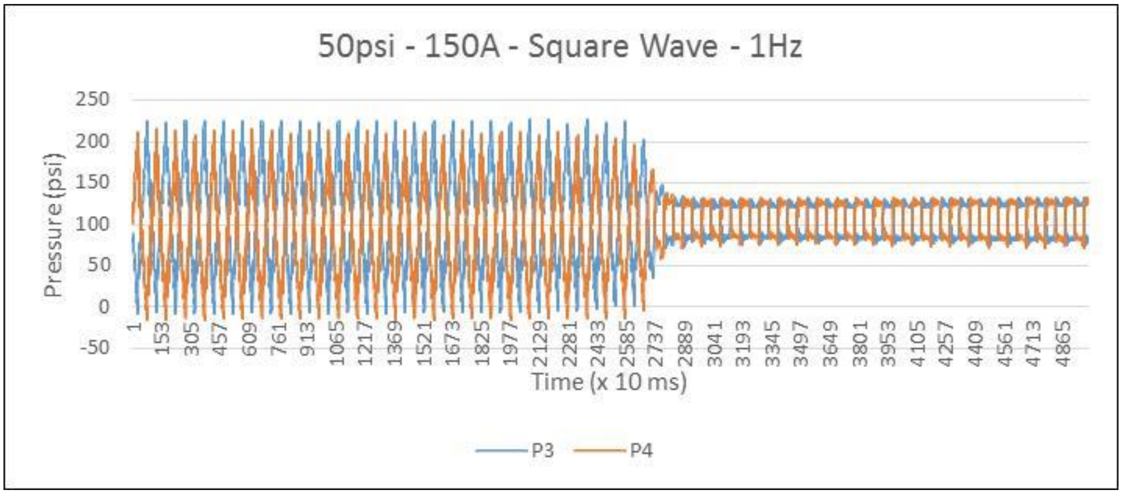

Figure 10. No air in system – unplugging results.

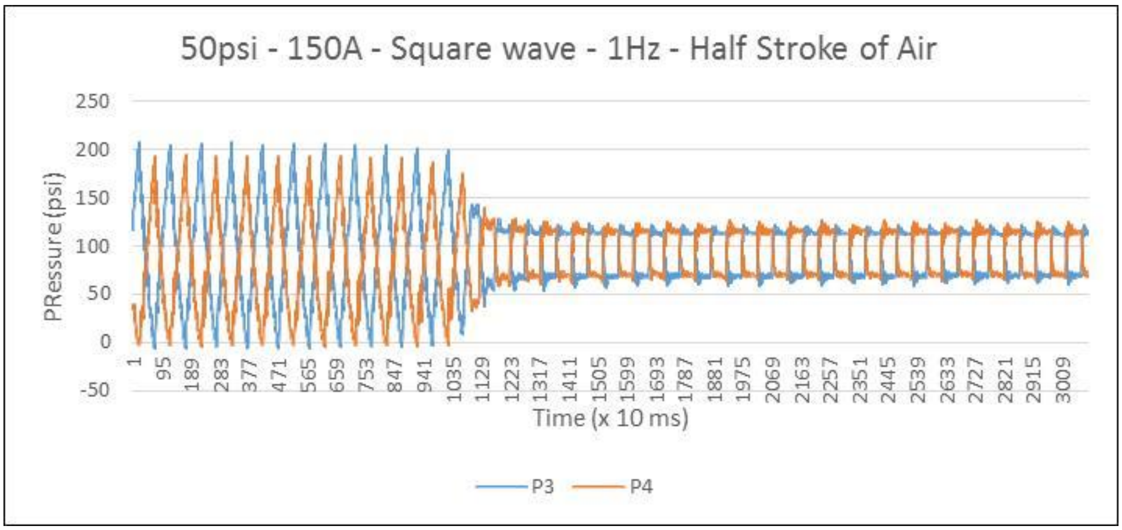

Figure 11. Half-stroke of air in system – unplugging results.

Evaluation of the experimental data initially focused on the testing that was conducted at 1 Hz. This analysis is intended to assist in the explanation of unplugging times for the trials conducted with various amount of air entrained in the system. Pressures at the pistons were compared to the pressures at the plug faces to understand the overall change in pressure along the pipeline. In most cases, some amount of amplification was observed between the inlet and plug face, even with the air entrained. It should be noted that our test system has an inclination similar to the cross-site lines. This means that air on the P4-P6 side resides next to the piston face and air on the P1-P3 side resides on the plug face. The variability of the location of the air entrained could explain some of the variability seen in the data. Additionally, the APS control system is designed to compensate for air by increasing the static pressure, further complicating the evaluation of the data. Lastly, variation in temperature throughout the course of testing also changes the pressure in the line dramatically.

Figure 12 shows an example of one trial data set and how it was analyzed. Pressure peaks for representative sections of the testing show how the pressure at the inlet (1, 4) compared to those at the plug face (3, 6). The average of the peak difference was determined, indicating the level of amplification for each test trial.

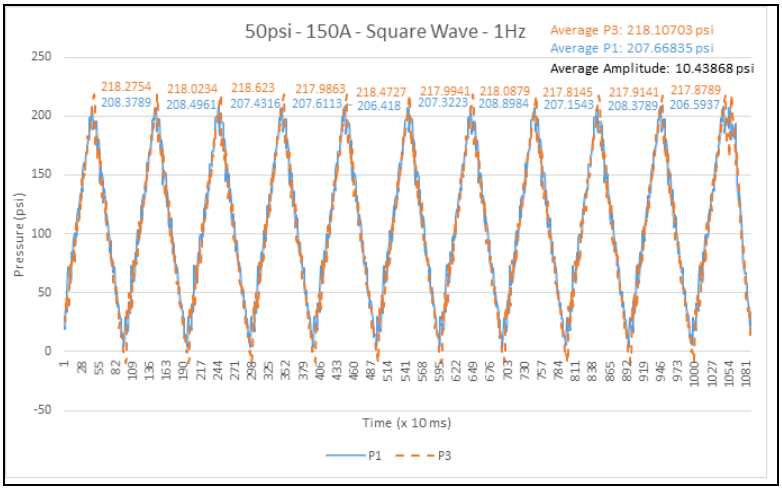

Figure 12. Example data sample to evaluate line pressure.

Table 3 shows the representative pressure differences from each of the trials at 1 Hz. All pressures are in psi. In general, as air increased, the time to unplug also increased. FIU would expect that the pressure amplification would decrease with increasing amounts of air. However, due to the aforementioned reasons, some variability was observed. The pressure peak differences appear similar in magnitude with the exception of the half-stroke case on the P4-P6 side. In this trial, virtually no amplification was observed.

Table 3. APS Unplugging Trials for 1 Hz

Amount Air	Unplugging Time	Ave P1 Peak	Ave P3 Peak	Ave P1-P3 Amplitude	Ave P4 Peak	Ave P6 Peak	Average P4-P6 Amplitude
No Air	6 hours	207.7	218.1	10.4	211	203.8	7.2
Half Stroke Air	5.5 hours	189.5	205.8	16.4	189.2	179.6	9.6
	8 hours	216.9	225.9	9	184.9	184.9	0.1
Full Stroke Air	9.5 hours	231.9	241.4	9.6	144.6	133.1	11.4

DISCUSSIONS AND CONCLUSIONS

During the data analysis of the experimental data obtained from this year's testing, it was observed that various factors affected the results of the testing, including piston drift, the temperature of the pipeline, and amount of air within the pipeline as well as variability in the strength of the plug.

Each pump's piston position is controlled by the computer via LabView. By obtaining feedback readings from the pressure transducers, the piston position transducers, and the desired pressure pulse profile, the control software determines the starting position and how far and how fast to drive each piston forward. The controls try to maintain a desired static pressure within the pipeline by moving the piston forward to compensate for drops in pressure. The piston can drift from its nominal state due to this compensation as well as high frequency pulsing that does not allow the piston enough time to return to its original starting position.

As mentioned previously, the temperature of the pipeline can also significantly affect the unplugging results. As the temperature increases, the water itself tries to expand but is restrained because of the small (or no) amount of air in the system; therefore, when the temperature in the pipeline is increased slightly, the pressure in the system will increase greatly. Temperature in the system varies with ambient temperature, weather conditions, etc. and is amplified by the black iron pipes that compose the system. The results of the temperature variation cause large variability in the pressure waves that are sent through the system, changing the amplification of the waves as well as the amplitude. Temperature also has a significant effect on the variability of the starting pressure in the system along with the amount of air entrained.

The volume of air within the pipeline can adversely affect the efficiency of the system. When the pipeline temperature is increased (due to environmental conditions), existing air pockets within the system are more easily removed. This is due to the expansion of the air pockets, which allows them to travel to the highest points in the pipeline section where purge valves are located to expel the air. However, variability in ambient temperature proves to be an obstacle when performing air mitigation techniques. It is important to note that the complete removal of air from the pipeline is very difficult in terms of our air mitigation practices; therefore, variability will exist between unplugging tests conducted with different amounts of entrained air.

Another parameter that can affect unplugging results is the variability of the plug. Initial blow out tests ranged from 400 to 600 psi. Upon testing, it was observed that the success of making this plug was significantly impacted by the plug material, development procedure and conditions. For instance, mixing for a prolonged or shortened time would yield different shear strengths for the same composition. Pressure blowout tests were conducted on a variety of 3-ft kaolin-plaster plugs in order to verify that the plugs could withstand a maximum static pressure of 400 psi. Results showed that the optimal plug had a composition of 30% kaolin, 35% plaster and 35% water (by weight) with a 24 hour "wet cure" time (wet curing involves keeping the plug in a moist environment). Results from initial blow out tests showed that the plugs could withstand pressures from 400-600 psi, where any pressure exceeding 400 psi was optimal for testing.

REFERENCES

1. Roelant, D., (2012). FY2012 Year End Technical Report. Chemical Process Alternatives for Radioactive Waste. U.S. Department of Energy, Office of Environmental Management.

2. Zollinger, W., & Carney, F. (2004). Pipeline blockage unplugging and locating equipment. Conference on Robotics and Remote Systems- Proceedings, (pp. 80 - 85). Gainesville.

TASK 2.2
COMPUTATIONAL SIMULATION AND EVOLUTION OF HLW PIPELINE PLUGS (FIU YEAR 5)

EXECUTIVE SUMMARY

At Hanford, an extensive network of pipelines traversing several miles is used to transfer the high level radioactive nuclear waste from tanks to the treatment facilities. During transfer operations, however, there is a potential risk for the transport lines to plug, causing significant delays, increasing operation costs and creating hazardous conditions for personnel and the environment. Pipeline plug formation has been primarily attributed to changes in the chemistry and flow patterns within the pipe transfer system at Hanford [1]. The use of CFD software has been explored in the past to predict plug formation [2, 3]. The plugging mechanism simulated was settling of solids. Even though the efforts were promising, the models lacked incorporation of chemical reaction kinetics. Hence, a new task was initiated as part of Florida International University's (FIU's) research efforts to develop a multi-physics model using computational fluid dynamics (CFD) software that could simulate the coupled flow and chemistry kinetics and aid in understanding the plug formation process.

During this reporting period, several three dimensional (3D) virtual scenarios representing multi-phase flow conditions in a pipe were simulated to study the settling dynamics in a pipeline. The CFD software used to facilitate the model development and analysis was Comsol Multiphysics 4.3b. The mixture interface was used to investigate the multiphase interactions and solids growth in a pipeline was modeled. A parametric analysis was carried out, simulating settling of solids as a function of flow velocity, particle size, solids density and volume fraction of solids. The numerical results were validated by experimental results and critical velocity correlations. The 3D numerical results were also compared with prior 2-D studies to evaluate the trade-off between the obtained numerical accuracy and the computing time. Modeling of the multi-phase precipitation kinetics could not be completed due to the inability of the software to model the coupled phenomena.

In addition, the 2D and 3D flow models were developed to analyze the settling characteristics of solids based on complex geometries of pipelines. This included a realistic case of potential plug formation in the test loop developed by PNNL.

INTRODUCTION

A vast amount of radioactive waste has been stored at Hanford spanning several decades. A majority of this waste is stored in tanks and is transferred in the slurry form between tanks and from tanks to processing facilities. A waste transfer system consisting of an extensive network of pipelines is used to facilitate the transfer operations. The main goal of the waste transfer system is to transfer the nuclear waste without plugging the transfer pipelines. Currently, two tools have been used to support this objective: the Environmental Simulation Program (ESP) and empirical based critical velocity correlations. ESP is used to estimate the initial waste compositions and solids volume fraction and critical velocity correlations are used to estimate the minimum velocity to prevent settling of solids during waste transfers. Despite such efforts, several lines have plugged during the waste transfer process at Hanford. The plugging has been attributed to two main factors: chemical instability and settling of solids. Chemical instability during waste transfers results in a phase change (from liquid to solid) initiated due to drops in temperature, changes in local concentration or mixing and pumping of wastes that are not in equilibrium. The solids precipitate or crystallize out of the solution and accumulate along the pipe walls. These serve as a nucleation site where the solids nucleate and grow rapidly and eventually form an interlocking needle-like crystal network. The needle-like crystal network impedes the flow within the pipe and commences the formation of the plug [4]. The presence of precipitates and/or agglomerates increases the solids concentration and increases the viscosity of the slurry. The flow transitions from turbulent to laminar as a result of such changes during transit and the undissolved solids may settle when the flow velocity is not sufficient to keep them suspended. A moving bed of particles then begins to accumulate during slurry transport operation. Settling of solids in a moving bed of particles forms a stationary bed that eventually fills the pipe and blocks the flow. Blocked pipelines pose several problems at Hanford. The plugged pipelines are considered hazardous, hard and expensive to repair and cause significant time delays in the clean-up process. Consequently, most plugged transfer pipelines are abandoned. The phenomenon of settling of solids has been the subject of numerous theoretical and experimental studies [3, 4 and 5]; however, these require extensive experimental set-ups, procuring varied slurries, and carrying out lengthy experimental trials. The theoretical studies rely heavily on empirical formulae which do not take full account of the settling physics. Hence, a need exists for a computational tool that can investigate the influence of various parameters that affect the settling of solids and better aid in understanding the settling dynamics at a click of a button.

A three dimensional (3D) computational analysis has been carried out at FIU, simulating settling of solids in a horizontal pipeline as a function of flow velocity, particle size and volume percent solids using the CFD software Comsol Multiphysics 4.3b. The numerical results are validated with empirical correlations and experimental results as well as with prior 2D numerical studies. The 2D and 3D modeling is further extended to include the effect of complex geometry of the pipeline. The following information is provided in this report: First, the governing equations for the mixture model simulations are introduced. Secondly, simulations modeling and settling of solids are presented in a horizontal pipe. The influence of pipe geometry is presented next followed by the application of the developed CFD model to analyze the settling of solids in a complex pipeline (PNNL test loop). Lastly, conclusions are drawn and discussions are presented.

NUMERICAL APPROACH

The slurry flow in a horizontal pipeline was computed using the mixture model that is part of the Chemical Engineering module of COMSOL Multiphysics 4.3b. The mixture model is a macroscopic two phase model that is able to compute the flow for a mixture of a solid and liquid. It tracks the average phase concentration, or volume fraction, and solves for one velocity field for each phase. The two phases consisted of one dispersed phase (solid particles) and one continuous phase (liquid). The model combined the k-epsilon turbulence model for the main flow with equations for the transport of the dispersed phase and the relative velocity of both phases. Some of the assumptions made while using the mixture model are that the density of each phase was constant; that the pressure field was same and the velocity between the two phases could be ascertained from a balance of pressure, gravity, and viscous drag [6].

Governing Equations

The mixture model treats both the continuous as well as the dispersed phase as a single mixture with a slip velocity between them. The momentum equation for the mixture is given by

$$\rho u_t + \rho(u \cdot \nabla)u = -\nabla p - \nabla \cdot \tau_{Gm} + \rho g + F$$

$$-\nabla \cdot \left[\rho c_d(1 - c_d)\left(u_{slip} - \frac{D_{md}}{(1-c_d)\Phi_d}\nabla\Phi_d\right)\left(u_{slip} - \frac{D_{md}}{(1-c_d)\Phi_d}\nabla\Phi_d\right)\right] \quad (1)$$

where, u denotes mixture velocity (m/s), ρ is the mixture density (kg/m^3), p is the pressure (Pa), c_d is the mass fraction of the dispersed phase (kg/kg), u_{slip} is the relative velocity between the two phases (m/s), τ_{Gm} is the sum of viscous and turbulent stress (kg/(m·s^2)), g is the gravity vector (m/s^2), and F is the additional volume forces (N/m^3).

The velocity u used here is the mixture velocity which is defined as

$$u = \frac{\emptyset_c \rho_c \mu_c + \emptyset_d \rho_d \mu_d}{\rho} \quad (2)$$

Here, c and d denote the volume fractions of the continuous phase and the dispersed phase (m^3/m^3), respectively, u_c is the continuous phase velocity (m/s), u_d is the dispersed phase velocity (m/s), ρ_c is the continuous phase density (kg/m^3), ρ_d is the dispersed phase density (kg/m^3), and ρ is the mixture density (kg/m^3).

The relationship between the velocities of the two phases is defined by

$$u_d - u_c = u_{cd} = u_{slip} - \frac{D_{md}}{(1-c_d)\emptyset_d}\nabla\emptyset_d \quad (3)$$

Here, u_{slip} (m/s) denotes the slip velocity between the two phases, and D_{md} is a turbulent dispersion coefficient (m^2/s) accounting for extra diffusion due to turbulent eddies.

The Schiller-Neumann model was used to compute the slip velocity which uses the following relation,

$$\frac{3}{4}\frac{C_d}{d_d}\rho_c\left|\mu_{slip}\right|\mu_{slip} = \frac{(\rho-\rho_d)}{\rho}\nabla p \tag{4}$$

where C_d is the dimensionless particle drag coefficient and is defined as

$$C_d = \frac{24}{Re}(1+0.15Re^{0.687}), Re \leq 1000 \tag{5}$$

and

$$C_d = 0.44, Re \geq 1000 \tag{6}$$

The mixture density ρ is given by

$$\rho = \Phi_c\rho_c + \Phi_d d \tag{7}$$

where ρ_c and ρ_d (kg/m^3) are the densities of each of the two phases.

The mass fraction of the dispersed phase c_d is given by

$$c_d = \frac{\Phi_d\rho_d}{\rho} \tag{8}$$

The sum of viscous and turbulent stress is

$$\tau_{Gm} = (\mu + \mu_T)[\nabla u + \nabla u^T] \tag{9}$$

where μ (Pa·s) is the mixture viscosity and μ_T (Pa·s) the turbulent viscosity.

The transport equation for Φ_d, the dispersed phase volume fraction, is

$$\frac{\partial}{\partial t}(\Phi_d\rho_d) + \nabla\cdot(\Phi_d\rho_d u_d) = -m_{dc} \tag{10}$$

where m_{dc} (kg/(m^3·s)) is the mass transfer rate from dispersed to continuous phase and u_d (m/s) is the dispersed phase velocity according to Eq. (3).

Assuming constant density for the dispersed phase Eq. (7) is rewritten as,

$$\frac{\partial}{\partial t}(\Phi_d) + \nabla\cdot(\Phi_d u_d) = -\frac{m_{dc}}{\rho_d} \tag{11}$$

The continuous phase volume fraction, $\emptyset_c$, is

$$\Phi_c = 1 - \Phi_d \tag{12}$$

and the continuity equation for the mixture is given as

$$\rho_t + \nabla\cdot(\rho u) = 0 \tag{13}$$

The Mixture Model interfaces assumes that the densities of each phase, ρ_c and ρ_d are constant, and therefore uses the following alternative form of the continuity equation of the mixture,

$$(\rho_c - \rho_d)\left[\nabla \cdot (1 - c_d)\boldsymbol{u}_{slip} - D_{md}\nabla\Phi_d) + \frac{m_{dc}}{\rho_d}\right] + \rho_c(\nabla \cdot \boldsymbol{u}) = 0 \tag{14}$$

The flow turbulence is modeled using the k-ε turbulence model which solves two extra transport equations for the turbulent kinetic energy, k and the dissipation rate of turbulent kinetic energy, ε as described below. The turbulent viscosity is given by

$$\eta_T = \rho C_\mu \frac{k^2}{\varepsilon} \tag{15}$$

where C_μ is a model constant and is equal to 0.09.

The transport equation for the turbulent kinetic energy *k* is

$$\rho\frac{\partial k}{\partial t} + \rho\mu \cdot \nabla k = \nabla \cdot \left(\left(\mu + \frac{\mu_T}{\sigma_k}\right) \cdot \nabla k\right) + P_k - \rho\varepsilon) \tag{16}$$

where the production term is

$$P_k = \mu_T(\nabla\mu : (\nabla\mu + (\nabla\mu)^T) - \frac{2}{3}(\nabla \cdot \mu)^2) - \frac{2}{3}\rho k \nabla \cdot \mu \tag{17}$$

The turbulent kinetic energy, ε, is determined by

$$\rho\frac{\partial \varepsilon}{\partial t} + \rho\mu \cdot \nabla\varepsilon = \nabla \cdot \left(\left(\mu + \frac{\mu_T}{\sigma_\varepsilon}\right) \cdot \nabla\varepsilon\right) + C_{\varepsilon 1}\frac{\varepsilon}{k}P_k - C_{\varepsilon 2}\rho\frac{\varepsilon^2}{k} \tag{18}$$

where $C_{\varepsilon 1}$, $C_{\varepsilon 2}$, σ_k, and σ_ε, are model constant and the values used were 1.44, 1.92, 1 and 1.3, respectively.

Model Geometry and Boundary Conditions

The model geometry for the simulations consisted of a three dimensional (3D) horizontal pipe with a diameter of 0.078 m and a length of 5.2 m. The slurry was modeled as a Newtonian suspension consisting of solids particles dispersed in liquid. The mixture entered through the inlet at velocities characterizing fully developed turbulent flow regimes. The turbulence intensity and length scale were set to 5% and 0.07*r_{in} where r_{in} = 0.039 is the radius of the inlet. The solids were modeled as spherical solid particles of equal size with the particle size ranging from 14.4-220 μm. The solid volume fraction ranged from 2.9-9.8%. The solid densities ranged from 1000-8000 kg/m^3 and the liquid densities ranged from 999-1647 kg/m^3. The outlet was set to zero pressure, no viscous stress and the dispersed phase flow exited the pipe at mixture velocity. A gravity node was added to account for the gravity force in the negative y-direction over the entire domain. Initially, the velocity as well as the solids phase volume fraction was zero in the entire model domain. The mesh used to partition the model domain into sub-domains consisted of triangular elements as shown in Figure 13.

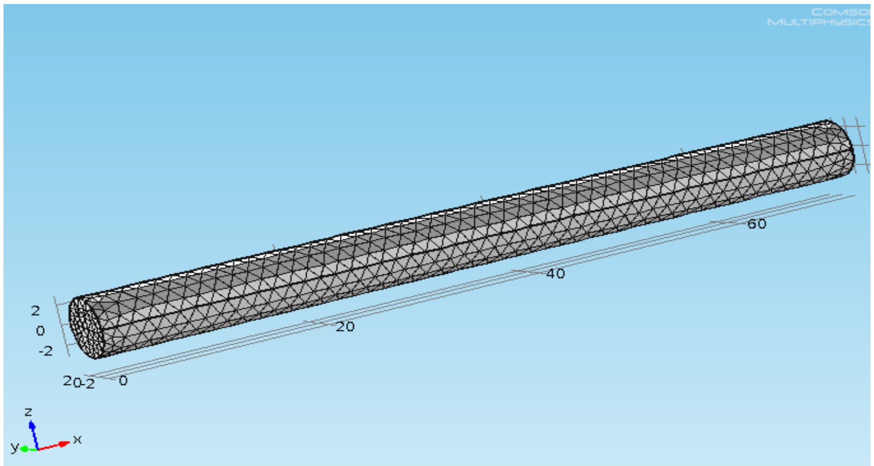

Figure 13. Model geometry and boundary conditions for the mixture model simulations.

RESULTS & DISCUSSION

A. Mesh Optimization Analysis

For the mesh analysis, two types of mesh were evaluated: (a) tetrahedral mesh and (b) swept mesh as shown in Figure 14. The mesh size of the elements was evaluated for three sizes: extremely coarse, coarse and normal.

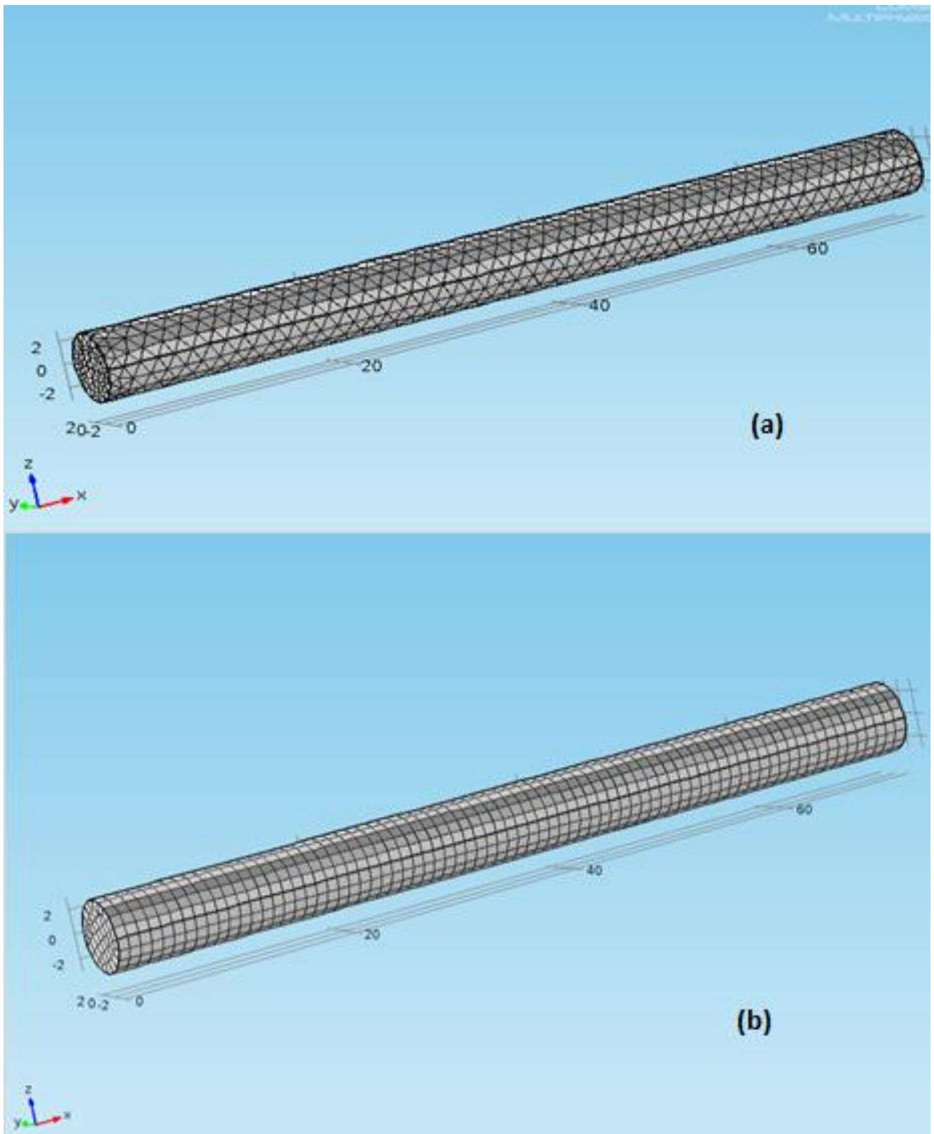

Figure 14. Meshed geometry-3D numerical model: (a) tetrahedral mesh and (b) swept mesh.

The dispersed phase volume fractions for each of the mesh type and mesh size were computed as shown in Table 4. Both the mesh types produced comparable results; however, there was a high variance in the computational time that each of the mesh types took to converge. For instance, for the coarse mesh size, the tetrahedral mesh model took 66 minutes as compared to the 206 minutes it took for the swept mesh model to complete for comparable dispersed volume fraction computations. Hence, it was concluded that for future virtual models, mesh elements of coarse size and tetrahedral mesh type will be the optimal solution for simulations.

Table 4. Mesh Analysis

Mesh Size	Tetrahedral Mesh (dispersed volume fraction)	Swept Mesh (dispersed volume fraction)
Extremely Coarse	0.034	0.0353
Coarse	0.038	0.039
Normal	0.041	0.042

B. PNNL Comparison

The mixture model to simulate settling of solids is solved via a transient simulation. Table 5 below lists the material properties used for the numerical simulations.

Table 5. Numerical Simulations Matrix-PNNL Comparison

	Model Verification Study				
Test Configuration	**1**	**2**	**3**	**4**	**5**
Particle diameter (μm)	14.4	37.7	129.5	182.3	203.9
Solids Density (kg/m^3)	2500	7950	3770	2500	7950
Solids volume fraction (%)	9.8	9.3	8.7	7.4	3.0
Liquid density (kg/m^3)	1146	1647	1151	999	1026
Liquid viscosity (cP)	10.2	9.3	4.5	1.5	1.6

The material properties were obtained from the experimental tests done by PNNL to determine the critical velocity for Newtonian slurries. The critical velocity obtained by the numerical simulations was compared with the experimental results of PNNL and with the empirical based critical velocity correlations. The 3-D numerical results were also compared with the previous 2-D numerical studies to understand the trade-off between the two studies in terms of computing speed and numerical accuracy.

The numerical results were a good match with the experimental results and demonstrated the use of COMSOL Multiphysics 4.3b to accurately simulate the settling physics as shown in Figure 15. Moreover, there was little variance observed between the computed 2-D critical velocity results to those compared with the 3-D results. The 3-D models had relatively longer computing time (> 24 hr) compared to the couple of hours it took for the 2-D models to solve. Hence, it was concluded that the 2-D models were a good enough representation and highly accurate of the settling behaviors simulated with the given material properties and future studies would not require 3-D representation.

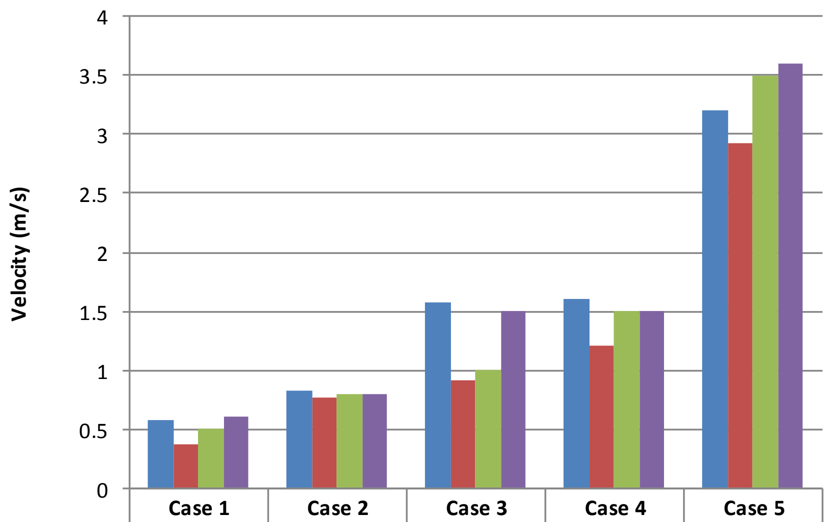

	Case 1	Case 2	Case 3	Case 4	Case 5
Empirical Correlations (m/s)	0.58	0.82	1.58	1.61	3.2
PNNL Experimental Results (m/s	0.37	0.76	0.91	1.21	2.93
FIU 3-D Comsol Results (m/s)	0.5	0.8	1	1.5	3.5
FIU 2-D Comsol Results (m/s)	0.6	0.8	1.5	1.5	3.6

Figure 15. Comparison of numerical results to experimental and empirical results.

The main problem with using the critical velocity correlations to determine the velocity of the transfer operations is that the equation is based on single component density particles forming narrowband particle size distribution (PSD). The use of the equation for multi-component density particles, broadband PSDs, and/or median particle sizes less than 100 µm (typical Hanford waste) requires extrapolation beyond the database used in the development of equation. Hence, the equation should be used with caution when applied for any of these conditions. Moreover, the PSD is assumed to be static while deriving these correlations. But in actual waste transfers, the PSD is dynamic due to precipitation, particle agglomeration, and particle-surface interactions. The correlations do not provide information about the solids volume fraction, temperature, local velocity profile, PSD, etc. along the length of the pipe nor any information on how these quantities change with time. The correlation is applicable for calculating the critical velocity of Newtonian fluids in straight, horizontal piping. When applied to non-Newtonian fluids in horizontal piping, these correlations under-predict the critical velocities [5]. Moreover, the transfer lines consists of vertical segments, pipe bends, Tee's, reducers, jumpers, connector and various other pipe components which can affect the critical velocity and plug formation process and the empirical formulae does not consider such complex piping components. Hence, future studies will include investigating the influence of pipeline components on the settling mechanics.

Additional virtual scenarios were also simulated to understand the behavior of settling as a function of flow velocity by varying particle size, solids density and solids volume fraction. The material properties used for each of these studies is described in their corresponding sections along with a brief analysis of the results observed.

C. Influence of Particle Size

The effect of particle size on the settling dynamics was investigated using 45 µm and 220 µm size solids particles dispersed in water. The solids density was kept constant at 3147 kg/m^3 and the liquid density used was 1000 kg/m^3. The solids volume fraction was 2.9%. The simulations were carried out with entrance velocities ranging from 0.8 m/s to 2 m/s. The 45 µm and 220 µm particle concentrations at different velocities are shown in Figure 16 and Figure 17. The color legend represents the different solids concentration in the pipe.

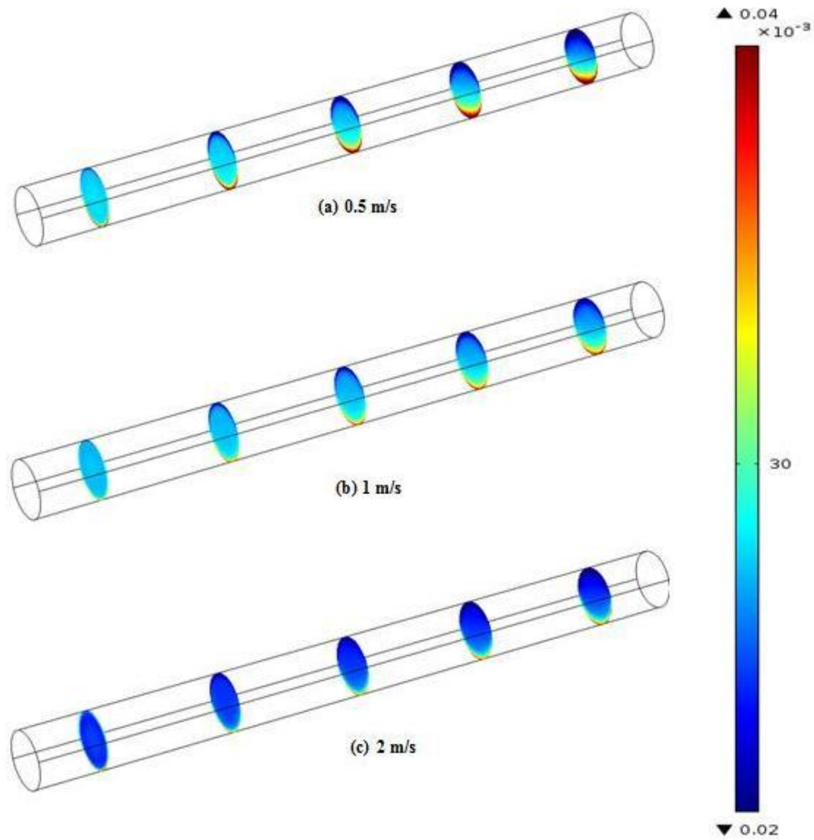

Figure 16. A 45 µm particle concentration along the pipe as a function of flow velocity ranging from 0.8 to 2 m/s.

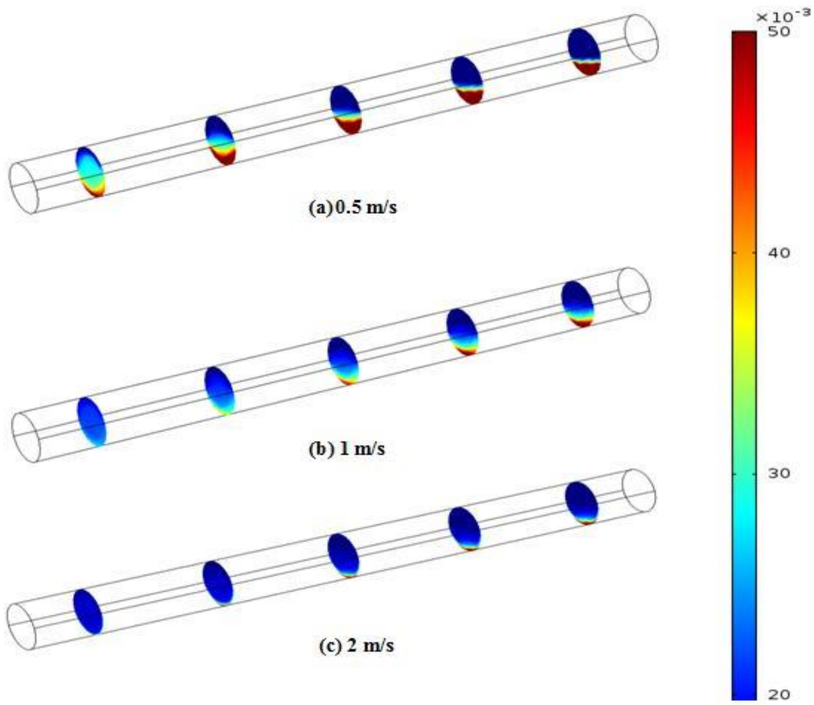

Figure 17. A 200 µm particle concentration along the pipe as a function of flow velocity ranging from 0.5 to 2 m/s.

The concentrations figures show that the 220 µm larger and heavier particles tend to settle fast on the bottom of the pipe, especially at low flow velocities. The simulations showed that flow velocities of lower than 1.0 m/s will create a stationary bed flow that eventually causes a plug to form. For velocities of greater than 1.0 m/s, the fluid establishes a moving bed regime where the particles move along the bottom of the transfer pipe.

D. Influence of Solids Density

The effect of solids density on the settling dynamics was investigated by running simulations for the 45 µm particle size and 2.9% solids volume fraction at solids densities of 3147 kg/m^3 and 6300 kg/m^3. The entrance velocities used were 0.5 m/s, 1 m/s and 2 m/s. The results of the simulations are shown in Figure 18, Figure 19 and Figure 20, respectively.

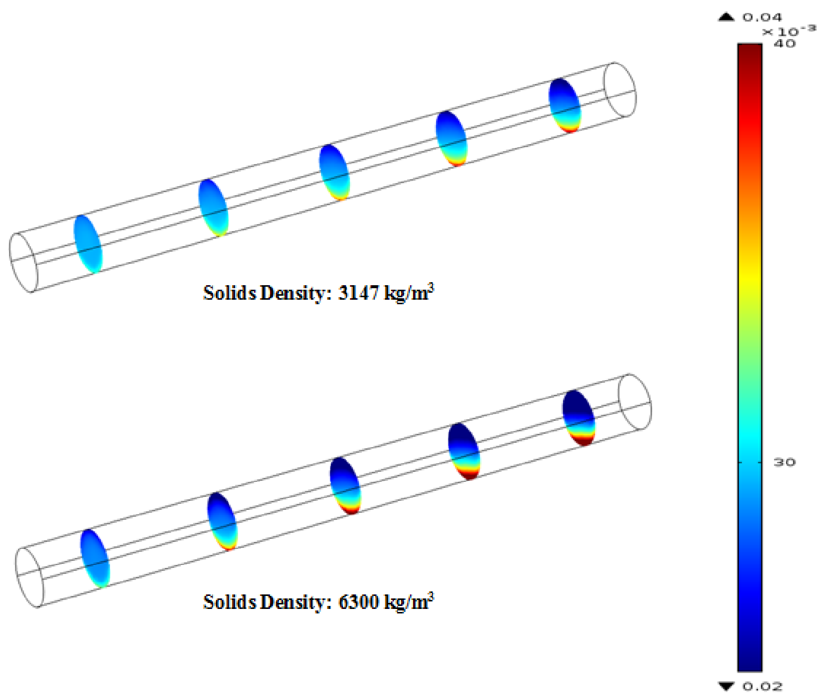

Figure 18. Settling of solids as a function of solids density for 45 µm particles at 0.5 m/s.

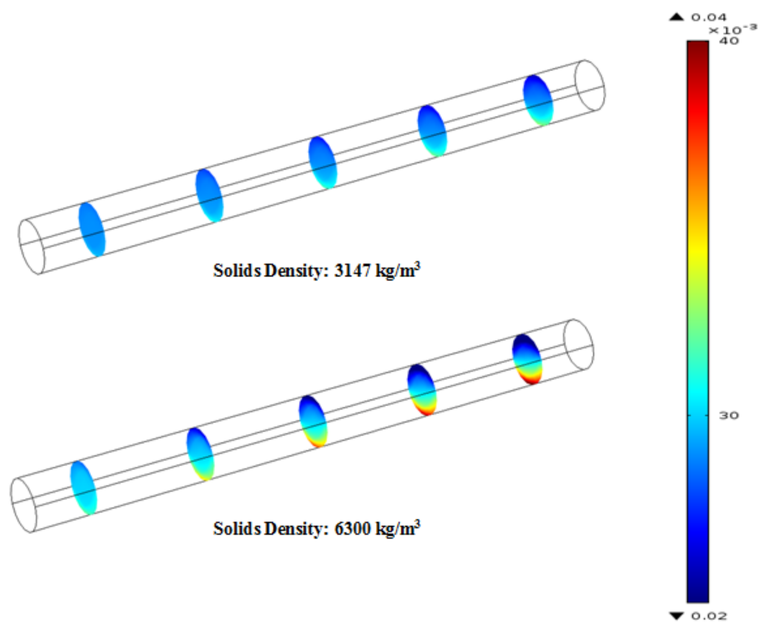

Figure 19. Settling of solids as a function of solids density for 45 µm particles at 1 m/s.

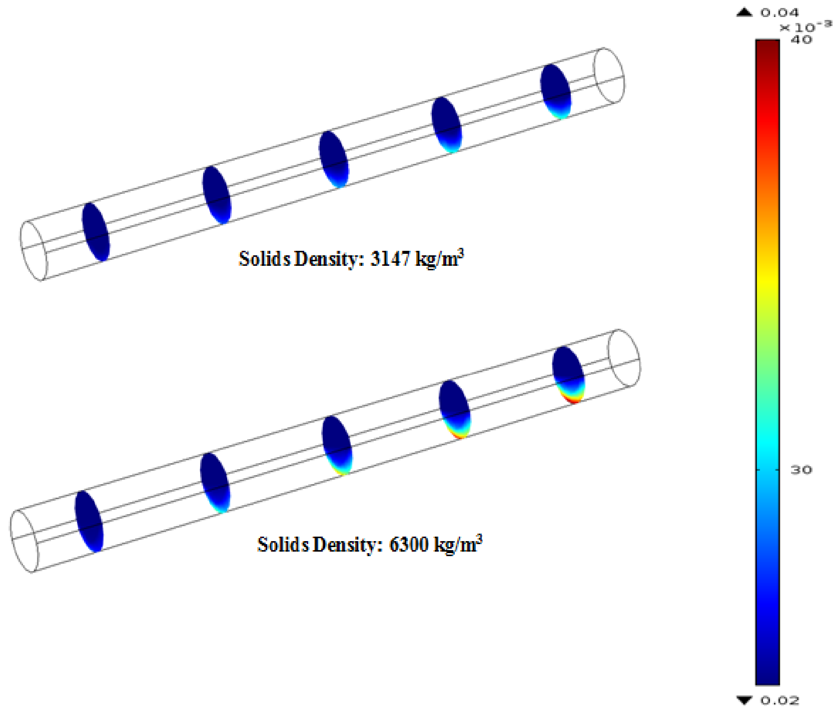

Figure 20. Settling of solids as a function of solids density for 45 µm particles at 2 m/s.

The higher density slurries require a higher velocity to keep them suspended and prevent them from settling at the bottom compared to the lower density slurries. The critical velocity for the slurries with density of 3147 kg/m^3 was 0.7 m/s compared to the 4 m/s velocity obtained for the heavier slurries with density of 6300 kg/m^3.

E. Influence of Solids Volume Fraction

The effect of solids volume fraction on the critical velocity was investigated by running simulations for 45 µm particles with a solids density of 3147 kg/m^3. The solids volume fraction values used were 2.9%, 5.8% and 10%. The liquid density was fixed at 1000 kg/m^3. The critical velocities were calculated for each case and were numerically assessed as the velocity at which the solids were fully suspended in liquid and, hence, no settling was observed at the bottom of the pipe. For example, for the slurry consisting of 2.9% volume fraction of solids, the solids were observed to settle at 0.5 m/s, 0.8 m/s, and 1 m/s. This can be seen as an increase in the solids volume fraction from the initial 2.9% to 3.53%, 3.35% and 3.27% at the respective velocities. As the velocity was further increased to 2 m/s, the solids do not settle. They remain fully dispersed across the pipe length as the solids volume fraction stays the same as the initial volume fraction value (i.e., 2.9%). Any increase in the velocity thereafter shows that the solids remain fully suspended. Hence, the critical velocity calculated for the case with solids volume fraction of 2.9% is 2 m/s. Table 6 shows the solids volume fraction values highlighted in red for the cases simulated and their corresponding measured critical velocities.

Table 6. Flow Velocity as Function of Solids Volume Fraction

Flow Velocity (m/s)	Solids volume fraction 2.9%	Solids volume fraction 5.8%	Solids volume fraction 10%
0.5	3.53%	6.84%	11.32%
0.8	3.35%	6.57%	10.98%
1	3.27%	6.42%	10.80%
2	2.90%	6.13%	10.44%
4	2.90%	5.90%	10.20%
6	2.90%	5.90%	10.12%

As the solids volume fraction increases, the critical velocity increases, as expected. For instance, for the slurry with solids volume fraction of 2.9%, the critical velocity obtained is 2 m/s compared to the 4 m/s obtained for solids volume fraction of 5.8% and 6 m/s for the slurry with solids volume fraction of 10%.

F. Influence of Pipe Geometry

The effect of the geometry of the pipelines was investigated by considering various sections, like the T-section, the vertical section and constrictions. 2D and 3D flow models were developed. Initially, a vertical section (L-section) and a section with a constriction in the pipe diameter were considered. Densities of the solid particles and fluid were taken as 6300 kg/m^3 and 1000 kg/m^3, respectively. Solid particles were 45 µm in diameter and their volume fraction was 2.9%. In the case of the vertical section, the diameter of the pipe was kept constant at 3 in. while in the other case, the diameter was reduced from 3 in to 0.75 in. Results obtained are as shown in Figure 21. The figure shows the dispersed volume fraction of the solid particles in the vertical section (red color indicates the deposition of solids) and in a constriction geometry of the pipe. It is evident that most of the particles are deposited in the pipe section with higher diameter and only a few are carried after the constriction. Hence, this could be a region for potential plug formation.

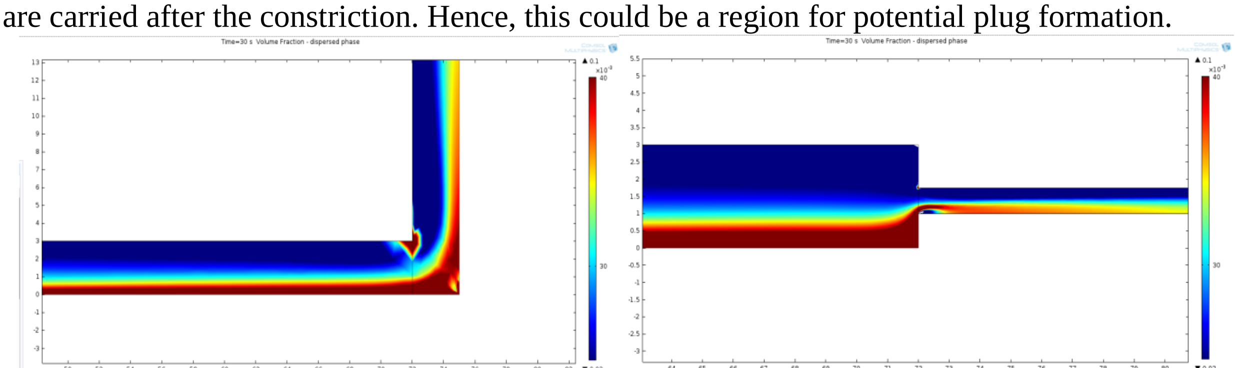

Figure 21. Settling of solids in a vertical section (left) and a constriction (right).

Next, the focus was on investigating the 2D turbulent flow based settling of solids in circular pipes with mixing of flows and variation in geometric sections. A T-section and a geometry including corners and U-sections were studied. Similar to the previous case, the densities of the solid particles and fluid were taken as 6300 kg/m^3 and 1000 kg/m^3, respectively. The flow velocities were varied from 0.5 m/s to 2.0 m/s. Two different diameters of solid particles were considered as 45 µm and 200 µm. Their volume fraction was varied from 2.9% to 10%. Geometry of the pipe sections were based on the standard 3-inch schedule 40 pipe dimensions.

Sample results obtained are as shown in Figure 22, Figure 23 and Figure 24. Figure 22 shows the dispersed volume fraction of the solid particles in the vertical T-section (red color indicates the deposition of solids). It is to be noted that the flow is input from both sides of the T-section. It mixes at the junction and the combined mixture flows through the outlet at the bottom.

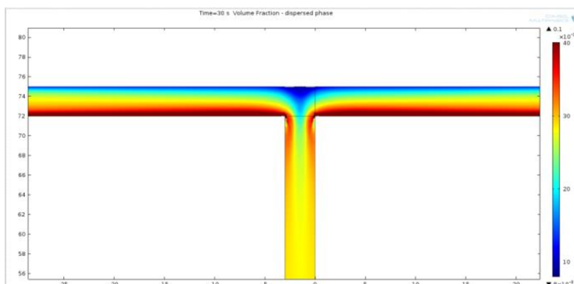

Figure 22. Settling of solids in a T- section.

A pipe section with bends, U-section and sharp corners is studied to determine the effect of settling due to complexities in the geometry of the pipes. The finite element mesh for the pipe section is shown in Figure 23 (left) and the velocity profile is shown in Figure 23 (right). As seen in the figure, there is a greater increase in the velocity at sharp corners when compared to that on the curved bends. The settling of solid particles is shown in Figure 24 for two different velocities (0.5 m/s and 2 m/s). Also the solids volume fractions considered were 2.9% and 10%. It is to be noted that in the case of lower velocity, the deposition was seen in the elbow section, straight section and the U-section of the pipe. Increasing the velocity to 2 m/s resulted in less deposition at the straight and U-sections. In this case, volume fraction was also increased by 10%.

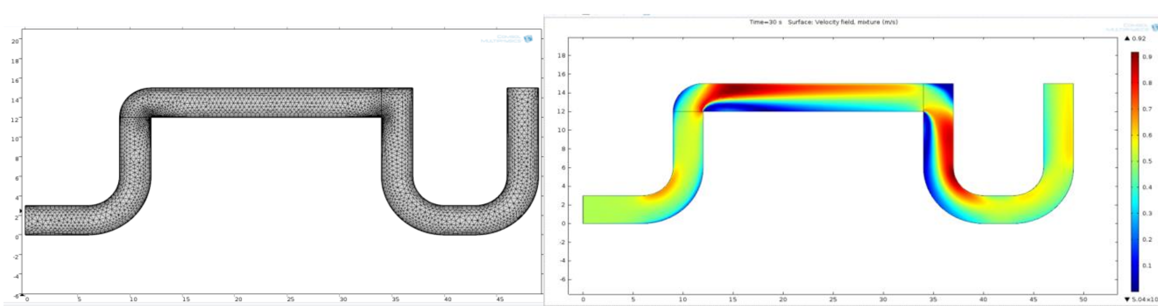

Figure 23. FE mesh (left) and velocity profile (right) for the pipe section.

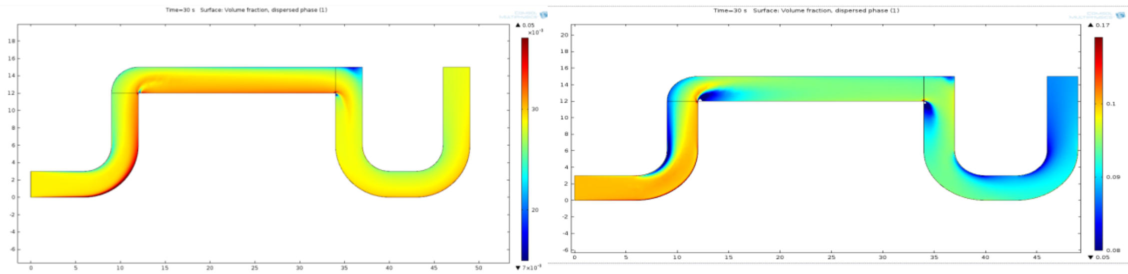

Figure 24. Settling of solids in the pipe at 0.5m/s velocity (left) and 2m/s velocity (right).

A 3D pipe geometry including horizontal, vertical and inclined sections along with elbow sections was created and modeled for the dynamic settling characteristics of solids. Solid works (Version 2013) rendering of the developed pipe model is as shown in Figure 25. Nominal diameter of the pipe is 3 inches and the loop consists of five 90° elbows with long radius. There are five straight sections and one angular section in the loop along with four vertical elbows and one horizontal elbow. The lengths of the straight sections are varied to predict the change in volume fraction of the particles flowing through the pipe loop.

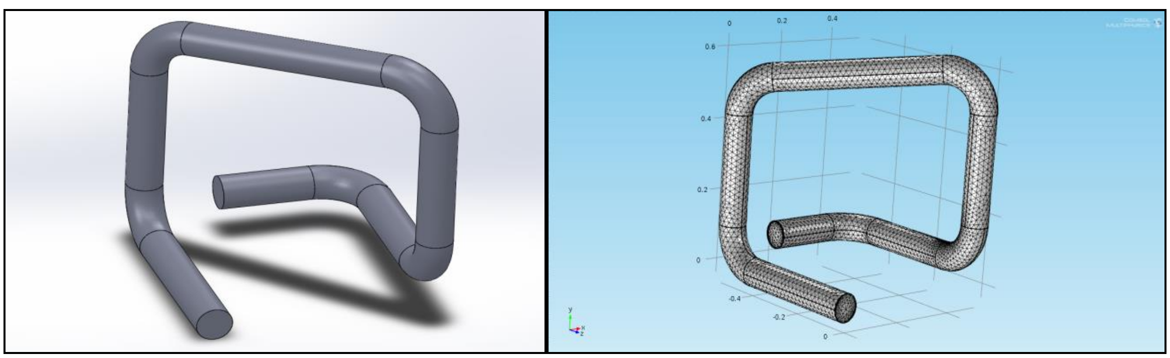

Figure 25. 3D Pipe Model (left) and FE mesh (right).

A finite element (FE) mesh was generated using COMSOL 4.3b (Figure 25). The mesh is a physics controlled mesh consisting 3D tetrahedral elements. Once the FE mesh was generated, the multiphase fluid flow module was used for modelling. Solid liquid mixture models under turbulent flow conditions were considered. Rans k-ε model was chosen for turbulence and Schiller-Naumann model was chosen for slip. A step function was used to introduce solid waste particles into the pipe loop at the inlet. Initial and inlet flow conditions were specified along with the outlet pressure condition. Densities of the solid and fluid particles were taken as 3147 kg/m^3 and 1000 kg/m^3 respectively. The flow velocities were varied from 0.5 m/s to 2.5 m/s. Solid particles with diameter of 45 µm were considered. Their volume fraction was varied from 2.9% to 10%.

Sample results obtained are as shown in Figure 26 and Figure 27. Figure 26 (left) shows the distribution of the dispersed volume fraction in the pipe loop for the case with flow velocity of 2.5 m/s and an initial solids volume fraction of 2.9%. It is evident from the figure that the volume fraction is higher (indicated by red) at the bends (elbow sections) than it is in the straight sections. The values of the volume fraction range from 2.9% to 8.9%. Hence, the elbows are regions of potential plug formations. Also, it is to be noted that the intrados of the elbows show larger deposition when compared to the extrados. This is due to the local changes in flow velocities and gravity effect. Figure 26 (right) represents the distribution of volume fraction for the case with a flow velocity of 1 m/s and an initial volume fraction of 2.9%. It is evident from the figure that a decrease in velocity by 1.5 m/s did not result in a significant change in the dispersed phase volume fraction and thus in the settlement of particles. The volume fraction in this case ranged from 2.9% to 9.1% and the pattern for volume fraction distribution remained the same as in the previous case.

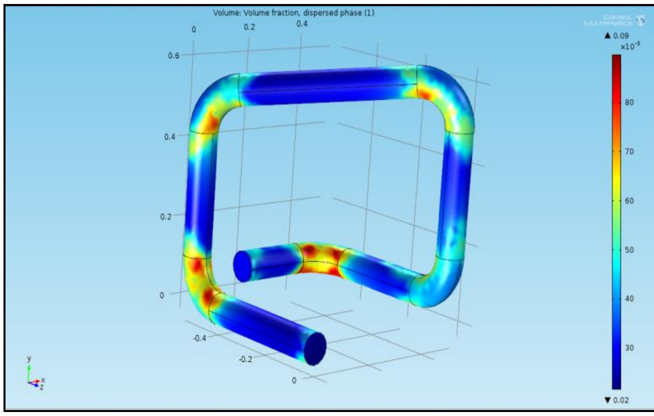

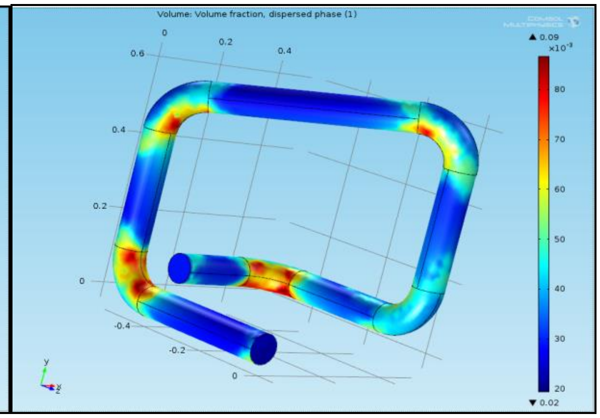

Figure 26. Settling of solids in pipe section at 2.5m/s velocity(left) and 1.0m/s velocity(right).

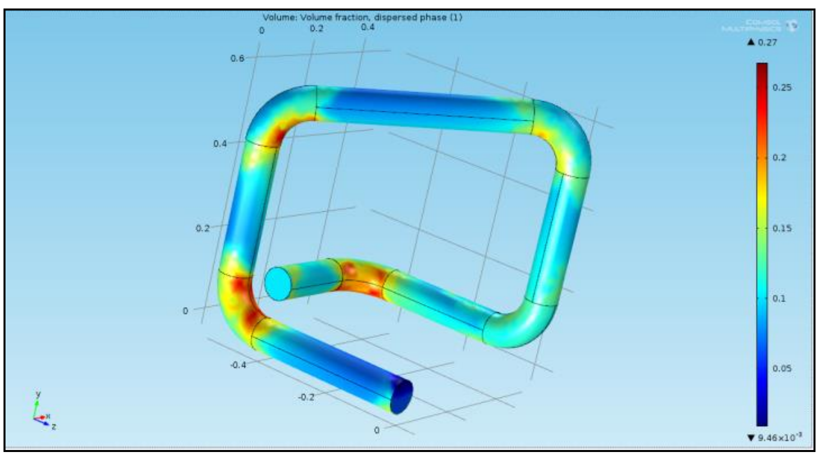

Figure 27. Settling of solids in pipe section (10% volume fraction).

In order to consider the effect of initial volume fraction on the settling dynamics, the volume fraction of the solids was chosen as 10% with a velocity of 2.5 m/s. Results obtained for the dispersed phase volume fraction of the solids in the pipe section are shown in Figure 27. As seen from the figure, the volume fraction of the solids increases from 10% to 27%. The highest value is at the elbows (indicated in red). The dispersion is similar to the previous cases. However, in this particular case, settlement of solids at the bottom of the straight sections was observed to be higher. This is due to the higher volume fraction values.

G. Settling of solids in PNNL test loop model

To investigate the settling behavior in a realistic situation, a test loop developed by PNNL is considered. A 3D pipe geometry replicating the PNNL test loop was created and modeled for the dynamic settling characteristics of solids.

A Solid works (Version 2013) rendering of the developed PNNL test loop model along with the FE mesh is as shown in Figure 28. Nominal diameter of the pipe is 3 inches and the loop consists of eleven 90° elbows with long and short radii. There are twelve straight sections in the loop along with seven vertical elbows and four horizontal elbows. The lengths of the straight sections are proportional to the PNNL test loop.

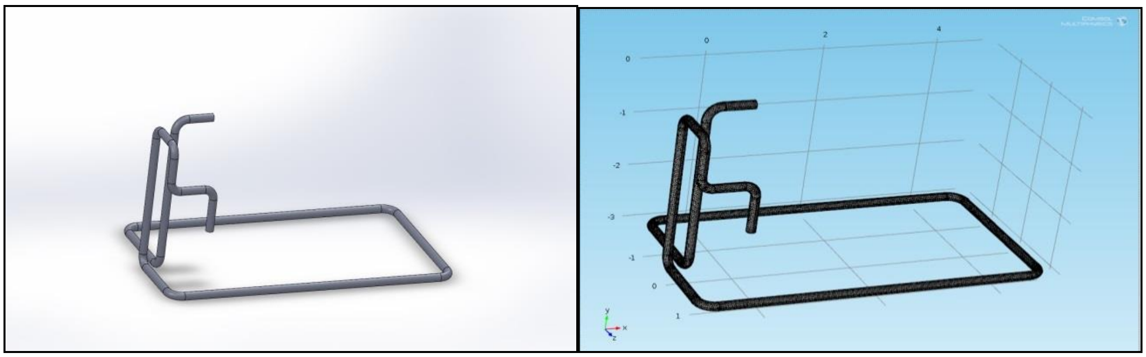

Figure 28. PNNL Test Loop Model (left) and Finite Element Mesh (right).

The FE mesh is physics controlled mesh consisting 3D tetrahedral elements. The FE mesh consisted of 348420 domain elements, 33046 boundary elements and 2146 edge elements for the analysis. Densities of the solid and fluid particles were taken as 3147 kg/m^3 and 1000 kg/m^3, respectively. The flow velocities were varied from 0.5 m/s to 2.5 m/s. Solid particles with diameter of 45 µm were considered. Their volume fraction was varied from 2.9% to 10%.

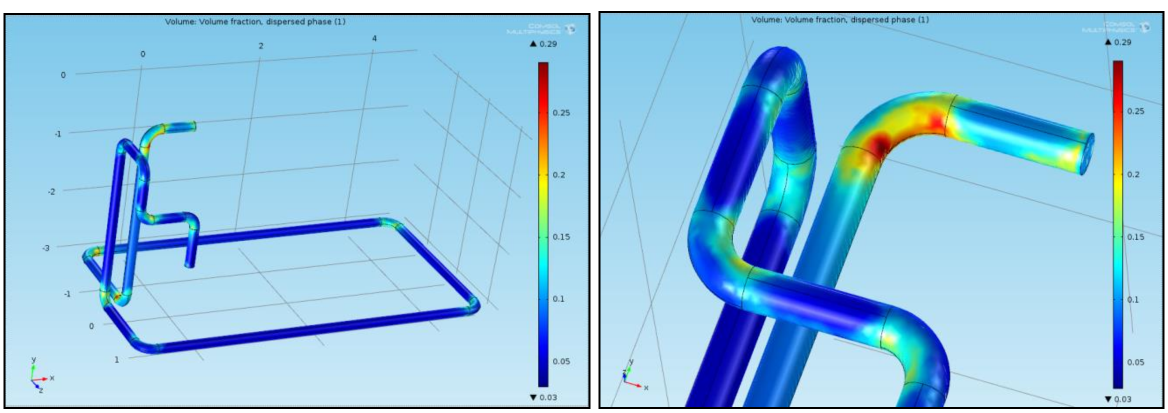

Figure 29. Settling of solids in the PNNLTest Loop (left) detailed view (right).

The sample results obtained are as shown in Figure 29, which shows the distribution of the dispersed volume fraction in the pipe loop for the case with flow velocity of 2.5 m/s and an initial solids volume fraction of 10%. It is evident that the volume fraction is higher (indicated by red) at the bends (elbow sections) than it is in the straight sections. The values of the volume fraction range from about 5% to 30%. Hence, the elbows are regions of potential plug formations. Also, it is to be noted that the intrados of the elbows show larger deposition when compared to the extrados as seen in the detailed view of the PNNL model loop. This is due to the local changes in flow velocities at the bends. In longer straight sections, the flow was stabilized and the particles well suspended, leading to a lower value of the volume fraction at the top and some deposition at the bottom of the cross section. The dispersion is similar in all the cases. However, in cases with higher initial volume fraction, the settlement of solids at the bottom of the straight sections was observed to be higher. The results obtained in the 3D simulations indicate the settling dynamics in the sample PNNL test loop.

CONCLUSIONS

During this performance period, the implementation of COMSOL Multiphysics 4.3b has been presented in simulating the settling of solids as a function of flow velocity, particle size, solids density and solids volume fraction. The efforts in investigating the chemical influence on the plug formation process were receded due to the inability of the present software to model precipitation. The 3-D numerical results simulating settling of the solids with varying rheological properties compared very well with the experimental results and empirical correlations as well as prior 2D numerical studies.

In addition, the influence of the geometry of pipelines on the settling dynamics was studied. 2D and 3D models were developed to investigate the change in volume fraction of solids at bends, constrictions and T-sections. Finally, a 3D model of a realistic system was developed based on a test loop created by PNNL. Results obtained demonstrated how particle settling is effected by pipeline geometry and can be used to assist in predicting the real-time settling of solids in Hanford’s waste transfer pipelines.

REFERENCES

1. Servin, M.A. et al., “Feasibility Study of Pressure Pulsing Pipeline Unplugging Technologies for Hanford”, Washington River Protection Solution, LLC, Richland, Washington (2012).
2. Lindner, J. S. et al. 2002. Dial/MSU Prevention of Solids Formation FY 2000 Status Report Part II: Modeling of Slurry Transport and Saltwell Pumping, reported in ORNL/TM-2000/302, Mississippi State University, Starkville, Mississippi.
3. Rector, D. R., Stewart, M. L., Poloski, A. P. 2009. Modeling of Sediment Bed Behavior for Critical Velocity in Horizontal Piping, Pacific Northwest National Laboratory, and Richland, Washington.
4. Bae K.S. et al., “Empirical Correlation for the Minimum Transport Velocity of Multidisperse Slurries in Horizontal Pipes”, Korean Journal of Chemical Engineering 8(2):120–124 (1991).
5. Poloski, A. P. et al., “Deposition Velocities of Newtonian and Non-Newtonian Slurries in Pipelines”, PNNL-17639, WTP-RPT-175, Rev-0, Pacific Northwest National Laboratory, Richland, Washington (2009).

TASK 17.2
CFD MODELING OF HLW PROCESSES IN WASTE TANKS
(FIU YEAR 5)

EXECUTIVE SUMMARY

Many engineering processes at various U.S. Department of Energy sites include the flow of nuclear waste in a liquid form that is characterized as a Bingham plastic material, a form of non-Newtonian fluids. Solid particles of varying range are suspended in the radioactive waste during mixing operations using pulse-jet mixers (PJMs). The existence of such particles makes the waste act differently than Newtonian fluids such as water, which makes it difficult to predict when engineering calculations are needed to evaluate the PJM performance. One example is the cavern formation in the upper regions of the tank where the PJMs can't produce enough flow speeds. This cavern is formed due to the nature of the nuclear waste which deforms differently based on the shear rates created in the fluid by the PJMs. The high speed jet produced by the PJMs create a turbulent flow which complicates the prediction of the size of the cavern formed by the Bingham plastic material.

Computational fluid dynamics (CFD) method is an efficient and safe approach that can provide insight into the behavior of non-Newtonian fluids by capturing the underlying physics that is represented by the governing equations of the fluid flow. Florida International University (FIU) aims to develop a CFD framework based on the Star-CCM+ software that can be used by the U.S. DOE scientists and engineers as a prediction tool for understanding the physics of fluid flow in nuclear waste tanks during regular operations and retrieval tasks.

The Star-CCM+ software was used as a direct numerical simulation (DNS) tool which utilizes a very fine mesh in order to capture the small scale details of the turbulent flows; however, DNS is computationally very expensive and only small scale problems can be analyzed with it. The goal of the current task is, therefore, to understand the behavior of the Bingham plastic material at turbulent conditions from the high fidelity simulations obtained using the DNS approach and modify the Reynolds averaged Navier-Stokes (RANS) equations in order to be able to obtain accurate simulation results at larger scales.

Initially, the DNS features of the Star-CCM+ software was evaluated against published experimental and numerical results for a Newtonian flow in a pipe. It was understood that a true DNS solver needs to be explicit in time and have a high order of discretization terms; however, Star-CCM+ software provides an implicit method with some high order terms ignored. Therefore, the DNS method provided in the Star-CCM+ method is referred to as the quasi DNS (q-DNS).

In addition, FIU evaluated the level of discrepancy for axial velocity profiles given for a Bingham plastic fluid that is flowing in a circular pipe at various conditions ranging from laminar to fully turbulent solved using the RANS approach in Star-CCM+.

A method to modify the viscosity is presented that aims to improve the results obtained with RANS; however, the results are in the process of being validated.

INTRODUCTION

The mixing performance of pulse-jet mixers (PJMs) depends on the geometry of the vessel, number and orientation of the PJMs, slurry rheology, cycle characteristics and other variables which makes the experimental evaluation a big challenge due to the large number of variables and high cost associated with building and testing the mixing process in the tanks. Computational fluid dynamics (CFD) could provide quick, safe and cost-effective predictions of the flow behavior of the nuclear sludge during PJM operation by solving the governing equations for the non-Newtonian fluid flow under turbulent flow conditions. This can yield benefits in the design estimations and performance scaling calculations for tanks where the PJMs will be used for the next 40 years in the vitrification process of the nuclear waste in the Waste Treatment and Immobilization Plant in Hanford.

In order to obtain a reliable and accurate computer model that can represent nuclear waste mixing process, all the computer software development steps must be undertaken, including the validation of the numerical method, development of an physics-based non-Newtonian viscosity model , and large-scale simulation for benchmarking. To achieve this, the CFD software chosen for this task, STAR-CCM+, is first utilized as a quasi-Direct Numerical Simulation (q-DNS) tool and is validated against experimental data for benchmark flows. Later, Reynolds-averaged Navier Stokes (RANS) and DNS simulations with a Herschel–Bulkley viscosity model was performed for a lab-scale flow problem and deviation from the experimental data was measured. The definition of viscosity was later corrected in the STAR-CCM+ software and a new model was proposed that could be used in RANS modeling of non-Newtonian fluids at full scale CFD simulations.

In this report, the evaluation of the STAR-CCM+ is first presented. The results of STAR-CCM+ q-DNS simulations for a turbulent pipe flow with Newtonian fluid are compared against available experimental data and it is shown that satisfactory results were obtained from the q-DNS simulations. Following that, inaccuracies of the RANS and q-DNS simulation results for laminar, transient, and turbulent non-Newtonian fluid flows are presented. Then, the underlying theory and numerical approach for a modification procedure in STAR-CCM+ RANS and Q-DNS simulations is presented. Finally, the feasibility of extending the procedure for implementation in the RANS simulation is discussed in the final section.

VALIDATION OF Q-DNS

In DNS, the Navier–Stokes equations are solved without any turbulence modeling and, generally, higher order numerical schemes are adopted to reduce the numerical errors. Due to very large computation requirements of DNS, a second order central scheme with 5% boundedness is considered for spatial discretization along with a second order implicit scheme for temporal discretization. This method is available in STAR-CCM+ and is referred to as a q-DNS in this report. Q-DNS was used by Shams et al. (2012, 2013-a, 2013-b) for simulation of flow around pebble configurations in hot reactors. However, due to the complexity of the flow geometry around pebbles, a simple pipe flow simulation was considered as a benchmark for code validation. A benchmark flow reference by many DNS users, like Komen et al. (2014) and Eggels et al. (1993 and 1994), and q-DNS users, like Shams et al. (2012), is the PDIV experiment of Westerweel et al. (1996). In a simple pipe flow, Westerweel et al. (1996) measured the velocity at various turbulent conditions of the flow.

Numerical Method

Benchmark data for turbulent pipe flow was extracted from the PDIV experimental findings of Westerweel et al. (1996) and the DNS simulations of Eggels et al. (1994). Guidelines for creating the computational grid were obtained from the numerical approach of Shams et al. (2012). Figure 30 shows the mesh created in comparison to the meshes that were used in other references. Compared to other referenced meshes, a very similar mesh was created at FIU but with courser elements in the axial direction, which contained 2.971 computational cells. Boundary conditions were set to match with both the experimental and numerical references; however, little information could be obtained from the references (Eggels et al., 1993; Eggels et al., 1994; Komen et al., 2014; Shams et al., 2012; and Westerweel et al., 1996) and direct correspondence with the authors regarding the conditions of turbulence at the inlet. This information was critical for sustainability of turbulence in the computational domain. Recommended values in the literature were used for the turbulent length scale and an estimate for the inlet turbulent intensity was obtained by analyzing the referenced DNS data available in the literature.

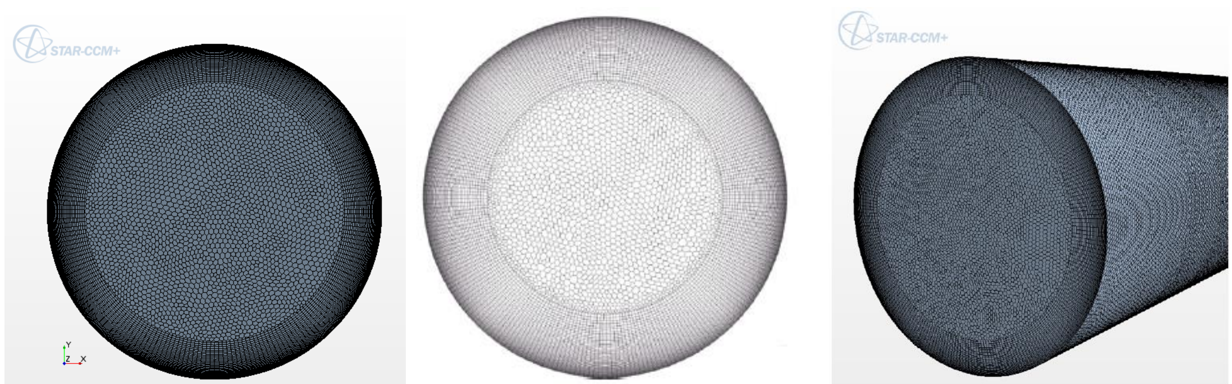

Figure 30. **Mesh for the pipe configuration(R=1m and L=10m) , (a) generated at FIU-ARC using the STAR-CCM+ program having ~2.91 mesh elements (b) generated by Shams et al. (2012) having 3.7 M elements, (c) generated by Komen et al. (2014) having 3.7 M elements.**

Simulations were performed with a sufficient amount of time to eliminate the initialization effects and achieve steady state values of the mean quantities. The time-averaging procedure was established through the creation of points at the measurement location (0.7 L from the inlet) in a traverse direction across the pipe. The simulation results from the pipe flow with almost 2.91 m grid cells are averaged over 9 seconds and are demonstrated below. In addition, simulations were performed with both water (as used in the PDIV experiment of Westerweel et al. (1996)) and air (as used in the DNS work of Eggels et al. (1993) and Eggels et al. (1994)) using the same non-dimensional parameter (Reynolds number) and scaling the mass flow rate of the fluid at the inlet. This approach helped to observe a minimal effect of viscosity on the profile of axial velocity.

Results

Q-DNS simulation results were time-averaged after a steady state condition for flow mean quantities was achieved (@~T=3sec in Figure 31). The non-dimensional velocity profile obtained from the STAR-CCM+ q-DNS, averaged over 20 seconds, is compared to the profiles of the referenced data in Figure 32. It is observed that close agreement was obtained for the values of Y+ < 30, which encompasses the viscous sub-layer and buffer layers of the turbulent boundary layer. Agreement with the experimental data could be further improved by using the originally recommended grid size of ~3.7 million, which would be pursued and reported later. The results obtained here, along with close agreements from Shams et al. (2012), who used the STAR-CCM+ for a similar exercise, can be accepted as a validation for the STAR-CCM+. The authors are confident in all the steps of mesh creation, simulation set up, obtaining time-averaged quantities and variances.

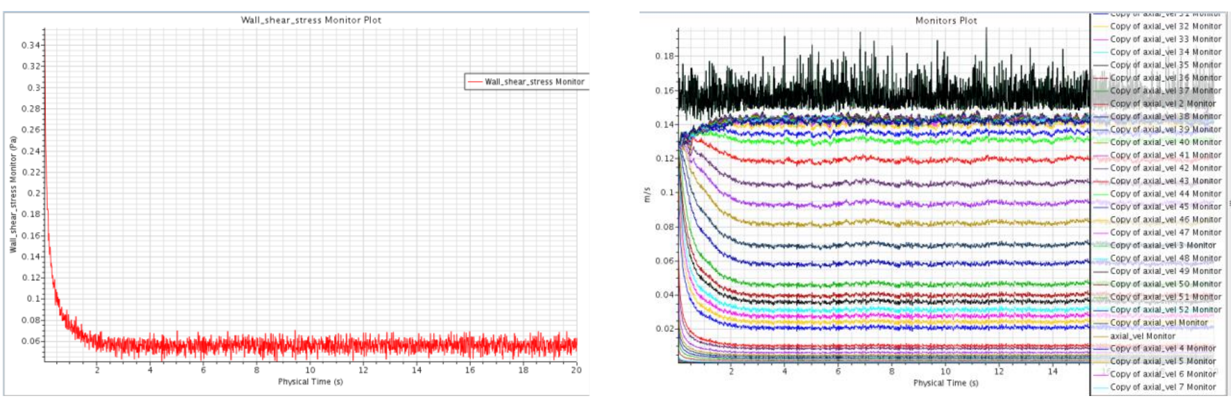

Figure 31. Steady state simulation results of Newtonian fluid flow in pipe using q-DNS STAR-CCM+ @ T=20sec. Wall shear stress on the left and velocity at different traverse locations along the probe (@ 0.7L) on the right.

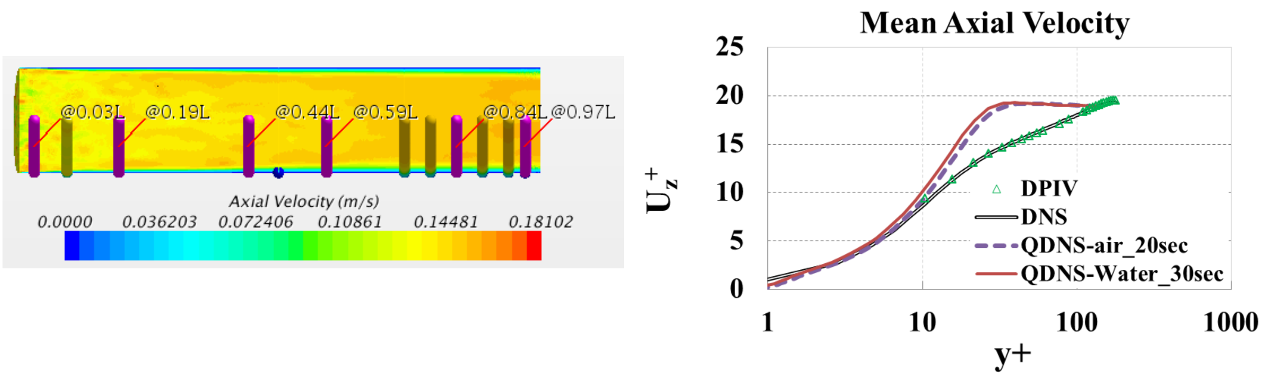

Figure 32. Q-DNS simulation results of Newtonian fluid flow in pipe. Computational domain on the left and averaged axial velocity on the right.

RANS AND Q-DNS SIMULATIONS OF NON-NEWTONIAN FLUID

Nuclear waste stored in the tanks is known to be a non-Newtonian material for its type of stress-strain dependency characteristics. Due to the existence of slurry in various applications such as pipeline transport, drilling muds and sewage sludges, and pulse jet mixing, there has been an interest in numerical studies of the flow of slurries. The stress-strain dependency, also known as the rheological property of nuclear liquid waste, can be presented by a two-parameter model like Bingham plastic or a three-parameter model like the Herschel-Bulkley rheological models. The first model is a specific type of the Herschel–Bulkley model where the exponent of the shear rate is set to unity. The choice of the model depends on the rheological information obtained from the experiments. Bartosik (2010) used both the Bingham and Herschel–Bulkley models for the Kaolin slurry using the k-ε turbulence model of Launder and Sharma (1974) with a modified damping coefficient. They observed that at low shear rates it was more advantageous to use the three-parameter model and the two-parameter model worked better for high shear rates. Malin (1997) treated the Bentonite slurry as a Bingham plastic type material in his RANS simulations using k-ε and k-ω turbulence models and found that his results were in good agreement with the experimental data. Meyer et al. (2005) introduced two types of simulants for the PJM tanks in the Handford site, a Laponite based simulant and a Kaolin-bentonite simulant. Simulant development efforts are summarized in their work and in Poloski et al. (2004a). According to Peltier et al. (2015) the Herschel–Bulkley rheological model is suitable for the slurry in PJM thanks. These researchers used the experimental data of Escudier et al. (2005) for validation of their numerical approach for pipe flow simulations with an aqueous solution of 1.5 wt% Laponite.

In this report, RANS and q-DNS modeling of the flow of non-Newtonian fluid in a pipe is presented. The purpose of these simulations was to evaluate the performance of the numerical modeling in the absence of modifications to the viscosity, which will be in part similar to investigations performed by researchers like Bartosik (2010) and Peltier et al. (2015). We aim to investigate the small scale characteristics of the flow captured with the q-DNS for the non-Newtonian fluid and improve the RANS approach using the information learned about the turbulence effects on viscosity.

A computational domain was created in accordance with recommendations from Peltier et al. (2015) for the RANS simulations in this report. Peltier et al. (2015) used a 2000-cell 2-d axisymmetric mesh consisting of prism layers and polyhedral elements for their RANS simulation. However, in this work, two 3-d computational grids consisting of 26500 and 48000 cells were created to evaluate the mesh independency of the results. The computational domains used for non-Newtonian fluid flow simulations is shown in Figure 33.

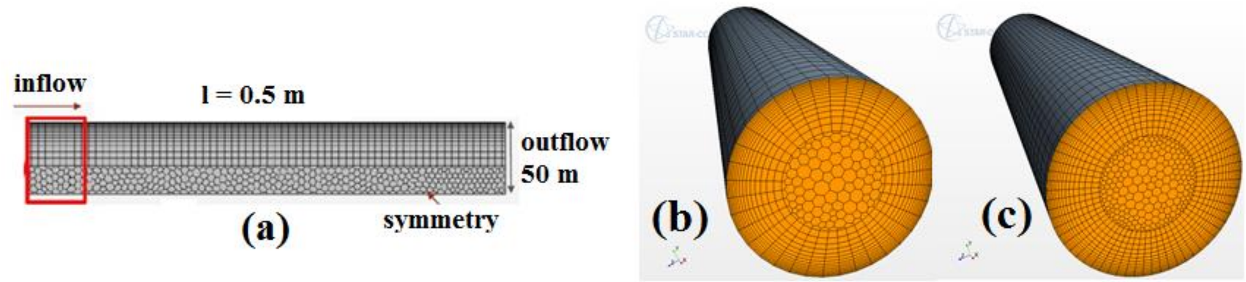

Figure 33. Computational domains used for non-Newtonian fluid flow simulations. (a) 2-d computational domain used by Peltier et al. (2015) (b) 26500 cells (c) 48000 cells.

For the q-DSN simulations, three computational grids, shown in Figure 34, were considered to investigate the sufficiency of the grid resolution in numerical modeling of the flow. A coarse mesh consisting of about 436,000 cells, an intermediate mesh of about 3.06 million cells, and a fine mesh of about 12.7 million cells were generated. An estimate of the characteristic dimensions of the mesh was obtained from the work of Shams et al. (2012) and led to the mesh with 3.06 million cells as shown in Figure 34-b. The purpose of using the coarse grid, as in Figure 34-a, was to perform a quick a-DNS analysis of the H-B model for viscosity calculations. The grid shown in Figure 34-c will be used in case non-satisfactory results are obtained with coarse and intermediate grids with modified viscosity modeling.

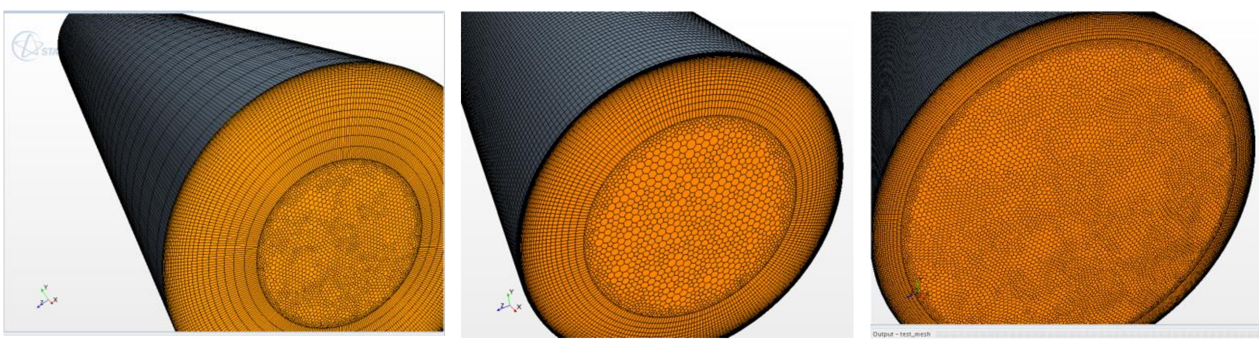

(a) (b) (c)

Figure 34. Mesh grids for Q-DNS simulations, (a)~436000 cells, (b) ~3.06m, and (c)~12.7m cells.

The k-ε model was used for the RANS modeling, while a second order scheme with 5 percent boundedness was used for the q-DNS simulations. For both approaches, the viscosity of the working fluid was modeled using the Herschel-Bulkley rheology equation. In RANS, the flow condition was changed from laminar to transient and later to turbulent, as indicated by Reynolds numbers of 550, 3400, and 25300, respectively. In q-DNS, the turbulent case with Re=25,300 was investigated. The experimental data to which Star CCM+ is compared to is documented in the reference by Presti and Escudier (1995). The referenced numerical data is from the work of Inksen N. from CD-Adapco™ [1]. The working fluid has the density of water at standard

1 http://www.cd-adapco.com/presentation/evaluation-rans-modeling-non-newtonian-bingham-fluids-turbulence-regime-using-star-ccm%C2%AE

temperature and a user defined function was created in the STAR-CCM+ to represent the Herschel-Bulkley rheology (H-B) expression of the dynamic viscosity of the fluid. The model and its coefficients are shown by:

$$\text{Viscosity modeling:} \quad \tau = \tau_Y + K\,\dot{\gamma}^n$$
$$\tau_Y(Pa) = 4.42, \qquad K(Pa\,s^n) = 0.242, \qquad n = 0.534 \tag{1}$$

where the constants are given in Presti and Escudier (1995) .

Results

Numerical results of the RANS simulations are plotted and compared against experimental data at T= 1 sec in Figure 35. These results pertain to the grid independency test at two Reynolds numbers, 550 and 25,300, and indicate no sensitivity of results to the refinement of the computational grid from 26,500 to 48,000 cells. Therefore, the referenced cell size was used for the rest of the numerical investigations. Further, to ensure that turbulence is well established in the domain, variation of the viscosity was plotted against time in Figure 36. It is clear that the viscosity of the fluid was perfectly stabilized after 0.5 sec from the start of the simulation.

However, there are clear discrepancies between the experimental data and the laminar/turbulent profiles obtained from STAR-CCM+. Figure 35 shows that viscosity is over predicted in the region close to the wall. A significantly steep profile was obtained in both laminar and turbulent cases. In contrast, in the core region (r/R $\lesssim$ 0.92), the velocity was under predicted in comparison to the experimental data in both conditions (left and right plots); however, the results show that the discrepancy is smaller for the turbulent case in both the wall and core-regions of the pipe flow.

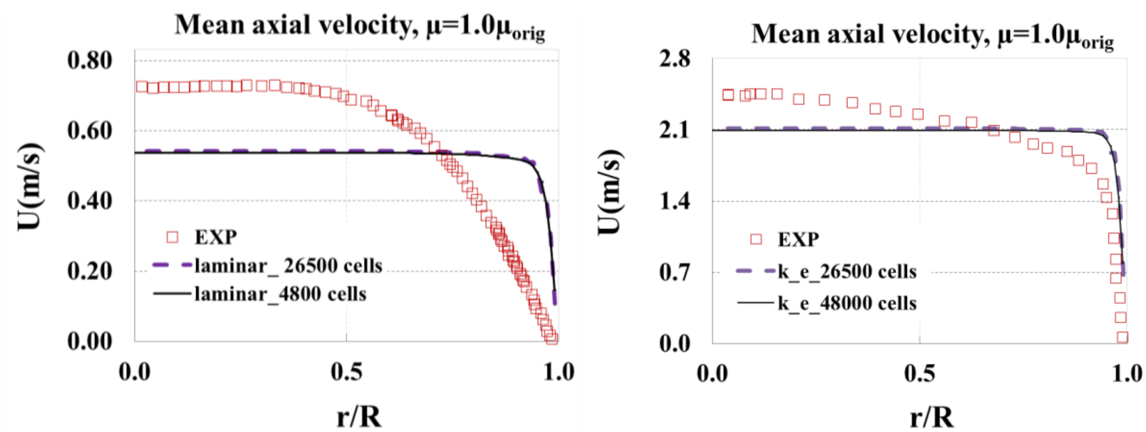

Figure 35. Profile of axial velocity at Reynolds = 550 (left) and Reynolds = 25300 (right). @ T= 1.001 s.

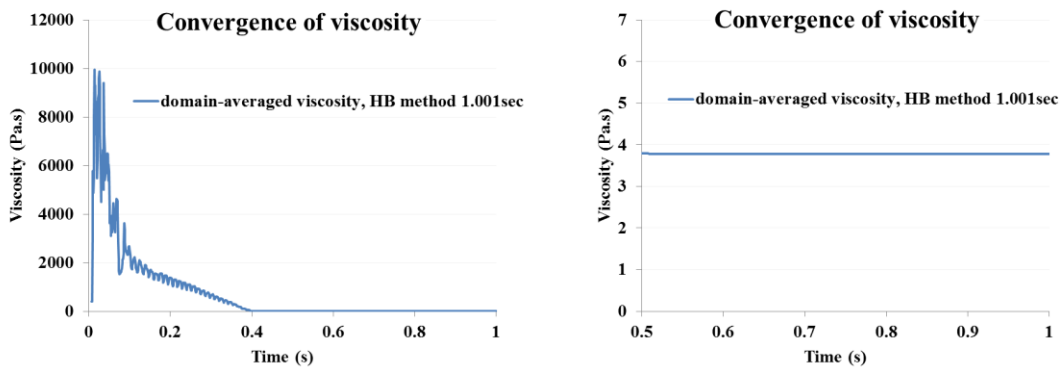

Figure 36. History of viscosity variation in RANS simulation.

Furthermore, Figure 37 shows a comparison of the results obtained at Re =550, 3,400, and 25,300 for the RANS simulation. Herein, the results are compared against the RANS simulation results published by Peltier et al. (2015) and experimental data available in publication of Escudier et al. (2005). In all cases, the RANS modeling with STAR-CCM+ predicted steeper profiles in a region close to the solid boundary. The velocity is under predicted in the core region and generally better results were obtained by Peltier et al. (2015), who used the k-ω turbulence model. The results show that differences between k-ε and k-ω are amplified by increase in the Reynolds number.

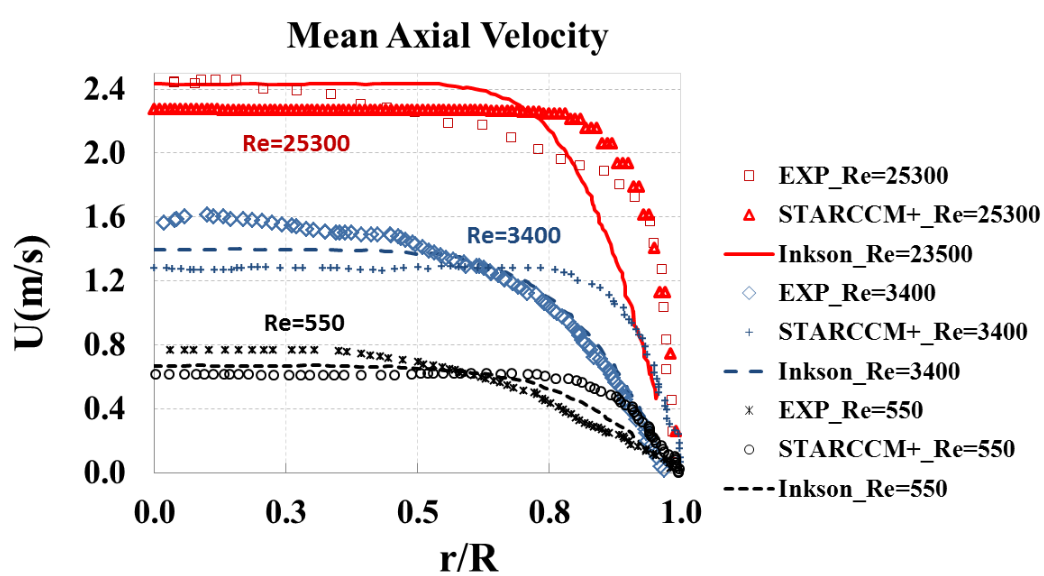

Figure 37. Comparison of velocity profiles from this work (RANS) with numerical data published by [Peltier et al., 2015] and experimental data available in publication of [Escudier et al., 2005].

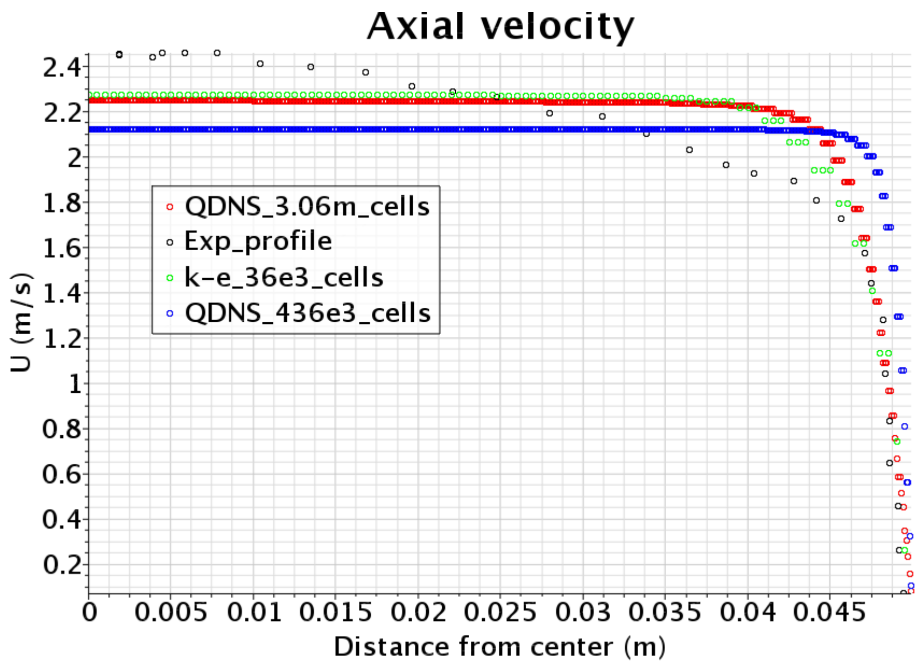

Figure 38. Simulation results generated by Q-DNS and RANS (k-ε) compared to experimental data published by [Escudier et al., 2005].

VISCOSITY IMPLEMENTATION IN RANS AND Q-DNS

According to Tennekes (1968), eddies are known by their velocity scale (ú) , length scale (Í), and time scale ($T = \frac{Í}{ú}$). Table 7 shows the characteristic of eddies in the turbulent flow. According to the cascade theory, viscous dissipation of turbulent kinetic energy occurs in micro scale eddies or dissipative eddies. These eddies are strongly affected by viscosity and can account for significant differences between the Newtonian and non-Newtonian fluids under the same flow geometry and initial and boundary conditions. The average rate of dissipation of turbulent kinetic energy can be quantified as $\hat{\varepsilon} = \overline{0.5 \times \nu \left(\frac{\partial u_i}{\partial x_j} + \frac{\partial u_j}{\partial x_i}\right)\frac{\partial u_i}{\partial x_j}}$ or simply as $\hat{\varepsilon} = \hat{\tau} \times \hat{s}$. In this definition, x and u, $\hat{\tau}$, and $\hat{s}, \nu$ represent the Cartesian (or other coordinate systems) components of the coordinates, components of the velocity shear stress, instantaneous shear stress and the rate of shear, and kinematic viscosity, respectively. A strong dependency of the dissipation rate (ε) on the strain rate is a key to the modification of viscosity in CFD modeling. Burden (2008) references Tennekes and Lumley (1972) and Mathieu and Scott (2000) and provides the definition of the instantaneous dissipation rate as shown by Eq. (2). For dissipative scales, the fluctuation and mean terms of the strain rates can be described by Eq. (3) and Eq. (4), respectively; however, one can calculate the mean term (i.e., $S_{ij}S_{ij'}$) from the expression of $0.5\times\left(\frac{\partial U_i}{\partial x_j} + \frac{\partial U_j}{\partial x_i}\right)$, where U is the mean (or time averaged) velocity. STAR-CCM+ RANS simulations provide the mean strain rate as their temporary storage values at the end of each iteration; however, with the STAR-CCM+ q-DNS simulations, the user has to either find the mean values, or use Eq.(4), where the turbulent Reynolds (Re_T) number is required which is given as: $Re_T = \frac{u_\tau \ell}{\nu}$.

Here, u_τ is the frictional velocity defined as $u_\tau = \sqrt{\tau_w/\rho}$, τ_w is the kinematic viscosity and ρ is the characteristic length usually taken as the pipe radius. τ_w and ρ are the wall friction and fluid density, respectively.

$$\langle \hat{s}_{ij}\hat{s}_{ij}\rangle = S_{ij}S_{ij} + \langle s'_{ij}s'_{ij}\rangle \tag{2}$$

$$< \acute{s}_{il}\acute{s}_{il} > = \frac{1}{2t_k^2} = \frac{\nu^2}{2\eta^4} \tag{3}$$

$$S_{ij}S_{ij} = \frac{<\acute{s}_{il}\acute{s}_{il}>}{2\,Re_T} = \frac{\nu^2}{4Re_T\eta^4} \tag{4}$$

In these definitions, $\hat{s}_{ij}$, t_k, and η are the instantaneous strain rate, Kolmogorov time scale, and Kolmogorov length scale, respectively. The definitions of these parameters are available in Table 7. Gavrilov and Rudyak (2014) introduced the definition of the fluctuating rate of energy dissipation as $\varepsilon = 2\nu\langle s'_{ij}s'_{ij}\rangle$ and, by replacing the right hand side term of Eq. (2), provided a link between the strain rate to the turbulent dissipation rate in the RANS. Eq.(5) shows the modified form of the instantaneous strain rate modules.

$$||\dot{\gamma}||^2 = 2\langle \hat{s}_{ij}\hat{s}_{ij}\rangle = 2S_{ij}S_{ij} + \varepsilon/\nu \tag{5}$$

Gavrilov and Rudyak (2014) used this method to modify the Herschel‑Bulkley viscosity definition, Eq. (1), in their RANS simulation and obtained significant improvements in comparison to the original power law model. Since this approach is not particular to a specific flow or geometry condition, it is considered a general approach for the simulation of non-Newtonian fluids. A more advanced method was used by Peltier et al. (2015) who used a modified definition of strain rate based on the direct use definition of fluctuating strain rate tensor similar to Eq.(3) instead of obtaining the ε from the transport equation. These researchers obtained results in close agreement with the experimental data for simple pipe flow using k-ω RANS modeling.

In addition to the work of Gavrilov and Rudyak (2014), literature contains a number of viscosity models proposed for the flow of non-Newtonian fluids (Thomas, 1963a&b; Soto and Shah, 1976; and Wilson and Thomas, 1986). According to Escudier and Presti (1996), Soto and Shah (1976) improved the theory for the Herschel-Bulkley fluid in the entrance region of the flow. Wilson and Thomas (1986) improved the theory of the power-law and Bingham plastic categories for the log-law region of the velocity profile towards better prediction of the wall friction coefficient. This modification reflected an enhanced viscosity effect at the small time and length scales of the dissipative micro-eddies.

Herein, our attempt is to use the fundamental theory of non-Newtonian fluids which relates the stress to the strain rate in order to obtain a modification that spans the entire computational domain. It is possible to define the coefficient α as the ratio of the area under the stress-strain curve of a Bingham plastic fluid to the area under the Newtonian curve, as shown in Figure 39(a). We define a pseudo-Newtonian viscosity as the slope of the line that connects the origin to the point of maximum stress on the Bingham plastic curve. According to Wilson and Thomas (1986), the dissipation rate of turbulent energy in a Newtonian fluid with viscosity of $\alpha \times \eta$ will be the same as the dissipation rate in a non-Newtonian fluid with tangential viscosity of η, where $\eta = \frac{\sigma}{du/dy}$. According to Figure 39(b), dissipation can occur in the entire computational domain and predominantly in the viscous sub-layer, where only dissipative eddies can be present. Therefore, by multiplying the α coefficient to the pseudo-Newtonian viscosity, it is possible to modify the viscosity, μ, in an iterative and corrective fashion. The explanation of this procedure is that one can start with a viscosity obtained from a non-precise method, such as the Herschel-Bulkley method, and obtain the entire flow field. In the next step, at the end of each iteration, the graph in Figure 39(a) can be reconstructed and α can be obtained. The correction to the viscosity can then be obtained using the expression, $\mu_{\text{micro eddies}} = \alpha * \frac{\sigma}{du/dy}$ where, $\boldsymbol{\sigma}$ is the shear stress. The calculation of α can be done using Eq. (6). This correction is performed to update the entire velocity field and the iterative procedure will continue until convergence is attained. In this approach, it is critical to separate the dissipative eddies through different methods. This scale separation can be performed using criteria such as a high dissipation rate of turbulent kinetic energy and a large strain rate modulus based on the energy spectrum shown in Figure 40.

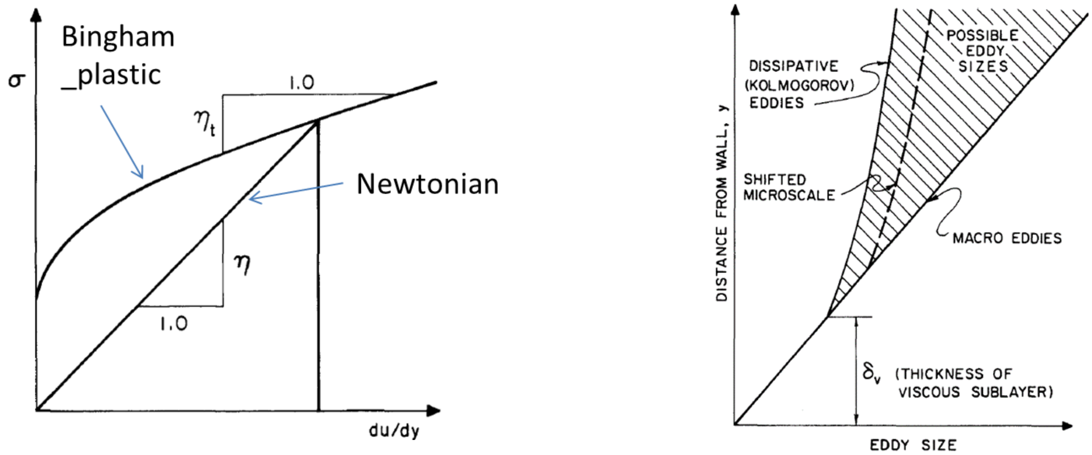

(a) (b)

Figure 39. Characteristics of the non-Newtonian fluids (a) the typical rheogram (b) eddy size, in turbulent flow, Wilson and Thomas (1986).

Table 7. Characteristics of Scales in Turbulence

	$\acute{u}$	$\acute{l}$	T	Dissipation rate of energy	Transfer of energy	Re	Fluctuation of Strain rate
Kolmogorov scale eddies	$(\nu\varepsilon)^{1/4}$ $=\nu/\acute{l}$	$\eta=\left(\frac{\nu^3}{\varepsilon}\right)^{1/4}$ $=\nu/\acute{u}$	$\frac{\acute{l}}{\acute{u}}=\left(\frac{\nu}{\varepsilon}\right)^{1/2}=\frac{\eta^2}{\nu}$	Viscous dissipation $\varepsilon=\frac{\upsilon\,\acute{u}^2}{\acute{l}^2}=\frac{\upsilon^3}{\eta^4}$ Isotropic dissipation $\tilde{\varepsilon}=\nu\left\langle\frac{\partial u_i'}{\partial x_l}\frac{\partial u_i'}{\partial x_l}\right\rangle$ $\varepsilon=\left\langle 2\nu s_{il}'\frac{\partial u_i'}{\partial x_l}\right\rangle=2\nu\langle s_{il}'s_{il}'\rangle$	NA	1	$\langle s_{il}'s_{il}'\rangle=\frac{1}{2t_K^2}$
Large scale eddies	u_T	l_T	l_T/u_T	NA	$\frac{u_T{}^3}{l_T}$	$\frac{u_T.l_T}{\upsilon}$	$\mathrm{Re}_T^{-1}\times\langle s_{il}'s_{il}'\rangle$
Intermediate scales $\eta \ll l \ll l_T$	$u=(\varepsilon l)^{1/3}$	ℓ	$\left(\frac{l^2}{\varepsilon}\right)^{1/3}$	NA	$\tilde{\varepsilon}=\nu\left\langle\frac{\partial u_i'}{\partial x_l}\frac{\partial u_i'}{\partial x_l}\right\rangle$	$Re_T=\frac{u.\ell}{\upsilon}$	$\mathrm{Re}_T^{-1}\times\langle s_{il}'s_{il}'\rangle$

$$\alpha=\frac{\int_0^{\dot{s}_{max}}\tau\dot{s}\ d\dot{s}_{\text{H-B}}}{0.5\times(\dot{s}_{max})_{\text{H-B}}\times(\tau)_{|\dot{s}_{max\ \text{H-B}}}} \tag{6}$$

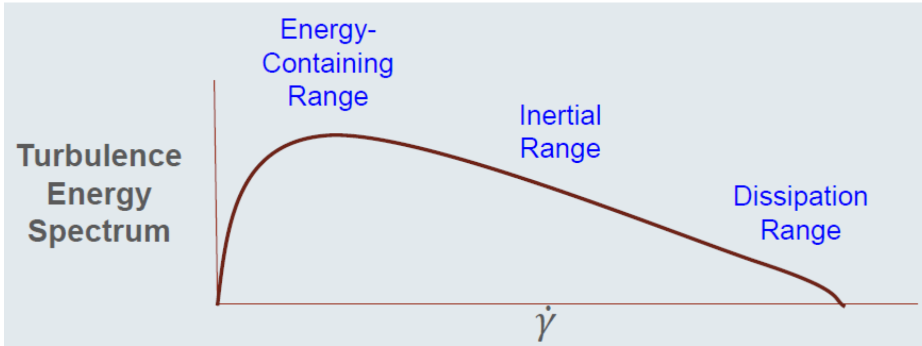

Figure 40. Energy spectrum in turbulence, Peltier et al., (2015).

In the next section, the methodology used for viscosity modification and the effectiveness of the proposed method will be discussed.

Numerical Method

In this section, a method of modification for the viscosity based on turbulent scale separation is proposed and investigated. We adopted the method of modification based on the Wilson and Thomas (1986). Two strategies were introduced to the STAR-CCM+ through Java scripting in order to identify the effective region of the viscosity and separate the scales: one based on a threshold for the dynamic viscosity, Eq. (7), and the other based on the threshold for the dissipation rate, Eq. (8). The first strategy was aimed to directly study the viscosity effect on the numerical results and the second strategy was aimed to more realistically separate the viscosity-effective scales (scales with length scales smaller than the Taylor length scales) from the rest of the scale.

$$\text{strategy \#1}: \begin{cases} \mu = \mu_{H-B} & \mu_{H-B} \geq \mu_{psudo\_Newt.} \\ \mu = \alpha \times \mu_{psudo\_Newt.} & \mu_{H-B} < \mu_{psudo\_Newt.} \end{cases} \tag{7}$$

$$\text{strategy \#2}: \begin{cases} \mu = \mu_{H-B} & \varepsilon_{H-B} < \varepsilon - THS \\ \mu = \alpha \times \mu_{psudo\_Newt.} & \varepsilon_{H-B} \geq \varepsilon - THS \end{cases} \tag{8}$$

The performance of the proposed method for modifying the viscosity of Bingham-plastic materials was tested in a turbulent pipe simulation. The details of the boundary condition and flow geometry are available in the publications of Peltier et al. (2015) and Escudier et al. (2005). The computational domain created in Figure 33-b was used for the present study. The effectiveness of the method was evaluated in a RANS simulation with the k-ε turbulence model, initialized with a Herschel-Bulkley model. The implemented viscosity model has the expression and constants shown by Eq. (1). The value of the alpha was numerically calculated based on the maximum of strain rate modulus from Eq. (6) and was used to modify the Herschel-Bulkley viscosity obtained from the previous iteration. The results of the RANS simulations after the implementation of the proposed methods were compared against the experimental data values.

Results

Simulation results of the first and second strategies showed a difference in the effective area of manipulation as shown in Figure 41. The results show a reduced number of cells needing manipulation in Figure 41-b shown by blue symbols in the same effective area ($\varepsilon > 30\ m^2/s^3$). Figure 41-c shows the significant change in the effective area in the case of the second strategy, which was the original purpose of defining this strategy. The goal for this significant increase of the effectiveness area (i.e., ε-THS= a small number = 1.44) was to involve more computational cells in the viscosity manipulation. Figure 42 shows the manipulation of the stress-strain profile as a result of both strategies. These results have been obtained after 50 time steps (5000 iterations) from the start of the manipulations. In Figure 42-a and Figure 42-b, the red line is the H-B curve and the green color indicates the modified stress-strain profile. As we can see, the deviation from the H-B curve is considerably more in the second strategy. In fact, the stress-strain profile has been dynamically adapting to the dynamically changing $\alpha^* \mu_{psudo\_Newt.}$. This has changes in the behavior of the material from a pure shear thickening after the yield stress to shear-thickening-shear-thinning after the ε-THS.

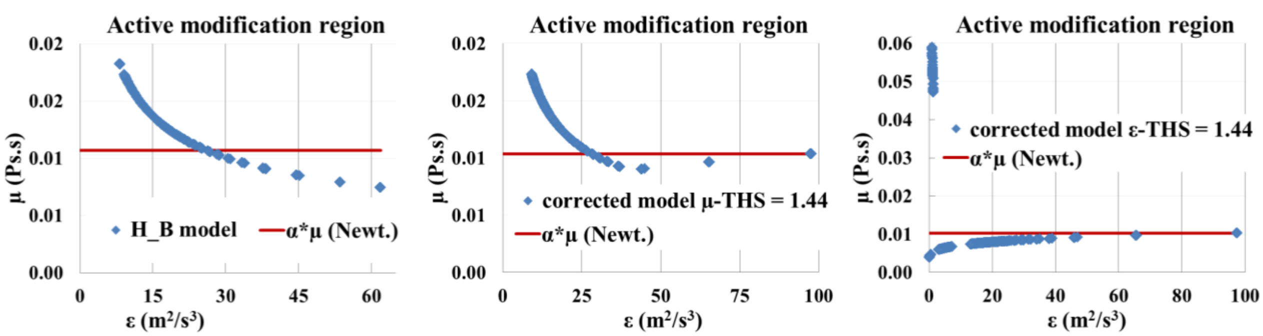

(a) (b) (c)

Figure 41. Simulation results of the first and second strategies, (a) original effective area obtained from non-modified RANS simulation, (b) effective area of strategy #1: $\mu_{H-B} < \mu_{psudo\_Newt.}$ (c) effective area of strategy #2 : $\varepsilon_{H-B} \geq \varepsilon - THS$.

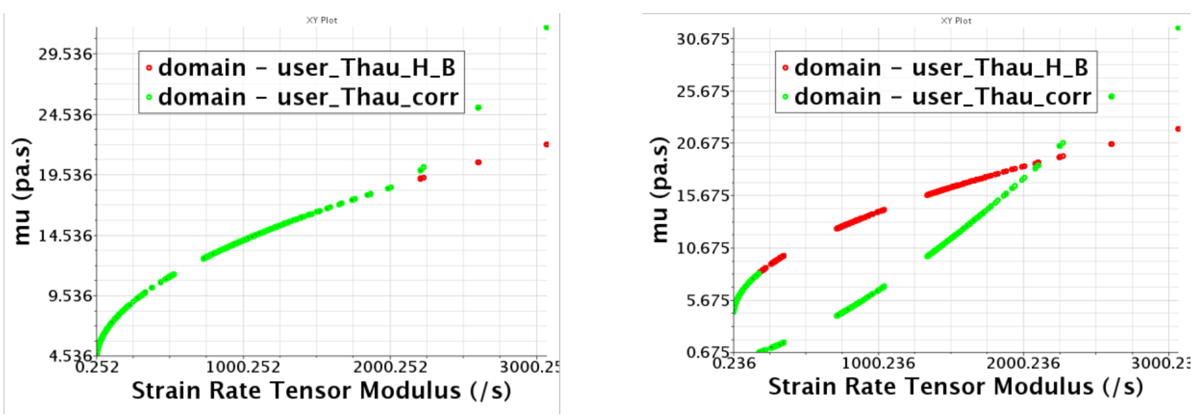

(a) (b)

Figure 42. Manipulation to the stress-strain profile (a): strategy #1 (b); strategy#2, results @T=10.05sec, (red shows the H-B profile and green shows the modified viscosity profile).

Finally, we have calculated the effect of the viscosity manipulation on the profile of velocity. Figure 43-a,b show that both strategies could not improve the velocity profile of the H-B model. Figure 44 shows a comparison between the profiles of dissipation rate and strain rate modulus before and after implementation of the manipulation to viscosity. As a result of this manipulation, a significantly higher dissipation rate and strain rate are observed. In fact, an increase of viscosity increases the strain rate and the first cell next to the wall possessed a significantly higher velocity due to this more rapid velocity change from zero at the wall. The ineffectiveness of such fundamental approaches is seen in the excessive increase of shear rate and shear stress in the boundary layer and thus dramatic increases of U+ in the near wall region. This effect was more pronounced by further decreasing the ε_THS to 0.01, as shown by the solid blue line in Figure 43-b. This has led to a noticeable deviation of the velocity profile in the wall-region of the domain. This effect is absent in the closer-to-core region of the pipe flow (r/R <0.9), where RANS was unable to capture the fine scales due to the averaging procedure, as opposed to the near to wall region where all scales are dissipative. Therefore, an investigation of both strategies presented in this report in the SARCCM+ Q-DNS simulations will be pursued in a future task.

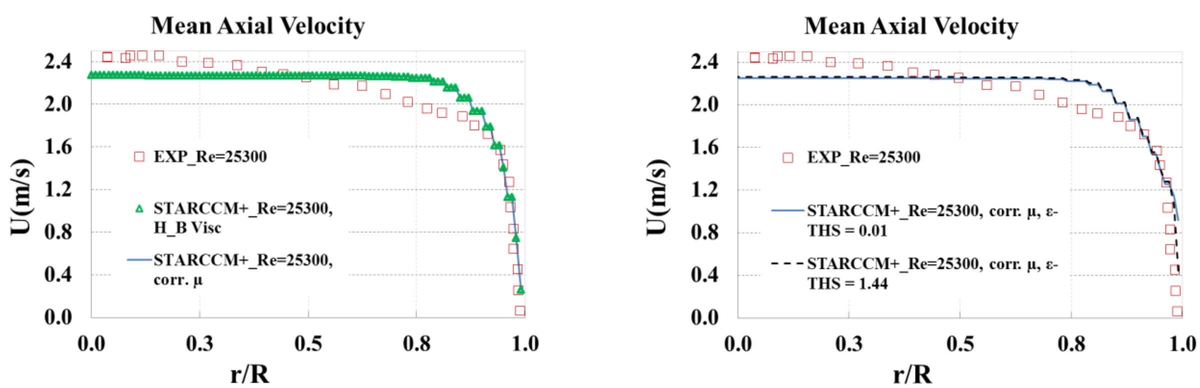

(a) (b)

Figure 43. Change in the velocity profile after using two strategies in RANS simulation (a) strategy #1, μ-THS = 1.44 and (b) strategy #2, ε_THS = 1.44 and ε_THS =0.01.

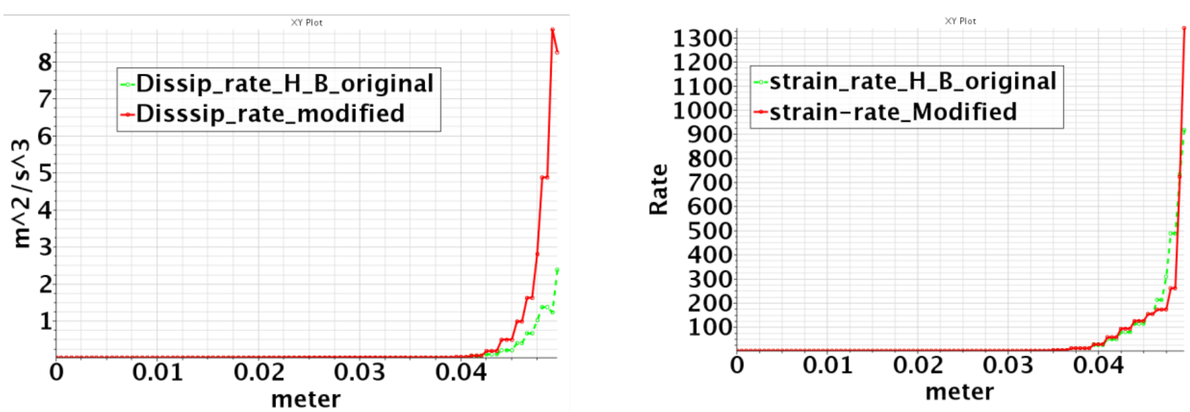

(a) (b)

Figure 44. Comparison of the simulation results before and after the viscosity manipulation.

CONCLUSIONS

In this work, validation of the q-DNS was initially performed for turbulent pipe flow of Newtonian fluids. Using 3 million mesh elements, close agreement was obtained between the q-DNS simulation results and the experimental data in the viscous sub-layer and the buffer layer of the turbulence boundary layer. In the outer layer of the boundary layer, the agreement could be improved by increasing the number of cell elements to almost 6 million elements. In the pipe flow simulation of the non-Newtonian fluid using the original form of the Herschel-Bulkley, results of the RANS and q-DNS simulations were not acceptable once compared to the experimental data. The choice of different turbulence models (k-ε vs k-ω) and dimensions of the problem (3-d vs 2-d) are possible reasons for the deviation from the reference numerical model; however, both the reference numerical model and the present work deviate from the experimental data, which calls for the need for correction to the strain rate modules and, hence, viscosity modification.

Additionally, a method for a direct correction based on the overall dissipation rate of energy was proposed for RANS simulations using STAR-CCM+. Two strategies were used to separately define the modification region based on the thresholding viscosity and dissipation rate. Results show the slight sensitivity of the model was not due to thresholding of the viscosity since the original data was re-obtained; however, thresholding of the dissipation rate involved significantly more computational cells in the viscosity manipulation and a strong deviation in the stress-strain curve was observed. This effect significantly increased the strain rate and dissipation rate, resulting in a dramatic increase of velocity in the wall region. This effect was absent in the core region because of the averaging nature of the RANS. The issue of insensitivity to manipulation of viscosity in the regions away from the solid boundaries will be evaluated by testing the proposed method in q-DNS. In addition, the implementation of the method proposed by Gavrilov and Rudyak (2014) in RANS can be extended by modification of the strain rate using Eq. (3) and Eq. (4) combined in q-DNS simulations. This implementation in q-DNS within STAR-CCM+ and extension of the results to RANS within STAR-CCM+ could provide a more robust application of STAR-CCM+ in simulations of nuclear slurries in future contributions to the present research.

REFERENCES

1. Burden T, The Length, Time and Velocity Scales, Lecture notes (2008), www2.mech.kth.se/courses/.../scales.pdf.
2. Space and time scales of turbulence, (2000). pp 57–61, in ‘An introduction to turbulent flow’, J. Mathieu & J. Scott, C.U.P.
3. Eggels, J.G.M., Westerweel, J., Nieuwstadt, F.T.M., Adrian, R.J. (1993), Direct numerical simulation of turbulent pipe flow: A comparison between simulation and experiment at low Re-number. Appl. Sci. Res., vol. 51, pp. 319-324.
4. Eggels, J.G.M. (1994), Direct and large eddy simulation of turbulent flow in cylindrical pipe geometry, Thesis, Delft University of Technology, Netherlands.
5. Escudier M.P., Presti F., (1996), Pipe flow of a thixotropic liquid, J. Non-Newtonian Fluid Mech., volume 62, PP. 291-306.

TASK 18.1
EVALUATION OF FIU'S SOLID-LIQUID INTERFACE MONITOR FOR RAPID MEASUREMENT OF HLW SOLIDS ON TANK BOTTOMS (FIU YEAR 5)

EXECUTIVE SUMMARY

FIU has tested and continues to test its profiling sonars for use in Hanford high-level radioactive waste (HLW) mixing (conditioning) tanks. The waste processing operations need to ensure that mixing by pulse-jet mixers (PJMs) is thorough and that solids are completely suspended and removed with each batch. Therefore, a technology that is able to image through the turbulent liquid and entrained solids during mixing and verify that no solids remained on the floor would allow operators to know that the waste was completely suspended and able to be transferred out of the tank for further processing. This task was initiated in October 2013 after discussions with engineers at Pacific Northwest National Laboratory (PNNL) and at the Department of Energy's (DOE's) Savannah River Site (SRS). In 2015, significant interest was also shown by a different group at PNNL for use of FIU's sonars related to mixing tanks in the Waste Treatment and Immobilization Plant (WTP). FIU's sonars are custom-built, commercial sonars for which FIU has developed data filtering algorithms and improved visualization software. FIU had earlier performed several years of research to deploy these profiling sonars in Hanford's 1 million gallon HLW tanks for the different technology need to optimize solids loading into double-shelled tanks. Much of the earlier research has relevance to the new, rapid scan application in much smaller HLW mixing tanks at Hanford. The key difference is the desire to image during the very short cycle times (15-30 seconds) of cycles in the PJMs. Extensive new testing was required for assessing imaging resolution under these very difficult conditions for sonar systems.

FIU's prior year effort on this task consisted of several successful demonstrations of the proof of concept for the application of its sonar in mixing tanks for short imaging periods (15-60 seconds). A milestone report was submitted to DOE EM in April 2014 that contained the research and technology testing results. FIU developed a 3-D sonar imaging software since the built-in commercial sonar imaging software does not function with sparse (few 2-D cross sections) sonar data sets such as those generated in scan times less than 1 minute. With proof of concept testing successful, FIU executed a Phase II Test Plan. FIU also continued to develop new data filters and to improve those developed in earlier years for the Solid-Liquid Interface Monitor (SLIM) sonar. Phase II testing included analyzing the image quality during short imaging times for various sonar settings. Results of this testing helped FIU identify the optimal settings for the sonar for this application. It also verified that the FIU SLIM sonar met some initial functional requirements for deployment for FIU's sonar into a high-level radioactive waste mixing tank. The functional requirements included data quality objectives for the accuracy and the allowable scan times.

In the current FIU year of effort (May 2014 – August 2015), FIU continued imaging objects, understanding how to optimize the sonar settings for various very short time sonar scans.

The Phase III testing of the sonar consists of sonar imaging of the tank floor while kaolin clay particles are incrementally added, varying the volume percentage of particles entrained in the water from 0% to 30% by volume. Phase III testing began in November 2014 with kaolin being added in January 2015. Very quickly, two major problems arose that halted testing and required solutions. First the pump power and the fluid flow in the test tank were not effective at suspending 3% entrained solids in the tank as evidenced by solids remaining on the floor of the tank. In addition, the image resolution of the sonar was greatly degraded during January 2015 testing. Movement of the sonar back to another test tank with no active mixing showed that the degradation was due to a physical malfunction on the sonar. The manufacturer later confirmed that the degradation was not due to the testing itself but due to the failure of a component in the sonar unrelated to the testing ongoing at the time.

In January – April, FIU began to perform tests and diagnostics on the 3-D sonar. Some of these tests were developed by FIU instrumentation engineers and the others were suggested by engineers at the manufacturer. Ultimately, it was determined that the sonar needed to be repaired and it was shipped out in April 2015, repaired and received back at FIU in June 2015. The engineer leading the testing for this task left FIU ARC in June 2015 and so a new engineer was brought on to support this testing. It was decided that it was important to repeat some earlier experiments with the repaired sonar as a way to re-baseline the image quality of the sonar to image objects and settled particles and thereby allow for more accurate comparisons of imaging results during mixing. This year also saw the design and installation of a new rotating nozzle system to better fully suspend large quantities of kaolin clay particles in the water during mixing.

Finally, FIU is working with WRPS and PNNL to identify a mixing or conditioning tank that would benefit from the deployment of the SLIM sonar technology.

INTRODUCTION

FIU has 3 custom-built profiling sonars (two 2-D and one 3-D) that were a component in the sequential prototypes of the Solid-Liquid Interface Monitor (SLIM) developed for Hanford. FIU continued testing its 3-D sonar this year to facilitate deployment into high-level radioactive waste (HLW) mixing tanks at Hanford tank farms and at the WTP. The HLW processing operations have a need to ensure that mixing by pulse-jet mixers (PJMs) is thorough and that solids are completely suspended and removed with each batch. Therefore, there was a new technology need identified for a system that can image or sense through the turbulent liquid and entrained solids during mixing and verify that no solids remained on the floor. Verification would allow operators to know that the waste was completely suspended and could be effectively transferred out of the tank for further processing.

In the 2003-2008 timeframe, FIU developed, tested and qualified full-scale SLIM for deployment in Hanford's 1 million gallon, HLW storage tanks (single-shell tanks (SSTs) and double-shelled tanks (DSTs)). FIU testing met all of the numerous performance requirements and the functional requirements for deploying into these tanks. Importantly, SLIM showed that it could image solids on the tank floor even while vigorous mixing entrained kaolin as much as 30% solids into the tank liquid. This is the reason for the Hanford Site interest in the SLIM sonar for this new HLW processing application. This new application for the SLIM sonar to image in mixing tanks involves much smaller tanks, more vigorous mixing, and a much shorter time allotted for imaging the settled solids layer on the tank floor. New software and new strategies have been developed to quickly and effectively visualize solids on the tank floor. FIU's SLIM consists of 3 primary components: (1) a commercial, customized sonar that is radiation hardened and impervious to highly caustic (pH>14) solutions; (2) a deployment platform able to deploy into DSTs and SSTs via 8-inch risers in the tank dome top; and (3) software for filtering sonar data and displaying an image of the solids settled across the entire floor of HLW tanks.

This task was initiated in October 2013. Progress made during the previous year (October 2013 to May 2014 is summarized in this Introduction section to provide a context for the current year's (May 2014 – August 2015) efforts and accomplishments. Current year progress is described in the Results section that follows. The focus of this task is to test FIU's sonar and its data filtering and image processing algorithms and software to facilitate deployment of the sonar at Hanford in 2016 or 2017.

Previous Year Accomplishments:

1. Developed bench-scale test plan to demonstrate proof of principle for rapid sonar imaging. Set up test bed and performed tests, varying the sonar settings to optimize the sonar image for rapid scans (15-60 seconds). Three key sonar settings include: total view angle, angle between sonar pings along a 2-D scan, and angle of rotation between each 2-D scan.
2. Developed and demonstrated the effectiveness of improved software to filter sonar data and to visualize tank floors, walls and solids on the floor.

Bench-Scale Testing: The testbed setup includes the 3-D sonar mounted inside of a tank with dimensions of 72 inches in height and 35.5 inches in diameter. A brick and other objects with specific shapes were selected for test objects to evaluate the accuracy of images with short time (15 – 60 seconds) scans by the sonar. FIU developed and applied filtering algorithms to remove points shown beyond the tank boundaries resulting from occasional sonar pings that have been scattered twice. Additional filtering algorithms smooth out the image contour of the walls and the settled solids layer surface. For later testing of the sonar during mixing, FIU developed an imaging algorithm that has an option to display the numerous sonar pings reflected off the entrained solids and back to the sonar or to eliminate all these reflections and only display the floor, wall and settled solids layer. The 3-D sonar operating software settings include: view angle (30°-180°); angle between successive sonar pings along every 2-D sonar scan (.9°-9.0°); and finally the angle between 2 successive 2-D scans can also be set at one of the same 10 options (0.9°-9.0°).

It was found that decreasing the swath angle can greatly reduce the time required to acquire a single sonar scan. Also, to reduce noise, the transmit pulse duration should be shortened to 10 microseconds.

The sonar software collects data into an ASCII file which can be imported into external mapping algorithms. The first algorithm was initially tested using the sonar image in the high resolution image to validate its accuracy. The algorithm was then used to generate maps of the low resolution sonar data. Figure 45 below shows 3 different views (off-axis, top and side) of the brick and tank bottom surface using FIU's 3-D mapping program. The images are the same, that is, the spatial dimensions for the location and size of the brick imaged is the same for the commercial sonar imaging as the mapper algorithm used to post-process the image of the object.

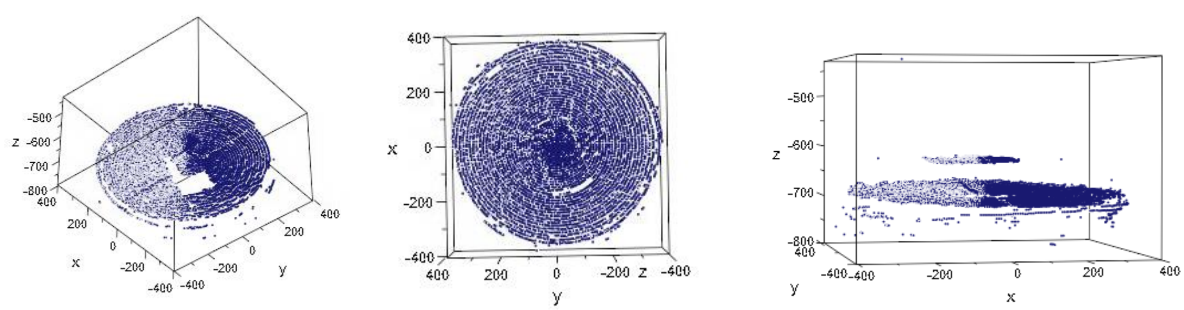

Figure 45. High resolution images from FIU's 3D mapper.

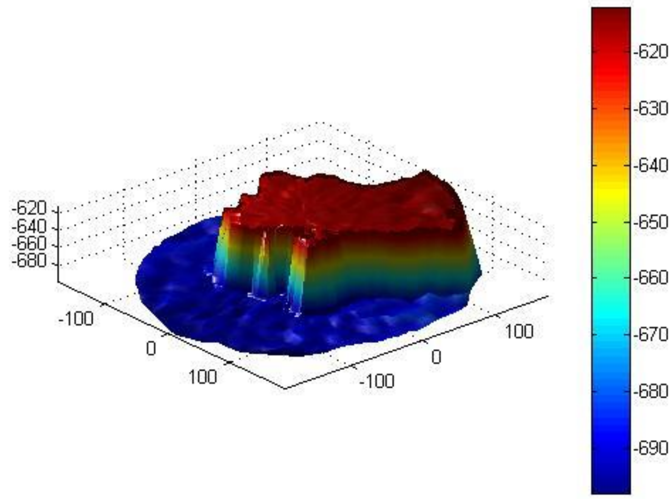

Figure 46. Trial #1 – Post-Processed – length, width and height of the brick is shown to be more accurate than volume estimation since interpolation distorts the location of the edge of the brick between 2-D swaths.

In Figure 46 above, one can observe that the height, width and length of objects can be imaged and measured quite accurately but that the interpolation between 2-D swaths contributes to errors in the boundary of a hard angle object which can result in errors in the volume estimate as large as 10%.

Baseline testing without mixing suspended solids was completed. Results of the testing will be discussed in the next section. Kaolin clay was then obtained to be used in the mixing studies. Additionally, software for automating the analysis and input of sonar data into imaging software was developed and needed refinement. In addition, specific data filters developed and/or tested include:

1. A minimum time filter to remove scatters sometimes seen around the sonar head;
2. A maximum time filter based upon tank dimensions and angle that will eliminate most double scattered sonar pings which show as points beyond a surface;
3. A nearest neighbor analyses that eliminates most sonar pings that scatter from particulates suspended in the water tank (important when mixing adds up to 30% by volume of solids to the water in the tank); and
4. Smoothing functions for interpolation of 2-D sonar slices into quality 3-D images even in sparse datasets (i.e., less than five 2-D sonar slices contributing to the sonar image due to short times available for imaging).

Depicted below in Figure 47 are images created by two additional processing filters for sonar data. The image is that of a standard brick. Filtering is needed to allow for automated analysis of the absence of the settled solids in the bottom of the mixing tanks at Hanford. Should there be settled solids during mixing, then the mixing operations engineer would either increase the energy of the PJMs or possibly allow more time for all solids to become mixed.

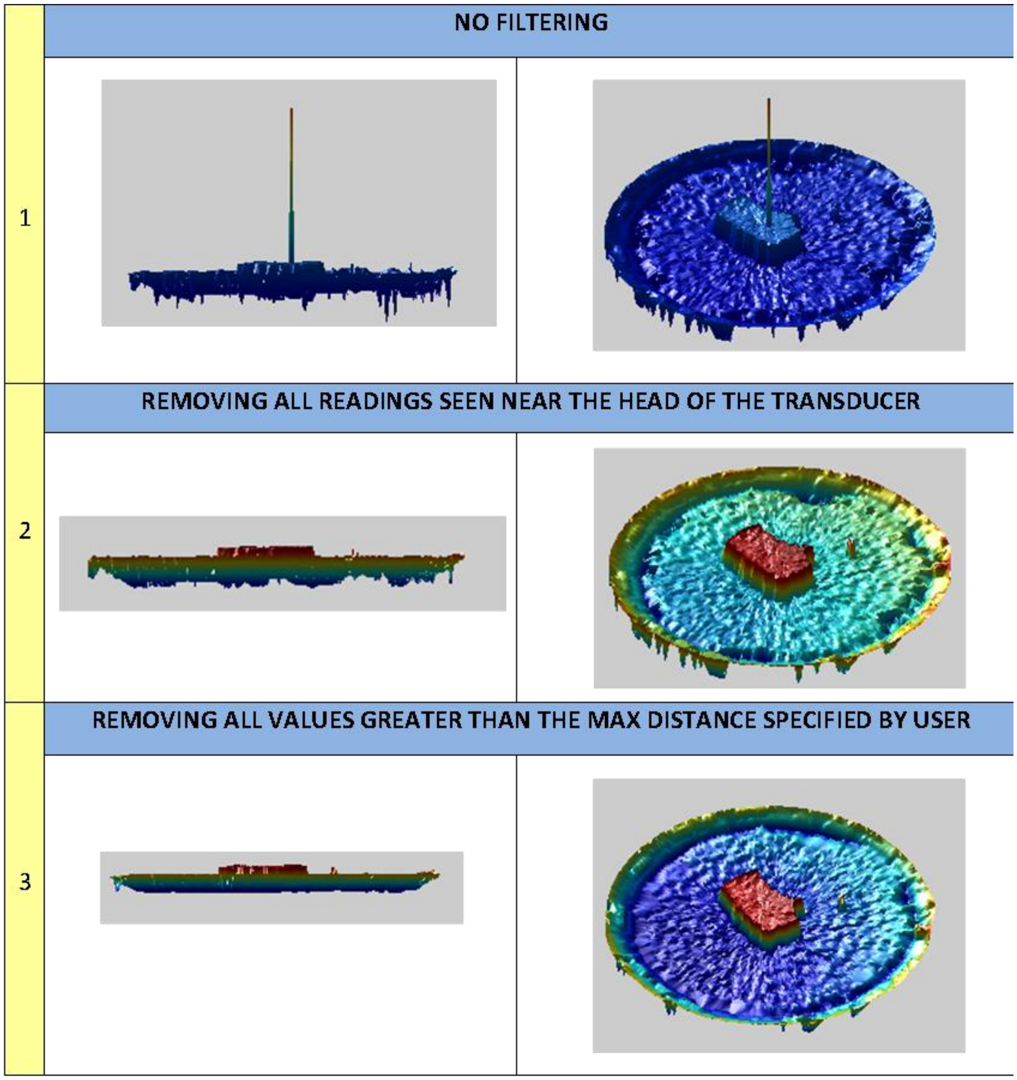

Figure 47. Results of a few sonar data filtering techniques.

Displayed below are the test results of filters 2 and 3 using the processing sonar data collected in March 2014. The image is of a standard brick sitting in the bottom of the laboratory test tank. Ultimately, filtering is needed to allow for automated analysis of the presence or absence of settled solids during the cycles of the pulsed jet mixers and the volume of the settled solids in the bottom of the mixing tanks.

The figures below were generated from data taken with the following experimental settings: 60° swath arc, rotation motor step size setting of 1, and swath motor step size of 1. Figure 48 shows FIU's 3-D sonar imaging software which displays unfiltered data. The two images in this figure are the side view and top view of the 3-D display of the sonar data without filtering.

In Figure 49, FIU's 3-D sonar imaging software displays the side and top views of the 3-D display of the sonar data with filtering that eliminates all data that is below the floor of the tank (due to sonar pings that scatter twice and still return to the sonar head). The initial algorithm currently corrects only the data that is below the tank floor (Z-axis) and could be expanded to eliminate data from beyond the tank walls. Sonar images during mixing with extensive scattering off suspended particles are expected to show significant double scatters beyond the tank walls. Red circles are used to show areas where filtering removed undesired (double scattered) sonar data compared to that shown in Figure 48.

Figure 50 displays the 3-D sonar data filtered to eliminate spikes that arise from scattering off suspended particles as well as possible noise in the system. This algorithm averages points based on the values of neighboring data. This mildly aggressive filtering algorithm will look at the Z-coordinate of each individual point and compare its neighboring points. If the difference in value between both neighboring points is greater than the specified user value, then the Z-coordinate will be replaced with the average of the two neighboring points. As seen by the red circles, the spikes observed within the original unfiltered data have been reduced. Observe the reduced height of the spikes in comparison with the original image. The spikes can be completely eliminated with a different scale applied to the nearest neighbors filtering. Finally, Figure 51 displays the sonar data filtered using both of the filters described above (double scatters and reflections off suspended particles).

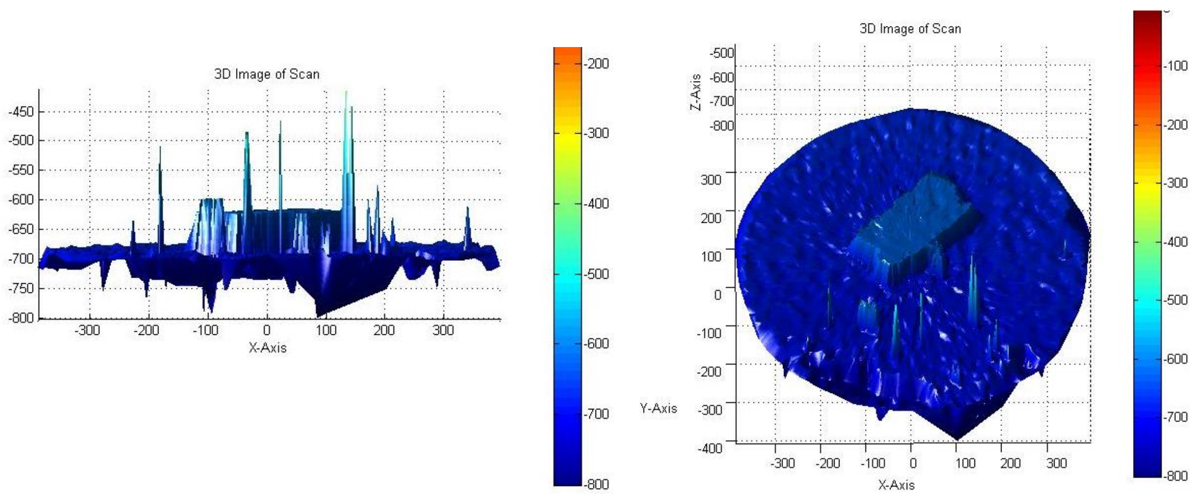

Figure 48. 3-D sonar side view and top view displays for unfiltered data.

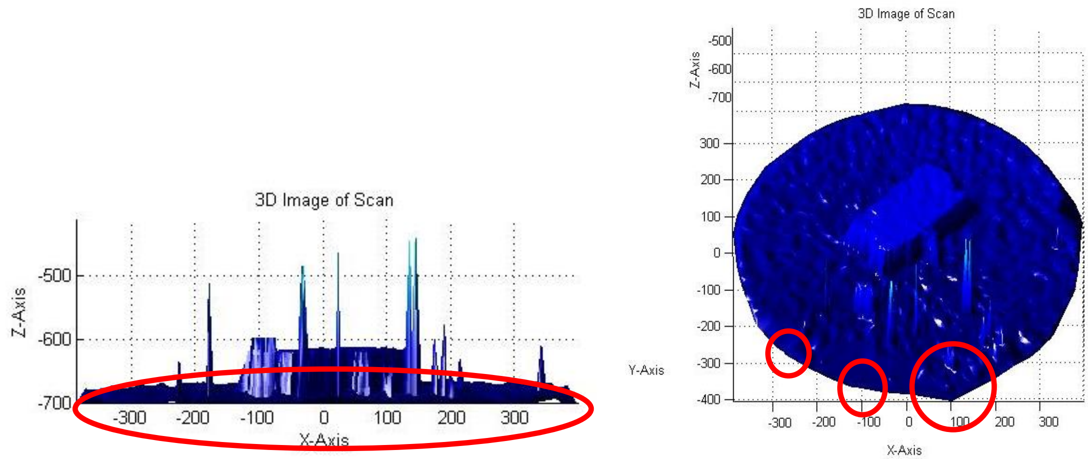

Figure 49. 3-D sonar side view and top view displays – filtered to remove data below floor.

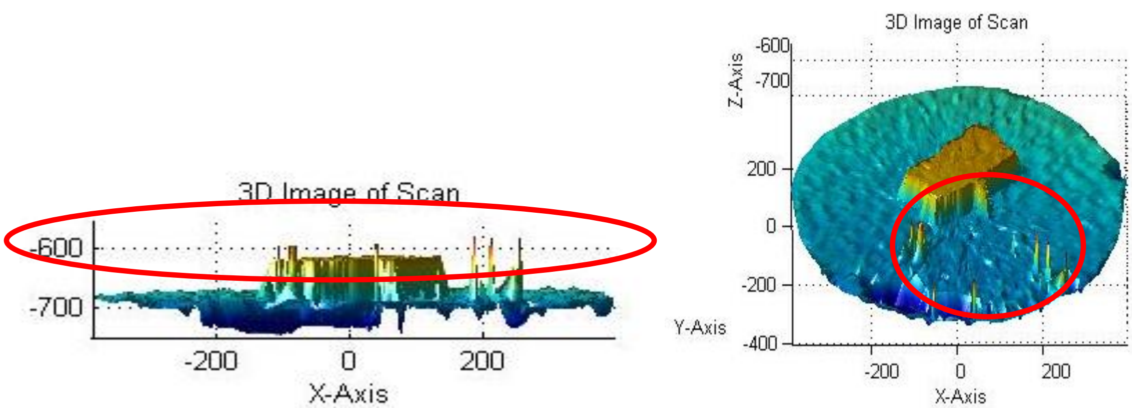

Figure 50. 3-D sonar side view and top view displays – filtered to reduce spike size.

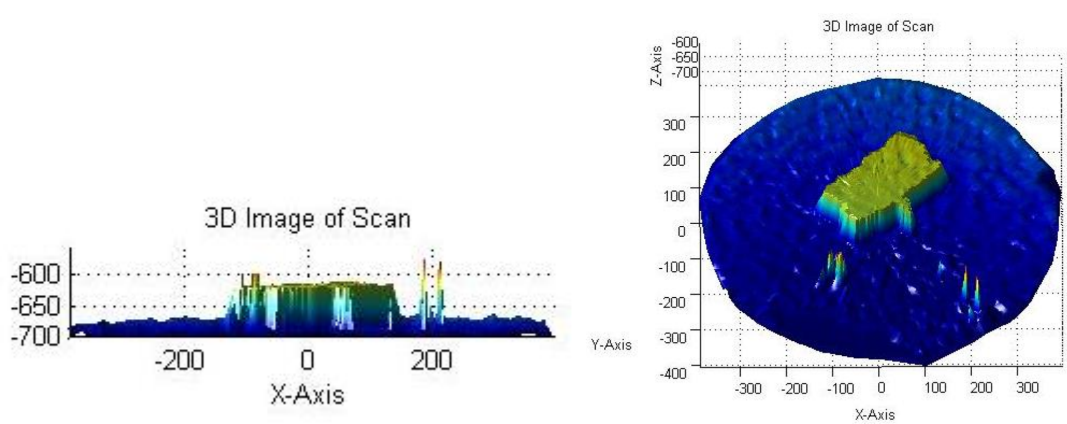

Figure 51. A 3-D sonar side view and top view displays with filter to remove data below floor and filter to reduce spike size.

RESULTS

At the end of FY14 (April 2014), a pilot-scale test plan for SLIM was completed and sent to the Hanford Site and to DOE EM Headquarters. A goal for this test plan is to demonstrate that the SLIM sonar will meet initial functional requirements for a technology deployment in a high-level radioactive waste mixing tank. Future functional requirements will include data quality objectives for the accuracy and allowable sonar scan times. As FIU continues to test its sonar against performance requirements for deployment at the Hanford tank farms and at the WTP, additional tests have been suggested to improve the likelihood of deployment or to address engineering safety issues or other concerns in the deployment and operation of the system.

Sonar Data Validation, Verification and Completeness

The commercial sonar component of FIU's SLIM provides 3-D sonar images by interpolating between data from multiple 2-D slices. Described below is the process of post-processing the sonar data to ensure data is valid and to verify its completeness. This data is then input into an algorithm to measure the volume of all material and objects imaged above a floor area (e.g., the volume of solids on a tank floor area).

Algorithm to Separate 3-D Sonar Data from Sonar ASCII Text File

The sonar data for each 2-D scan (or slice) is stored in a long list of XYZ points using a comma as a delimiter. An example of the format can be seen in Table 8 below. This table displays the initial set of points for one of the initial experimental tests (or trials) that was conducted on SLIM. This test was recorded as Trial 2 and was successfully completed in approximately 24 seconds with the highest possible setting of swath motor step size (setting 1) and a moderately low rotate motor step size setting (setting 7).

Table 9 shows the results of the 6 trials conducted in the past along with each of the associated settings. For this description of data preparation and processing, the data from "Trial 2" (outlined in red) was used for portioning and analysis.

Table 8. Example of Output ASCII Data from Sonar (in mm)

000000,000168,000614 000000,000158,000616 000000,000147,000614 000000,000137,000613 000000,000127,000615 000000,000118,000617 000000,000108,000617 000000,000098,000616 000000,000088,000617 000000,000078,000617 000000,000068,000617 000000,000058,000617 000000,000049,000617 000000,000039,000618 000000,000029,000617 000000,000019,000618…………etc

Table 9. Time Trials Results

Trial	Time	Swath Motor Step	Rotate Motor Step	Swath Arc
1	~45 Seconds	1	3	30
2	~24 Seconds	1	7	30
3	~19 Seconds	1	10	30
4	~32 Seconds	3	3	30
5	~19 Seconds	3	7	30
6	~15 Seconds	3	10	30

The data is retrieved from the sonar output text file with an extension ".txt" (see Figure 52 left). This text file is then uploaded into MATLAB using a delimiter function in order to separate the data into its X, Y, and Z partitions. The sonar provides an extensive list of data without any separation identifying where each individual swath began or ended. MATLAB is used to further partition the data into the individual 2-D swaths. Using Trial 2 as an example, 29 individual swaths (see Figure 52 middle) were identified and registered. There are 34 pings per 2-D swath, each with points denoted by x, y and z coordinates (see Figure 52 right). The algorithm scans the 3-D coordinate data and identifies when a new swath is recorded when a value along the X coordinate column is far greater than the previous value.

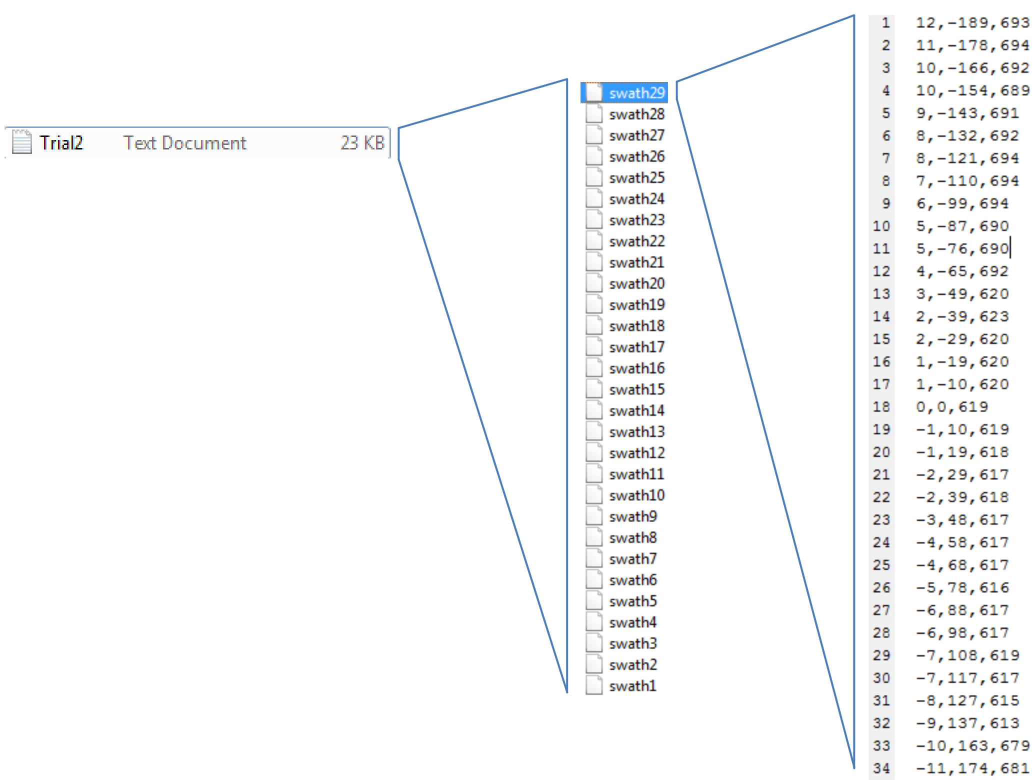

Figure 52. Document with selected time trial (left); derivation of 29 swaths from selected trial (middle); and the correct separation of sonar data into individual 2-D swaths.

Next, an additional software algorithm code was developed to allow for a "Limited Area View" of imaged sections of each scan. The limited area view reduces the area viewed during each scan and therefore limits extra post processing of data that is outside the area of interest. In the proposed application of FIU's SLIM in Hanford's mixing tanks, the area of interest is the area between pulsed jet mixers and constitutes only a few square feet of the tank floor. This algorithm will improve the volume calculation of each scan by eliminating the processing of data from areas where no solids are expected but errors in the measurement of the bare floor would add increased error to the total volume calculated for solids on the tank floor. False height measurements above the tank floor can arise from sonar ping reflections off the tank wall or off solid particles suspended in the liquid or from any double scattering of sonar the sonar pings that has a return path to the sonar. Based on the broader algorithm used to interpolate each ping detected by SLIM, this new algorithm will increase the quality and accuracy of the interpolation by removing erroneous spikes due to the mechanisms described above for sonar pings that can result in false height calculations.

<u>Examples of How the Limited Area View Algorithm Works</u>
This algorithm removes sonar data points from the beginning and end of each swath that are outside the area of interest, focusing directly below the sonar since the sonar may be positioned directly over the small area of interest where solids might accumulate.

In the example below, a 60° swath arc scan with 34 pings was used. This scan was one where the brick was centered directly under the sonar. The algorithm removes data that is outside the small area of interest. Simultaneously, the algorithm filters the sonar data to correct values that are out of range and that would cause errors in the interpolation algorithm. Figure 53 is an image where all of the past filtering algorithms have been applied. Yet, the calculated solids volume in the area surrounding the brick is undesirable and reduces the accuracy of the volume due to errors in the sonar data that show as reflections high above the floor (or as spikes).

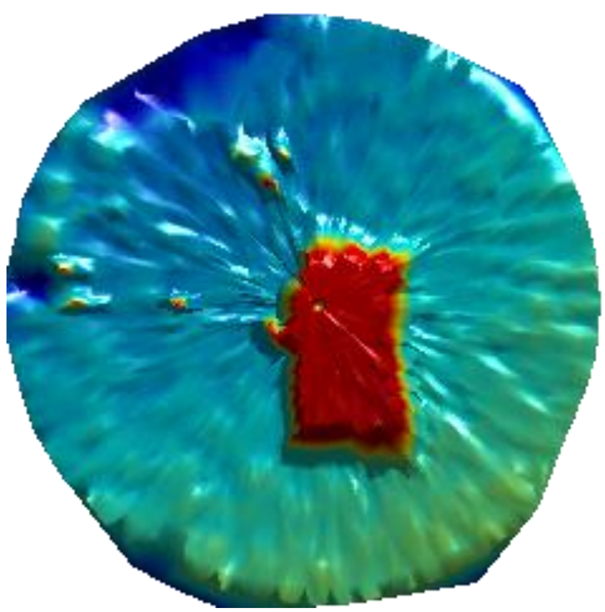

Figure 53. Sonar image processed with all data points.

As extraneous sonar data points are removed, the image is focused on the smaller area of interest as shown in Figure 54. In this image, note the immediate change in height of solids as depicted by the changed default color scale. The area around the brick in now a dark shade of blue depicting a distance of 680+ millimeters away from the SLIM sonar in comparison with the image in Figure 53 which had 660-675 millimeters from the sonar.

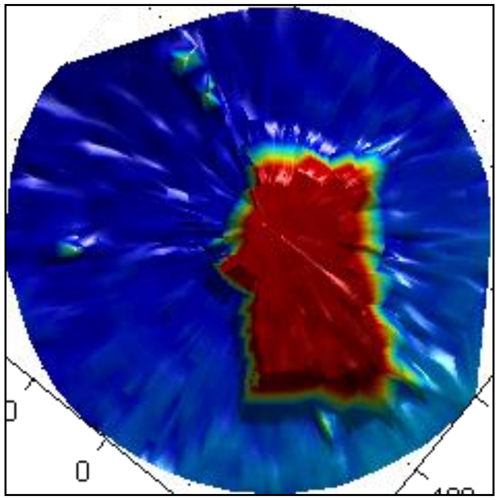

Figure 54. Limited area view on the area of interest after 4 data points removed per swath.

Figure 55 shows an image where sufficient sonar data points have been removed to start to lose the data from the brick or the area of interest. Processing of the sonar data can be optimized to allow imaging of only the area of interest as shown in Figure 56.

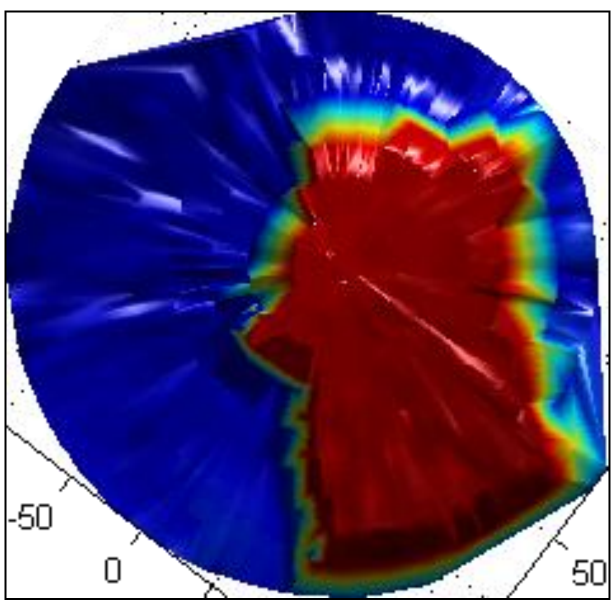

Figure 55. Sonar image with 8 data points per swath removed with part of brick cutoff.

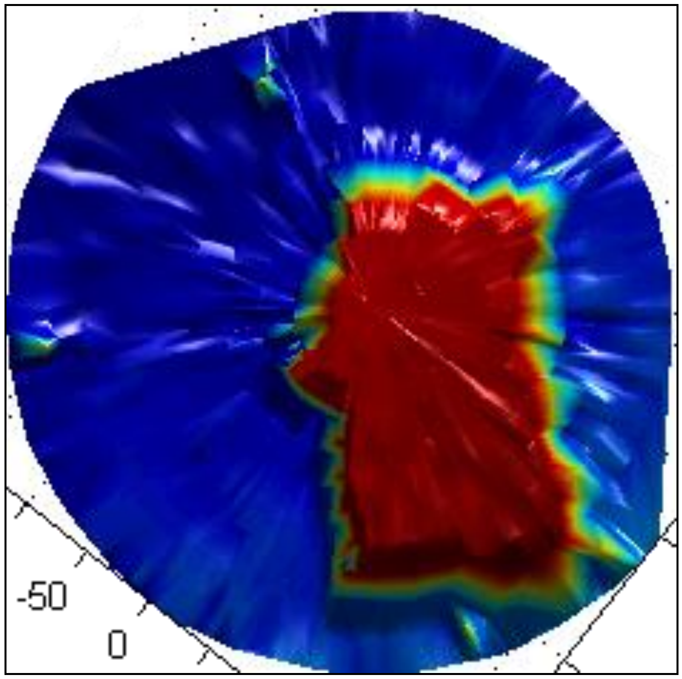

Figure 56. Optimal image with 6 sonar data points removed per swath.

Kaolin Properties Summary

The settling time for kaolinite is dependent on the solid concentration (% kaolinite within the fluid), the ionic strength of the kaolin and the pH of the water. Research shows that as the concentration of kaolin in an aqueous solution of water increases, the settling time will increase as well, almost at a linear rate, assuming the pH of the aqueous solution is 7. The Hanford and Savannah River Site high-level radioactive waste (HLW) are highly alkaline (pH >14). In alkaline solutions, kaolin settles as dispersed particles when ionic strength is low. When ionic strength is increased in alkaline solutions, kaolinite particles settle in flocculated form. Results also show that as the solid concentration increases, the settling rate decreases due to the buoyancy effect.

Kaolin Settling and Flow Characteristics Testing

Testing of the pulverized kaolin clay material purchased from Edgar Minerals was conducted to help measure the settling rate and thereby understand flow characteristics of these micron-sized particles in water. Data collected and analyzed enabled the simulation of flow of this specific form of kaolin in water within our test tank (dimensions of 36 inches in diameter and 84 inches in height). Another goal of this experiment was to help FIU determine the type of pump and nozzle as well as their setup in the tank to ensure complete mixing and a uniform density of entrained kaolin particles during various experimental tests.

A 2-liter beaker was used for our testing and scale-up calculations. With a proportional volume of water and volume of kaolin, the settling time and behavior for the kaolin were studied. This experimental test plan included measurements from 0% to 30% (by volume) of kaolin in water-kaolin slurry. The kaolin purchased, CAS no. 1332-58-7, has a density of 2.6 g/cm^3.

Results from the experiment showed the expected linear correlation between the concentration of kaolin in water (or volume %) and the settling time of the kaolin. When ionic concentration is low (pH~7), the particles will be seen in a dispersed form and thus settle in accordance with Stokes' sedimentation law.

Experimental Setup and Final Planning for Sonar Tests with Suspended Kaolin Particles

A polyethylene tank was set up in the FIU ARC research facilities and the sonar and a mixing pump were installed in the tank. HLW particulate simulant (1 micron diameter kaolin particles) were ordered and used for testing of imaging capability while mixing solid-liquid slurries.

A pump, nozzle and mixing system was designed, acquired and installed in the test tank to mimic Hanford mixing tank operations. The installed pump system consists of a 2 horsepower centrifugal pump, 2 hoses and a 3-way split head nozzle. The pump has been placed outside of the tank and the output hose connects the pump to the 3-way split head nozzle. The input of the pump is connected to an intake on the opposite side of the tank but at the same level. The pump system has been tested and the desired dynamic fluid movement has been achieved. The photograph below in Figure 57 shows the 3-way nozzle (water inlet) and opposite the tank outlet leading to the pump intake.

Figure 57. Three-way nozzle inlet and tank outlet directly opposite, both near the bottom of the test tank.

In October 2014, FIU completed the experimental setup and experimental plan. The goal of this test plan is to measure the sonar's ability to visualize and measure the volume of solids on the floor of the mixing tank while kaolin particle solids and water are completely mixed in the tank. There is a critical % solids entrained in the water during mixing which will completely obscure the sonar imaging of the tank floor and settled solids on the floor. FIU will determine that % solids for a sonar positioned 1, 2 and 3 feet above the tank floor. Sonar measurements will be taken during mixing as well as 0, 30, 45, and 60 seconds after the mixing pump is turned off. Hanford engineers have requested tests to image immediately after the pump mixer is stopped and while the micron-sized kaolin particles settle to the floor.

A structure with unistrut components has been designed and assembled across the top of the tank to hold the sonar in place and perpendicular to the tank floor even during mixing operations. The unistrut design holds the SLIM sonar within 3 degrees of the perpendicular in order to reduce errors due to an offset angle. Extra effort was focused on the forces and possible deflections of the sonar during the vigorous mixing motion of the water and entrained kaolin inside the tank. The unistrut design has been reinforced across the tank top to ensure that the sonar remains rigid with respect to its orientation to the tank.

Experimental testing of the SLIM sonar's ability to image through HLW with suspended particles (mixing) was performed for 3 months. Initial tests in the tank without kaolin were completed prior to adding 1% and 3% by volume kaolin.

A section of unistrut was used as the imaged object during these initial experiments. The weight of the steel unistrut kept it from moving during vigorous in-tank mixing. Also, the unistrut was placed on the tank floor directly in the line of flow of the nozzle to the tank outlet to the pump so that no solids material would accumulate around it as happened around the solid brick used in earlier testing. The test tank is 1 meter in diameter and the sonar was positioned exactly 1 meter above the tank floor for initial tests. See Figure 58 below a photograph of the section of U channel used as the imaged object.

Figure 58. Object to be imaged (a section of unistrut or U-channel).

The first sonar scan shown in Figure 59 is of the empty tank and the object being imaged is the nozzle directed into the tank. The second and third sonar images show results of imaging for 30 seconds with no kaolin added (0% vol. kaolin) and for imaging 30 seconds with 1% vol. kaolin. Note the sonar images of the nozzle and unistrut on the tank floor are identical in these last two sonar images. These images were created with software developed by FIU that includes MATLAB modules. The object on the left side of sonar scans 2 and 3 is the plastic coupling for the tank outlet that leads to the hose and pump inlet. Note that there is no effect on the image quality from the entrained kaolin particles.

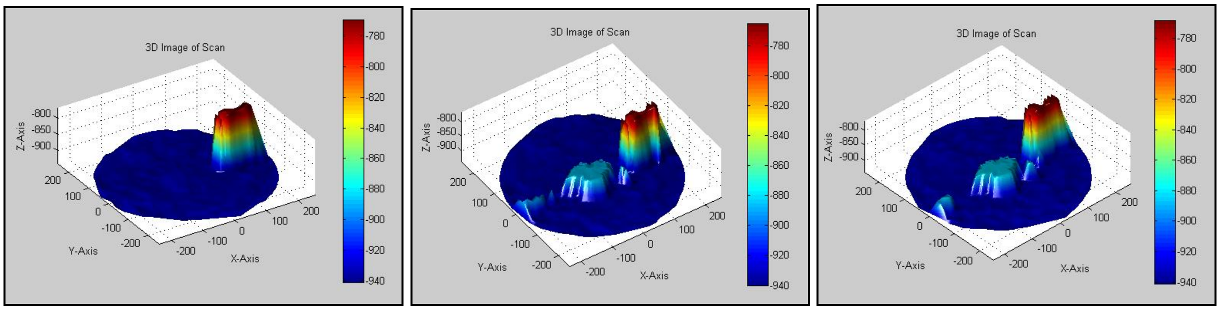

Figure 59. Sonar Scan 1 (left): empty tank with nozzle protruding from the right; Sonar Scan 2 (middle): same tank with a section of U channel (unistrut) aligned linearly with the nozzle; Sonar Scan 3 (right): tank with U channel as well as 1% kaolin added.

FIU initiated these experimental tests in December 2014 to test the ability of the 3-D sonar to image solids on the tank floor while solids are beings mixed (suspended) in a tank. Kaolin clay is used as the HLW solids since it has a diameter of approximately 1 micron similar to Hanford HLW. For this reason it has been found to be an excellent surrogate for the rheology and settling of solids in Hanford high-level radioactive waste tanks. The calculation for the mass of kaolin clay needed to be added to our tank water to vary the volume % of kaolin from 1% to 20% is shown in Table 10.

Table 10. Mass of Kaolin for 1-20 Volume Percent of Kaolin in FIU's Test Tank

Volume Percentages	% Volume (meters cubed)	Mass of Kaolin Required (kg)	Mass of Kaolin (lbs.)
1%	0.006207	16.1382	35.57859848
2%	0.012414	32.2764	71.15719697
3%	0.018621	48.4146	106.7357955
4%	0.024828	64.5528	142.3143939
5%	0.031035	80.691	177.8929924
6%	0.037242	96.8292	213.4715909
7%	0.043449	112.9674	249.0501894
8%	0.049656	129.1056	284.6287879
9%	0.055863	145.2438	320.2073864
10%	0.06207	161.382	355.7859848
11%	0.068277	177.5202	391.3645833
12%	0.074484	193.6584	426.9431818
13%	0.080691	209.7966	462.5217803
14%	0.086898	225.9348	498.1003788
15%	0.093105	242.073	533.6789773
16%	0.099312	258.2112	569.2575757
17%	0.105519	274.3494	604.8361742
18%	0.111726	290.4876	640.4147727
19%	0.117933	306.6258	675.9933712
20%	0.12414	322.764	711.5719697

These masses and volume percentages were calculated for the right cylinder tank with the following parameters:

H, Height of water in the tank	H = 1 meter
ID, Inner diameter of the tank	ID = 0.889 meters
R, Radius of the tank	R = 0.4445 meters
V_f, Volume of a right cylinder of fluid	$V_f = \pi \times R^2 \times H$
ρ, density of Kaolin (intrinsic)	$\rho = 2600\ kg/m^3$

In December, testing was completed for 0%, 1% and 3% volume of Kaolin. Data was collected for both 30° and 60° swath arcs with scans taking 29 seconds and 42 seconds, respectively. The unfiltered images for both the 30 and 60° arc scans are shown in Figures 60 through 62 for 3% Kaolin by volume.

The sonar image in Figure 60 is for the 30° swath arc. It is a scan that focuses upon the center of the tank. The dark blue shows the tank floor, the light blue is the top of the piece of unistrut and the orange/red/yellow layer is the kaolin that was not lifted by the mixing in the tank from the nozzle. It is important to note that the pump inlet and outlet were on opposite sides of the tank at the bottom and the direct fluid flow was in direct alignment with the unistrut and this is why there is no settled Kaolin in this blue flow field.

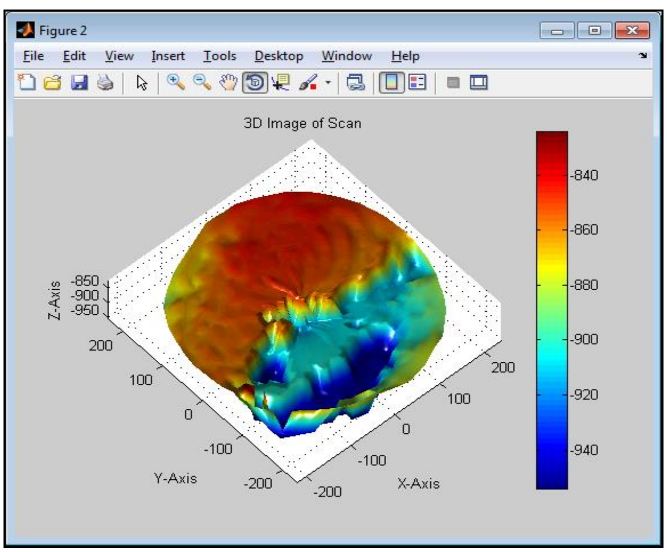

Figure 60. 3-D sonar scan for: 30° swath arc; 29 seconds; and 3% vol. Kaolin.

The sonar image in Figure 61 is of the entire bottom of the tank with the 60° swath arc. While the color scale has changed, one can see the above sonar scan between -200 and the 200 range along the X-axis and the -200 and the 250 range along the Y-axis. This image contains no filters. The peaks around the outer circumference of the tank are the tank walls as well as the inlet and outlet pipe fittings for the fluid being pumped.

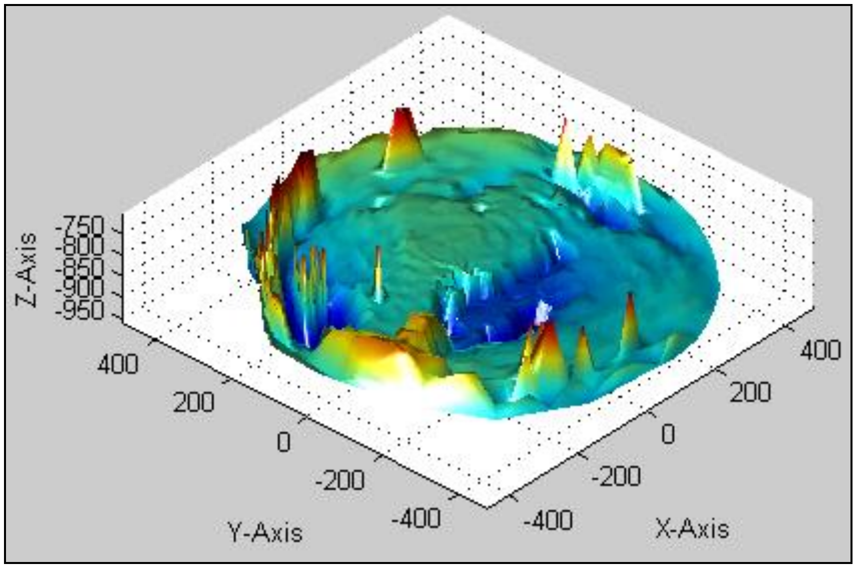

Figure 61. 3-D sonar scan for: 60° swath arc; 42 seconds; and 3% vol. Kaolin.

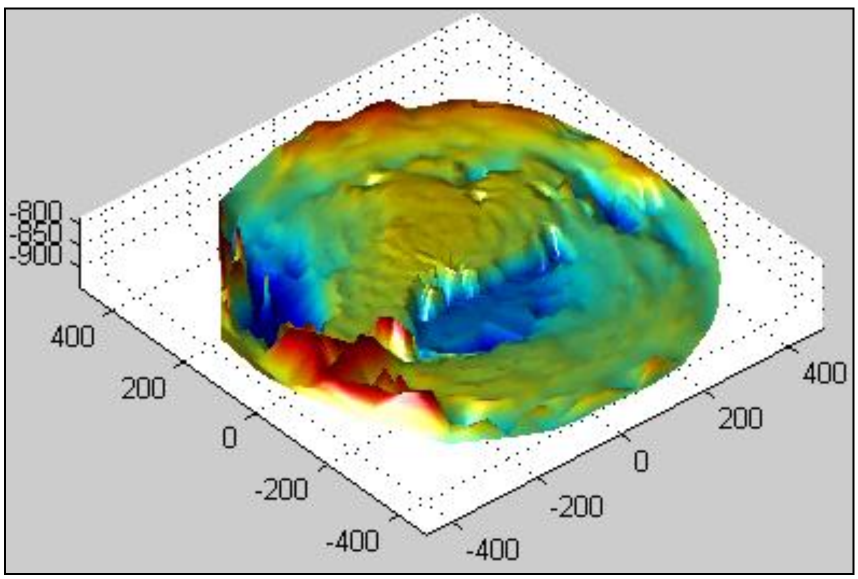

Figure 62. A 3-D sonar scan for: 60° swath arc; 42 seconds; and 3% vol. Kaolin with a simple filter applied to data to remove wall and pipe fittings.

A simple data filter was applied to remove the spikes seen arising from the walls and pipe fittings (tank inlet and outlet fittings) as shown in Figure 62. The direct flow of fluid across the bottom of the tank sweeps away all Kaolin but immediately outside of the direct flow path, Kaolin is settled on the floor.

The pump and the flow design for the experimental setup was modified in January through April to assure that solids at 1-20% vol. of Kaolin will remain suspended and not allowed to settle and remain on the floor. Calculations and empirical tests were used to confirm that the pump flow field is over designed for the mixing and suspension.

In earlier SLIM tests at FIU from before 2010, the ability of FIU sonars to image solids on the tank floor while solids were beings mixed (suspended) in a tank was successfully demonstrated for up to 30% Kaolin by volume. These earlier tests did not have time restrictions and took several minutes to generate accurate 3-D images.

In January 2015 testing was completed for 0%, 1% and 3% volume of Kaolin. Data was collected for both 30° and 60° swath arcs with scans taking 29 seconds and 42 seconds, respectively. There were two primary results of this testing: (1) the pump used is insufficient in power to keep all Kaolin suspended at 3%; and (2) the sonar experienced a major decrease in image quality with a major increase in "transmit breakthrough." It is normal for the sonar to have a small amount of transmit breakthrough near to the sonar head caused by the transmit pulse bouncing around in the sonar dome due to the impedance mismatch between the transducer/oil/PEEK/water interfaces.

FIU located a bigger pump and reconfigured the nozzles to better suspend up to 1000 pounds (maximum) of Kaolin clay particles in the tank. FIU worked with the sonar manufacturer, Marine Electronics, from the United Kingdom, for two months to discover why there was a sudden, permanent increase in the level of the breakthrough for the sonar. Some of the initial troubleshooting included: 1) testing the electrical current within the electrical processing units in order to determine if the device is receiving accurate signals, and 2) testing of the electrical pins on the umbilical cord connecting the electrical processing unit to the remote commercial sonar head. FIU completed these diagnostic tests on the sonar; the result of diagnostic tests was that the sonar needed repairing and FIU shipped the system to the manufacturer.

Due to the need for a larger mixing pump in the test set up, all sonar imaging tests during mixing will be redone with the new setup.

FIU performed an initial study to analyze how powerful (horsepower) a pump was required to suspend up to 1000 pounds of kaolin clay in the upcoming experiments. FIU has a 1 HP and a 1.5 HP pump and the 1.5 HP pump was selected for installation into the test tank. The shape and the orientation of the nozzles in the test tank were studied for improved mixing.

During the limited scan times for this new technology need, the sonar is able to generate few 2-D scans (swaths). In addition, there may be a requirement to image solids settled on the tank floor from an oblique view and not directly over the solids. If the sonar were to be inserted into these tanks inside the ring of pulsed jet mixers and required to view the settled solids through limited views between adjacent PJMs, then the advantage of the 3-D sonar compared to the 2-D sonars is decreased or eliminated. It would be prudent to test both systems for their capabilities for this challenging technology need. FIU has two 2-D sonars that were also built for deployment in a high-level radioactive waste environment. These sonars were custom built by Imaginex Inc. and have not been used at FIU for 5 years while FIU focused on the 3-D sonar alone.

FIU obtained improved sonar imaging software from Imaginex and have begun to learn this different sonar graphic user interface (GUI) and imaging software. Past mixing tests with the 2D sonar always required several minutes for excellent images. These short scans will be the first such tests of the 2D sonar for rapid scanning. If successful, then results from the 2D sonar for the current test tank and test matrix can be compared to that of the 3D sonar.

FIU's 3-D sonar was repaired by Marine Electronics and received back at FIU. Water will be injected into the bottom of the tank via the rotating nozzles. A new mixing configuration was designed and parts were ordered, received and installed. The experimental setup included a structure of U-channels framed around the tank to allow for the sonar and the pumping and mixer system to be bolted to it. A photograph of the tank and structure is shown in Figure 63.

Additional tests were developed for the 2-D and 3-D sonar due to the new experimental test setup and in order to get additional data points on the cutoff density of kaolin clay. Kaolin clay will be added in increments until the tank floor cannot be imaged at a distance from the sonar of 4 ft due to scattering from suspended particles. At this point, the sonar will be lowered to 3 ft from the tank floor and additional Kaolin will be added until again the sonar signal is attenuated and the floor cannot be imaged. Tests will be completed for 4, 3, 2 and then 1 foot distances. Grab samples of the suspended Kaolin will be collected to measure percent solids by volume and compared to that calculated based upon water and Kaolin input into the tank.

Figure 63. New structure around the test tank for mounting sonar and rotating mixer.

In addition, several tests completed on the 3-D sonar will be performed on the 2-D sonar scans (e.g., 20-30 seconds) to allow comparison of their performance. Past mixing tests with the 2-D sonar always used several 2-D scans which required several minutes for excellent images. These short scans will be the first such tests on this 2-D sonar. If successful, then results from the 2-D sonar for the current test tank and test matrix can be compared to that of the 3D sonar. Figure 64 shows photographs of the hollow rotating shaft with 2 nozzles attached.

Figure 64. A rotating shaft with opposing nozzles for mixing solids in the test tank (left); the rotating bearing close up (right).

Deployment of SLIM

Engineers at PNNL reached out to FIU to request information on the SLIM sonar, current tasks and capabilities of the sonar system as documented with many tests over the years. FIU sent annual reports, technical reports, and presentations and papers on the SLIM system. There is an interest in the results of the current testing on the sonars. The PNNL engineers have identified sonar testing they would like to see implemented at FIU, related to possible future testing of the sonar at PNNL for application to mixing tanks at WTP.

If the FIU sonars meet PNNL performance requirements, then there would be interest in testing the sonar at PNNL on their tank and mixer setup in order to ascertain that the pulse jet mixers will indeed mix and suspend all solids in all HLW slurries to be received at WTP (i.e., testing of the entire envelope properties of HLW (waste acceptance criteria) for WTP in the future). Ultimately, the goal is to test the envelope of HLW conditions in a test tank at PNNL and ensure that the solids are always mixed. Understanding the operating conditions of the mixers for the entire envelope of waste conditions would mean that the sonar would have completed its mission and demonstrated how PJMs would need to operate to ensure complete mixing in the tanks. If PJMs are operated where they would completely mix any type of waste that would be accepted to WTP, then they would not be needed in the actual HLW mixing tanks inside WTP.

CONCLUSIONS AND FUTURE WORK

This past year, FIU successfully completed functional testing of the 3-D profiling sonar from SLIM to assess its imaging quality with short time periods (15 – 60 seconds). After multiple successful tests of the sonar, the testing while mixing 0% to 30% by volume kaolin clay particles failed in January 2015 for two reasons: inadequate mixing and the sonar hardware underwent a permanent change that greatly degraded the image resolution and “breakthrough.” FIU also redesigned the tank mixing system by implementing a rotating dual nozzle system in the test tank. FIU then completed tests to image objects from 3 mm to 6 mm in thickness. A hard object 6 mm thick was easily observed as it was moved around the tank floor while other hard objects 3 mm in thickness were not distinguishable in the sonar scans. FIU submitted a package to PNNL for possible deployment of the sonar in their test tank related to WTP and was successfully selected during the first round of screening for technologies. Since the engineer that had performed most of the sonar imaging over the past year left ARC in April, a new engineer has begun operating the 3-D sonar and becoming aware of the filtering algorithms and the FIU visualization program. To date, the sonar still looks promising for deployment in mixing tanks in Hanford tank farms and in mixing tanks related to validation of full mixing in WTP mixing tanks.

In the next year, the test plan for imaging while increasing amounts of kaolin clay are added will be executed. There will also be more interaction with PNNL, Energy Solutions, and Bechtel for the WTP and performance and functional requirements for an imaging system to be deployed into the PNNL full-scale test mixing tank. Also, since the angle of view for a sonar deployed into a HLW mixing tank is likely be oblique and because the short scan times allow for few 2-D swaths to be collected, the advantage of the 3-D sonar has been diminished or eliminated. Testing of the 2-D sonar offers the opportunity for possible improved imaging, such as viewing the settled solids layer on the floor through great distances between the sonar and the floor while HLW mixing is occurring.

TASK 18.2
DEVELOPMENT OF INSPECTION TOOLS FOR DST PRIMARY TANKS (FIU YEAR 5)

EXECUTIVE SUMMARY

In August of 2012, traces of waste were found in the annulus of the AY-102 double-shell tank storing radioactive waste at the Hanford DOE site, prompting the need for developing inspection tools that can identify the cause and location of the leak. To help in this effort, Florida International University (FIU) is investigating the development of inspection tools able to access the tank's secondary containment, while providing live visual feedback. This effort has led to the development of two inspection tools: a magnetic wheeled miniature motorized rover that will travel through the refractory cooling channels under the primary tank, and a pneumatic pipe crawler that will inspect the tank ventilation header piping. Both inspection routes lead to the central plenum under the primary tank.

The magnetic wheeled miniature tool is a remote controlled rover with four wheels directly driven by independent micro DC motors. The tool is being designed for highly radioactive environments, and does not house any embedded electronics other than the camera. The inspection path consists of approximately 38 feet of channels, as small as 1.5 inches by 1.5 inches, and it includes several 90° turns. To avoid debris, the device will travel upside down magnetically attached to the bottom of the primary tank.

The pneumatic pipe crawler is a snake type robot with a modular design, composed of interchangeable cylindrical modules connected with flexible links. The design is an evolution of previous peristaltic crawlers developed at FIU, and uses pneumatic actuators to emulate the contractions of the peristaltic movements, which is suitable for highly radioactive environments by not requiring embedded electronics. The inspection path consists of approximately 100 feet of piping from grade, down through one of the drop legs and then lateral to the center bottom of the tank secondary containment. The route consists of pipes with 3 and 4 inches in diameter, reducers and several elbows.

Initial prototypes for the inspection tools have been designed and tested at FIU; further design modifications are currently being tested. Various tests have been conducted, ranging from isolated maximum force tests to lab scale mock up tests. FIU's staff is in routine communication with the site engineers, providing a valuable resource for necessary modifications.

INTRODUCTION

In August of 2012, traces of waste were found in the annulus of the AY-102 double-shell tank storing radioactive waste at the Hanford DOE site, prompting the need for developing inspection tools that can identify the cause and location of the leak.

Figure 65 shows three possible entry points for inspection in the AY-102 double-shell tank:

1. the refractory air slots through the annulus,
2. the leak detection piping, and
3. the ventilation header piping.

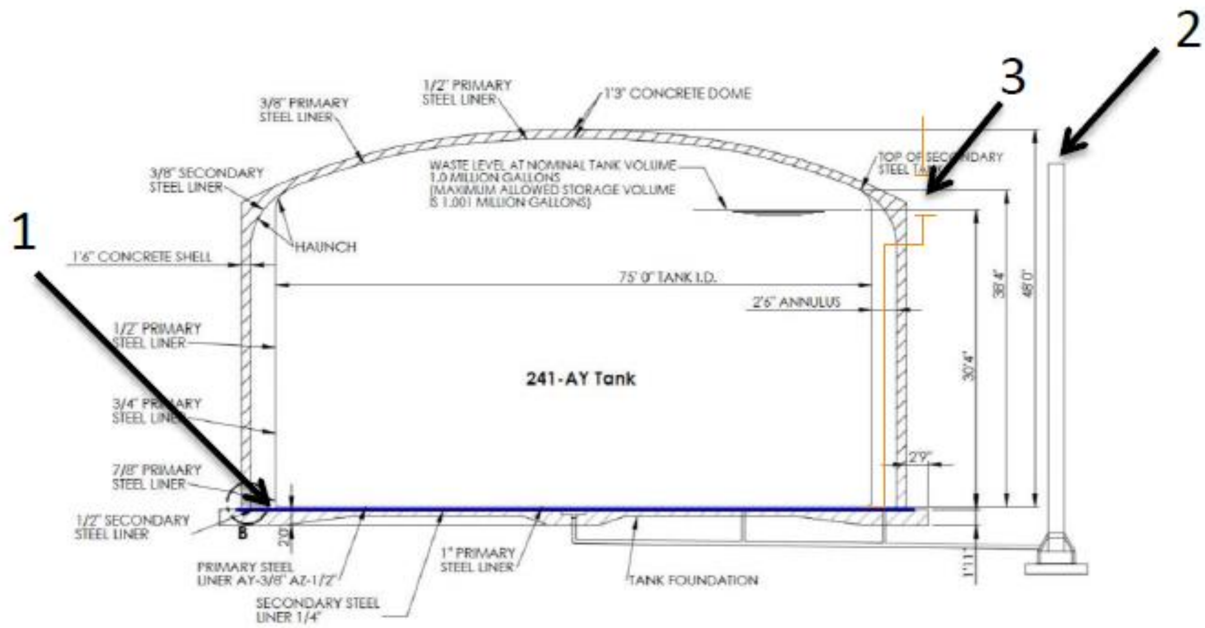

Figure 65. Inspection entry points of the AY-102 double-shell tank.

To assist in this effort, Florida International University is investigating the development of inspection tools able to access into the tank secondary containment, while providing live visual feedback. The effort led to the development of two inspection tools:

- a ***magnetic miniature rover*** that will travel through the refractory air slots, and
- a ***pneumatic pipe crawler*** that will inspect the ventilation header piping.

The objective of this task is to develop inspection tools that will assist site engineers at Hanford in isolating and pinpointing the source of the material entering Tank AY-102 annulus space..

MAGNETIC MINIATURE ROVER

Background

FIU is developing a technology that will access the primary tank floor of AY102 through the annulus and refractory air slots (Figure 66) and provide visual feedback of the condition within the air slots. The refractory air slots range from 1 inch to 3 inches in width and provide a complex maze to navigate through, including four 90° turns to reach the center of the tank (Figure 67).

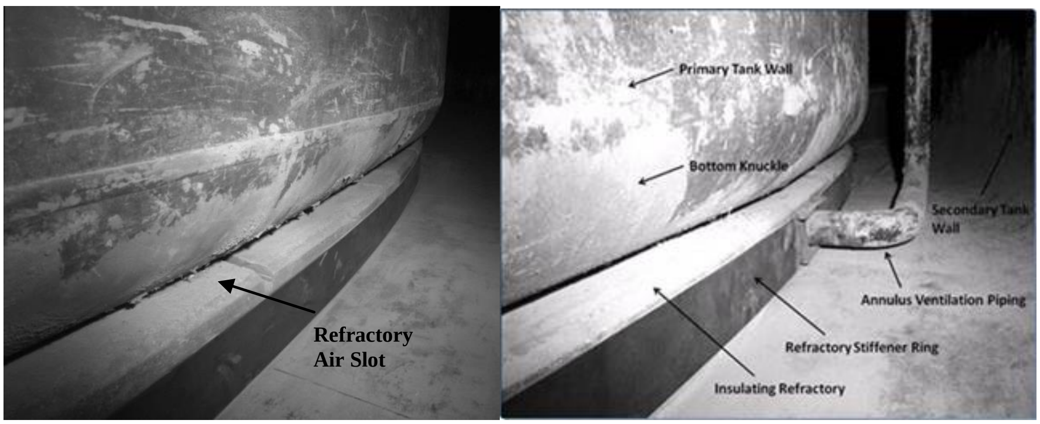

Figure 66. Side view of primary tank and refractory air slot.

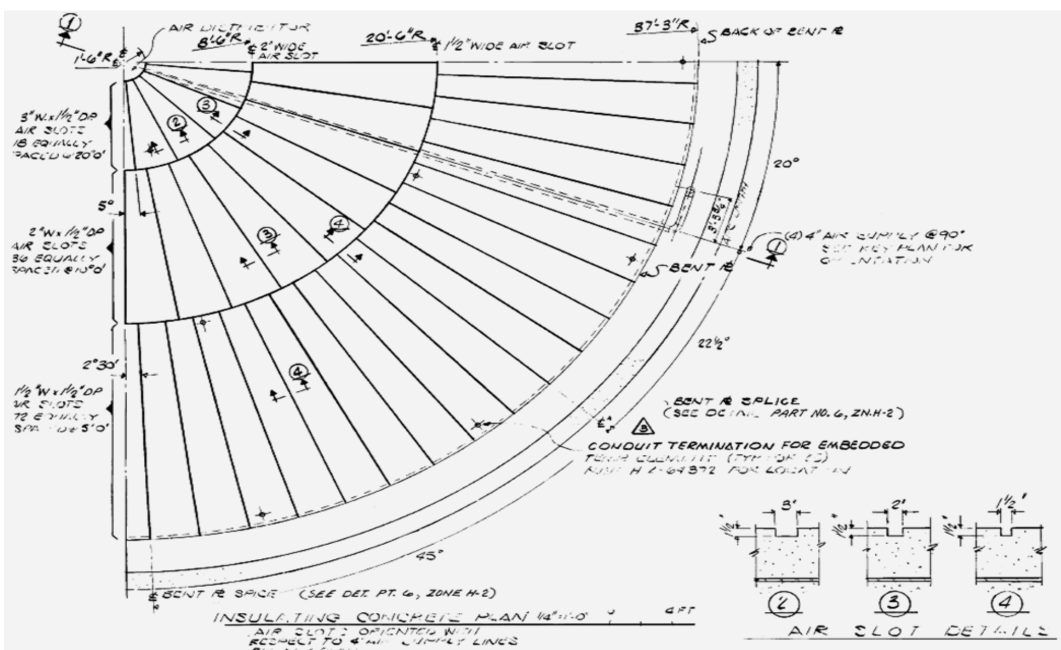

Figure 67. Refractory air slot layout and description.

In conjunction with site engineers, FIU has gathered information that has been used to establish the design specifications for the inspection tool. This includes annulus and refractory air slot geometry and maximum temperature and radiation limits for the device. Discussions with the engineers on the condition of the carbon steel along the tank bottom led to the viewing of refractory air channel video inspections for tanks AW-101, AZ-102, and SY-103 that were performed ten years ago with an articulated robot inside the annulus. The video provided FIU with a general idea of the conditions that will be encountered in the air channels, as well as the primary tank bottom surface condition. The video also provided FIU with a better understanding of the refractory pad's low shear strength and how easy it is to create debris (Figure 68).

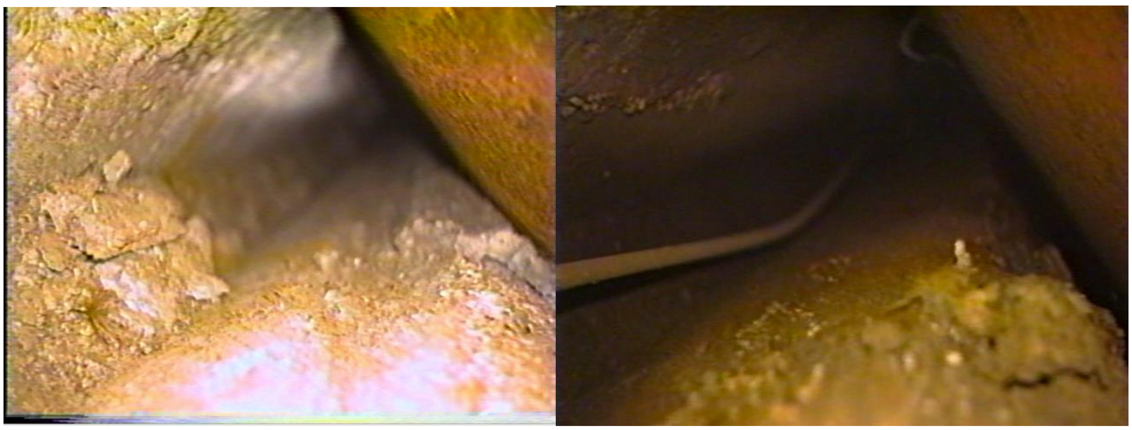

Figure 68. Debris seen in refractory air slots.

Design Concept

A prototype inspection tool was initially designed and the proof-of-concepts were validated via bench scale testing. Various design modifications have been implemented after a number of bench scale tests. Efforts in improving the design have been focused on minimizing the complexity of the design while retaining efficiency.

The previous design iterations served as a platform upon which modifications were introduced after observations from its performance during the testing. Figure 69 shows a previous four-motor design of the inspection tool. This inspection tool had 8 wheels, four of which were driving, providing power to pull the tether and traverse through a mock up channel. The purpose of free rolling wheels was to improve the tool’s stability over a straight path and increase its obstacle avoidance capability. Shaving the hub of the wheels reduced the width of the tool and a magnet was built into the bottom, surrounded by a loft to avoid any debris from wedging into the edge of the body and magnet.

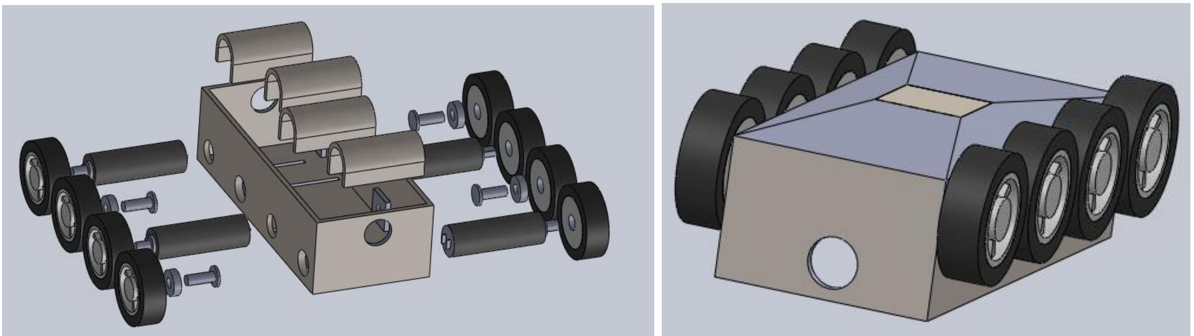

Figure 69. Exploded view from initial design of the inspection tool and loft design in the bottom to embed the magnet.

Recent design modifications in the inspection tool focused on optimizing the magnet size and improving the camera and motor installation. Press-fit cap holders were unreliable in securing the motors. To keep the motors from spinning and allowing for the removal of a single motor in the event one fails, a design modification was introduced to the main body which included fixing the motors using half cylinder seats. Previously, adhesive was used to affix the motors to the body. Another potential drawback of using adhesives stems from elevated operational temperatures in the refractory air channels. Elevated temperatures could adversely affect the adhesive and the effectiveness of the motors. Thus, a bracket was mounted over the motors and is secured via five pairs of 10 mm M2 bolt and nuts fasteners (Figure 70).

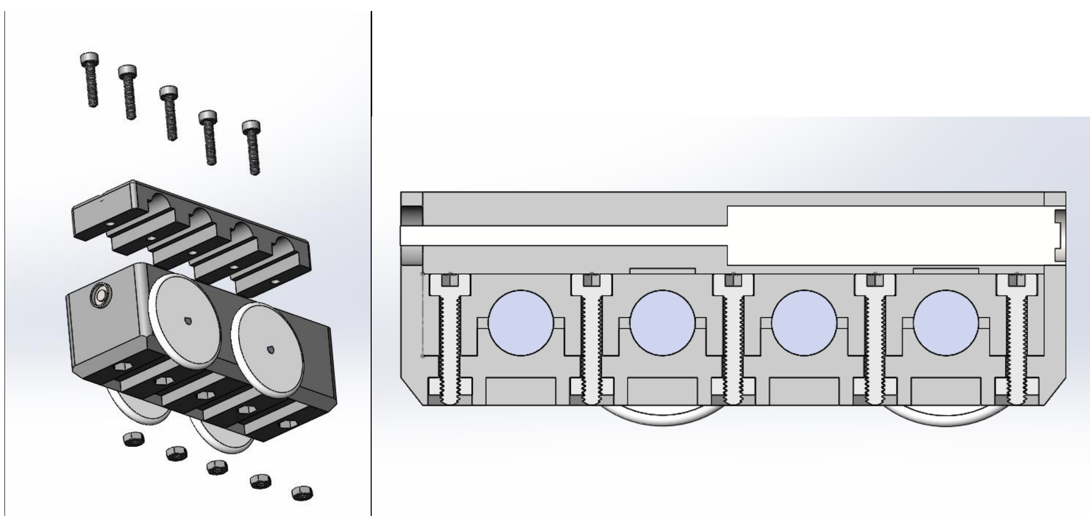

Figure 70. Exploded view of the modified design for inspection tool and section view of assembly.

A single, larger magnet was replaced with four separate neodymium magnets (3/4" long, 1/4" wide, 0.1" thick, each with 3 lbs maximum pull force). This allowed space in the bottom of the inspection tool for the nuts required to hold the bracket in place. This also provides a uniform distribution of magnetic force to improve obstacle avoidance. In the event of a part failure, a replacement could now easily be swapped into place without replacing the whole inspection tool.

Due to a limitation in the availability of off-the-shelf wheel components, a new design for the wheels was introduced. For this modification, the diameter of the wheels is 20 mm and the width is reduced to 2.9 mm. A groove around the boundary of wheel allows for the installation of a square-profile high-temperature silicone O-ring which can provide suitable surface traction between the wheel and tank. Figure 71 shows the 3D printed components with magnets and flat O-rings assembled.

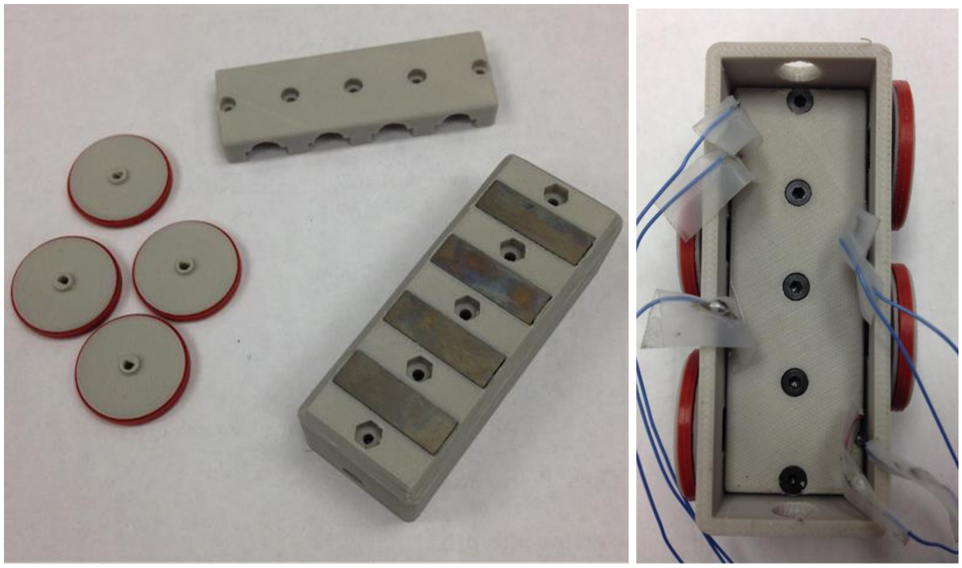

Figure 71. 3D printed components, magnets and assembled wheels and assembled inspection tool.

Additionally, a new control circuit for the inspection tool was assembled which consists of a Arduino Mega ADK, two DRV8835 dual motor driver carriers and a parallax 2-Axis joystick (Figure 72).

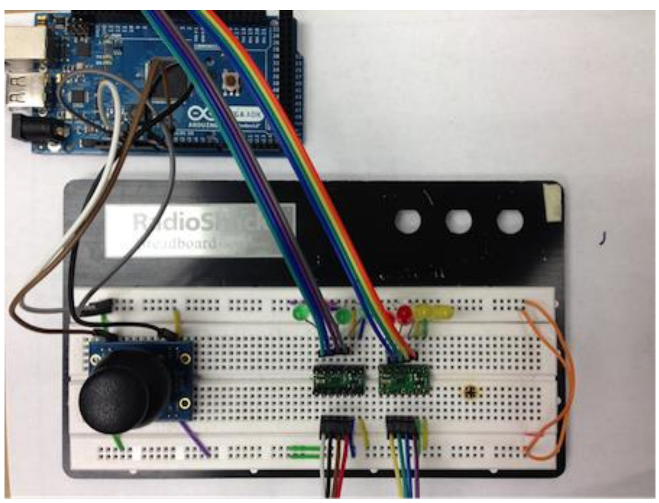

Figure 72. Arduino board and control circuit for the inspection tool.

Experimental Testing

In order to evaluate the inspection tool’s performance, a lab-scale test bed was designed and developed to mimic the refractory air channels. This test bed is comprised of two 8-ft modules and a 1-ft module to model the first 17-ft section of path. For future tests, new modules will be added to model the remaining sections of the refractory channels.

Each module is comprised of two long pine boards for the channel walls, a carbon steel flat bar (0.25 in×2.5 in×8 ft.) for the tank bottom and a transparent acrylic plastic sheet on one side to provide a view of the test bed. The cross sectional area is 1.5 in × 1.5 uniformly throughout the entire course to accurately emulate the refractory air channels. Figure 73 shows one of two 8-ft channels with the inspection tool navigating inside it. Testing demonstrated that the unit had the necessary power to traverse 17 ft with the tether dragging along the channel.

Figure 73. Mock-up test bed with inspection tool deployed.

The inspection tool was evaluated in the test bed multiple times and possible areas of improvement were identified. A live demo was presented to WRPS engineers, who provided valuable feedback. In some of the testing trials, the tool traveled the entire course and pulled the tether with no issue. In other trials, there was contact between the inspection tool wheel and plastic side of the channel, requiring the tool to reverse and correct its direction. Additionally, the tool stalled upon meeting the uneven joint between the two sections of steel.

During initial testing, one of the DC motors failed, requiring an assembly of an entire new inspection tool due to the use of adhesive in that design iteration. This failure prompted the design modifications that were previously mentioned.

Subsequently, a series of tests were conducted to identify the pull force performance of the inspection tool. The tests were conducted by placing weights on the front of the inspection tool as it navigated up a vertical column (Figure 74).

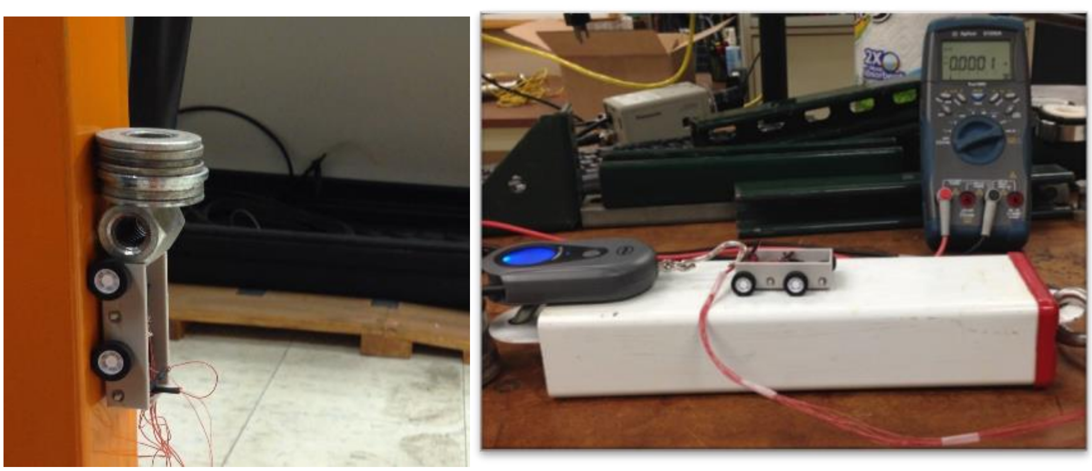

Figure 74. Maximum pulling force identification through weight test and measurement scale.

In another testing trial, a scale with 1 gram force resolution measured the maximum pull force of the inspection tool. The scale was lifted up 1.25 inches to simulate the real condition in which the device will be deployed and eliminate the moment from the hook of the instrument. The 16.7 gf weight of the tool is considered negligible compared to the 4.53 lb. magnet force. The measurements from the tests are shown in Table 11.

Table 11. Maximum Pull Force for Inspection Tool

	Bare weight	**Camera and tether added**
Inspection tool weight	16.8 gf	24.7 gf
Max. Force – from start	213.4 gf	199.1 gf
Max. Force – to stall	268.4 gf	254.1 gf
Power: weight – from start	12.7	8.1
Power: weight – to stall	16.0	10.3

PNEUMATIC PIPE CRAWLER

Background

The objective of this subtask is to develop a tool that will carry out the robotic inspection of the ventilation header piping, leading to the central plenum, of the AY-102 double-shell tank at Hanford DOE site, and provide live visual feedback.

The proposed inspection of the ventilation header is about 100 feet from grade, down through one of the drop legs, and then lateral to the center bottom of the tank secondary containment, as shown in Figure 75 below. The route consists of schedule 40 pipes which are 3 and 4 inches in diameter, reducers and several elbows. The four drop legs branch from the “header ring” with a diameter of 3 inches, transitioning then to 4 inches.

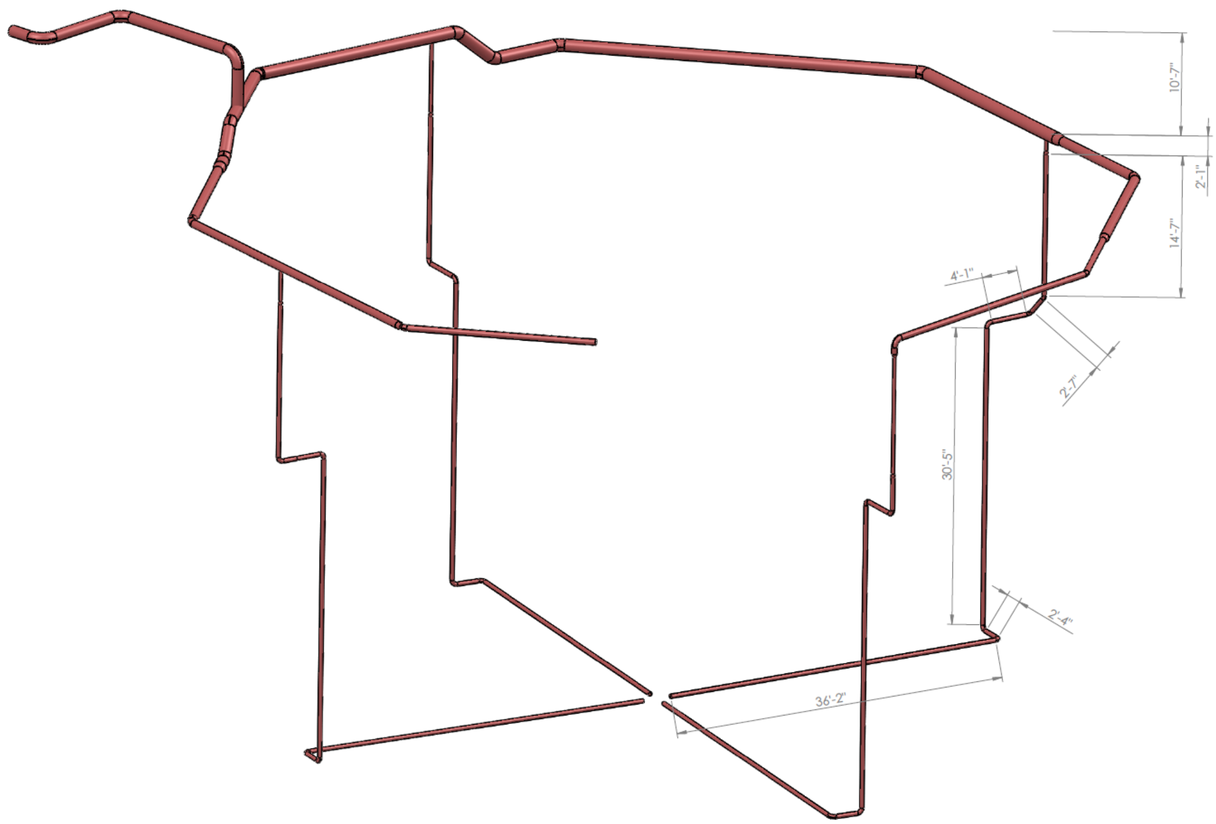

Figure 75. The ventilation header of the AY-102 tank at Hanford.

During the initial design phase, two options were explored:

- modify the existing peristaltic crawler previously developed by FIU, and
- design a new crawler.

The FIU existing crawler, shown in Figure 76, is a pneumatically powered worm type device that propels itself by a sequence of pressurization and depressurization of cavities constructed on a flexible assembly. The flexible body allows the existing crawler to navigate through straight sections and 90° elbows, and it was designed to unplug 3-inch pipelines. The device also has a camera, and it can be utilized as an inspection tool as well.

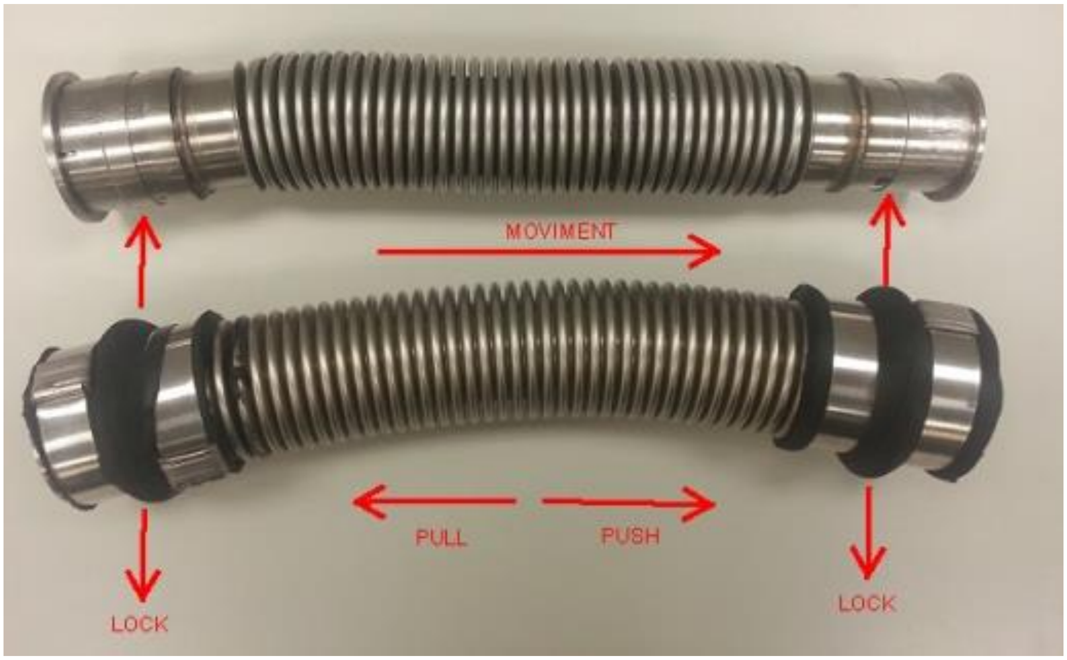

Figure 76. The existing pneumatic pipe crawler previously developed by FIU.

FIU's existing peristaltic crawler has a novel and robust design. The device is able to crawl inside a pipeline without using any moving parts, motors, or actuators, using only pneumatic inflatables which are suitable for harsh environments and critical applications. Several prototypes were built and successfully tested under restricted conditions. The existing crawler design shows potential for being a valuable pipeline unplugging tool for highly toxic, high-level radioactive waste stored systems.

However, the proposed inspection of the ventilation header of AY-102 double-shell tank would require the redesign of the rubber inflatables, located at both ends of the existing crawler. New inflatables would have to be designed to grip not only to 3, but also to 4 inch pipe diameters. A straightforward solution would be the use of balloon type inflatables, such as the one exemplified in Figure 77. The solution may not require drastic modifications to the current rims, but it would require the manufacturing and testing of custom-made bladder type inflatables. Also, the use of balloon type inflatables could aggravate previously noted durability issues associated with the hyperinflation and stresses rise in the rubber material during operation.

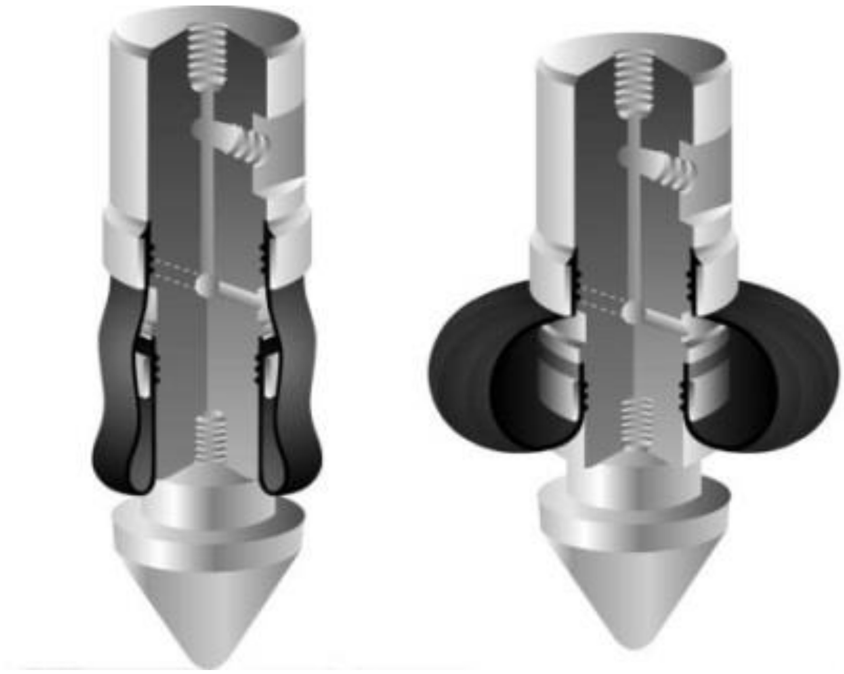

Figure 77. Example of a balloon type gripper.

The design of a new pneumatic crawler was the action taken for the inspection of the ventilation header of the AY-102 double-shell tank. In comparison to the requirements of the unplugging task of the existing crawler, the tether dragging force in the new inspection task will be considerably lower, due to a shorter crawling distance and the absence of an unplugging pressurized water hose in the tether. In addition, the dry environment with considerably lower radiation level would allow a new design that utilizes off-the-shelf compact actuators and gripping mechanisms instead of inflatables. If properly designed, a mechanical gripping mechanism would be more predictable and more reliable than the current rubber inflatables used in the existing crawler.

Design Concept

The designed pneumatic pipe crawler is a snake type robot with a modular design, composed of interchangeable cylindrical modules connected with flexible links. The design is an evolution of previous peristaltic crawlers developed at FIU, and has the following design requirements:

1) Crawl thru pipes and fittings which are 3 and 4 inches in diameter;
2) Climb vertical runs;
3) Tow around 50 lbs of tether drag[2];
4) Provide live visual feedback;
5) Tolerate elevated temperature (170 F);
6) Tolerate moderate radiation levels (85 rad/hr);

[2] Tether drag baseline will be experimentally verified.

7) Provide a means for removal in the event of a malfunction.

Figure 78 below shows an early design of the new pipe crawler. The new design uses pneumatic actuators to emulate the contractions of the peristaltic movements of the existing FIU crawlers, which is suitable for highly radioactive environments by not requiring embedded electronics, with the exception of a camera.

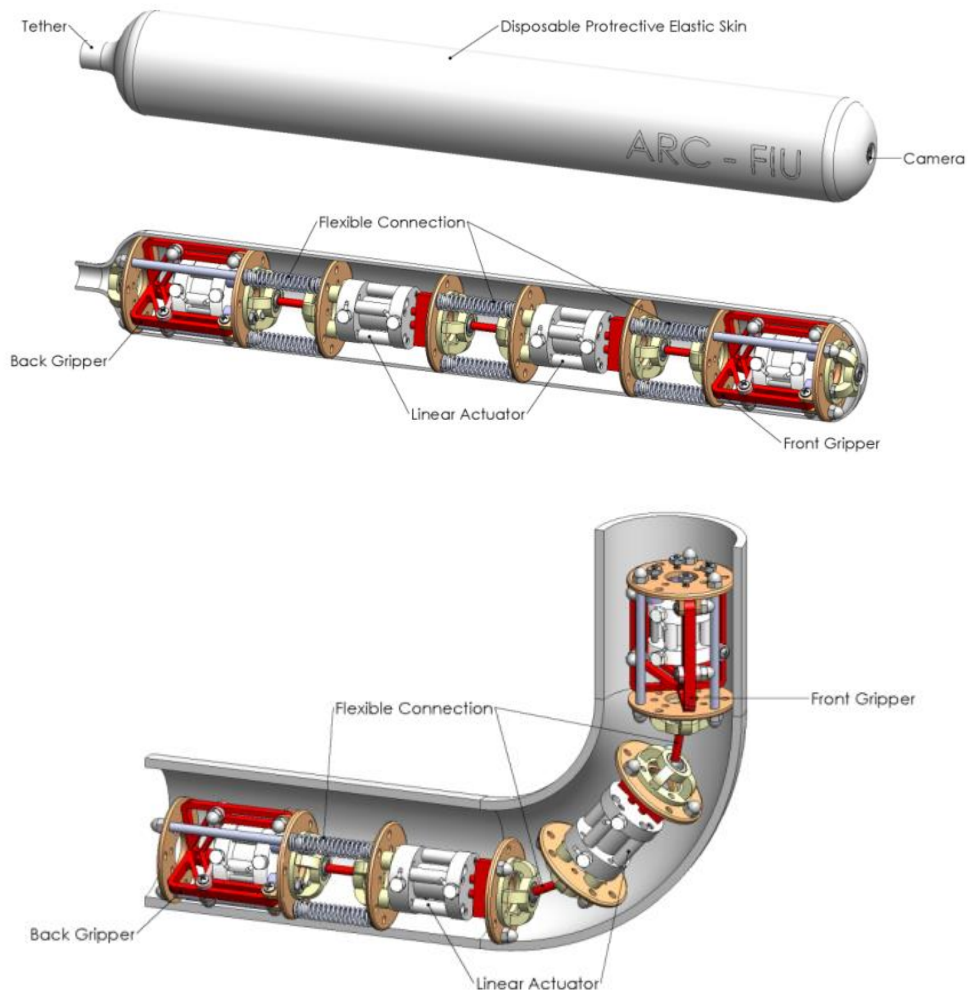

Figure 78. Pneumatic pipe crawler conceptual design.

The primary advantage of using a peristaltic locomotion concept in the design of the inspection tool is that the device can crawl inside a pipeline without using any external moving parts, such as wheels and continuous tracks. Therefore, the device can be fully encapsulated with a disposable protective skin, which is suitable for decontamination in harsh environments and critical applications.

The modular design of the new inspection tool, using interchangeable modules, has the potential to be customized for specific tasks with the addition of extra modules, such as instrumentation, material sampling, and pipe repair.

The new design is composed of two linear actuators, which propel the device using gripping mechanisms located at both ends of the crawler. Figure 79 shows the chief dimensions of the new crawler.

An overall picture of the key components of the crawler is briefly presented, as follows:

- the linear actuators,
- the gripping mechanism,
- the tether,
- the camera, and
- the overall control system.

Following the component description, a functioning prototype is also presented. Finally, a path forward plan is provided.

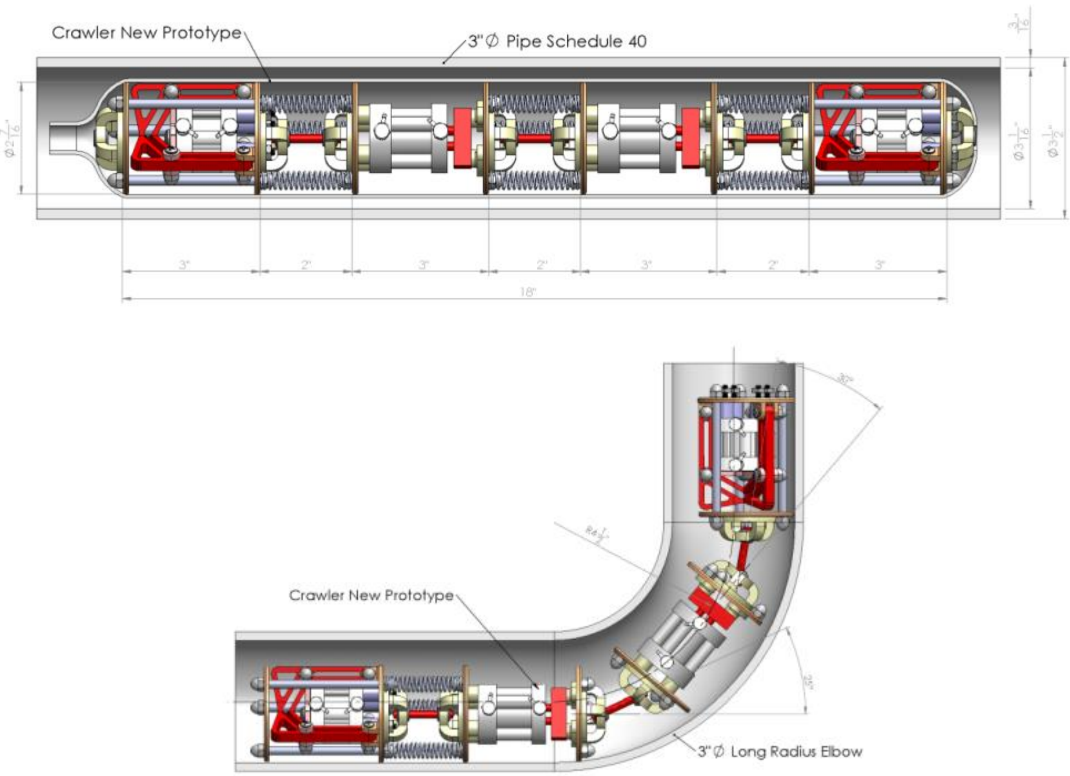

Figure 79. Pneumatic pipe crawler modular design.

Linear actuators

The linear actuators propel the device forward, using compact nonrotating tie rod air cylinders. These cylinders have two parallel piston rods that prevent the head from twisting as they extend and retract which prevents the crawler rotation, and consequently, prevents the rotation of the live video feedback as well.

Gripping Mechanism

The gripping mechanism, shown in Figure 80, was designed to grip pipes with an internal diameter varying from 3 to 4 inches. The mechanism was also designed to be self-locking, possibly allowing gripping forces greater than the one provided by the pneumatic actuator (40 pounds). In that case, the actuator will only open and close the mechanism, the locking would be carried out by the body of the module.

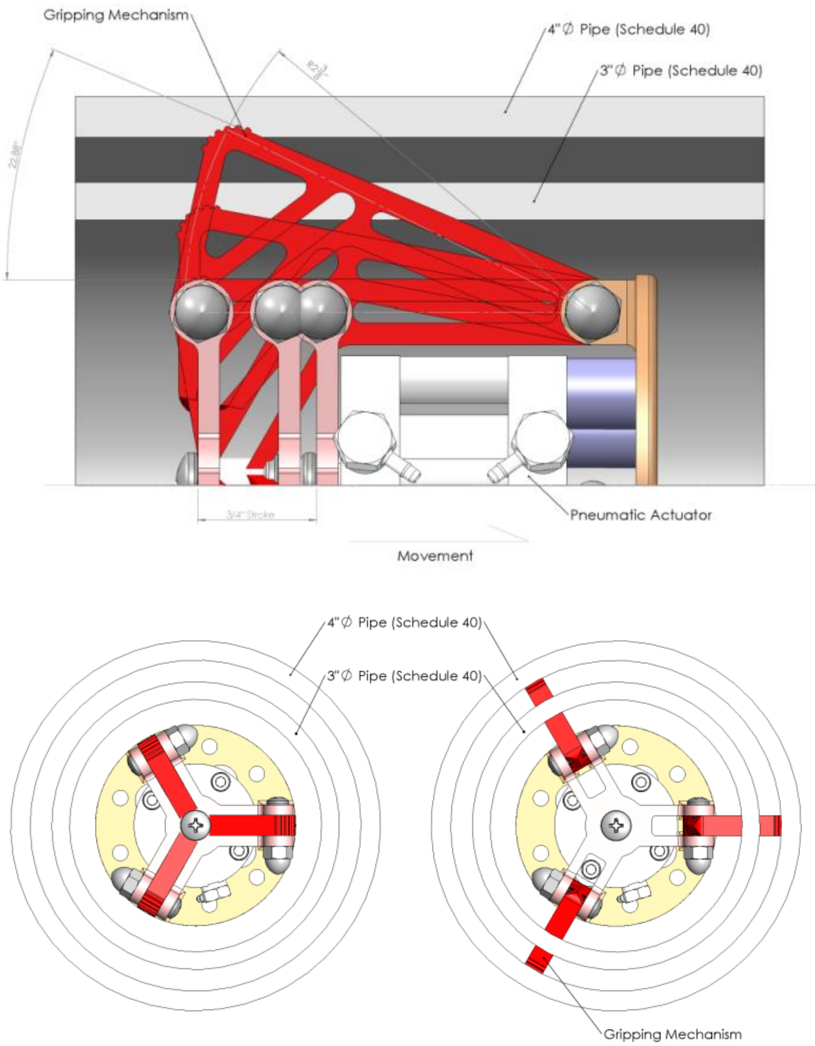

Figure 80. Pneumatic pipe crawler gripping mechanism design.

The maximum locking force exerted by the gripping mechanism is the main determinant of success in designing the new peristaltic crawler. The maximum theoretical gripping force F_{max} was estimated using the gripper free body diagram shown in Figure 81. The tether dragging force T must be held by the frictions F, between the gripper claws and the pipe, during the peristaltic movement; the radial compression forces C counterbalance themselves.

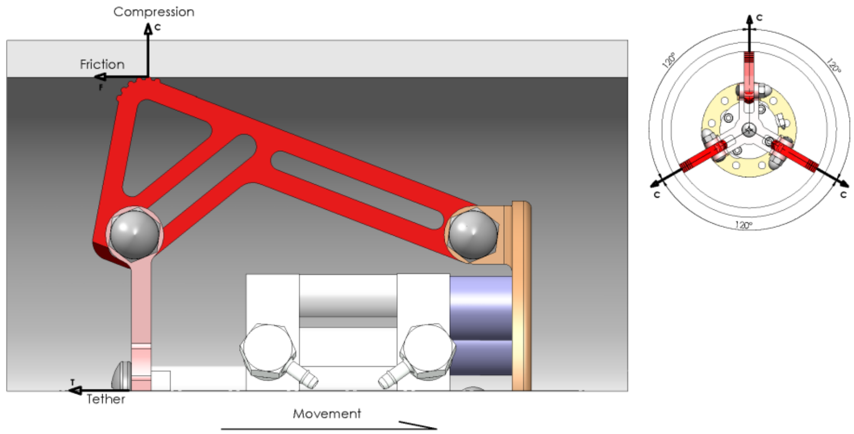

Figure 81. **Pneumatic pipe crawler gripper free body diagram.**

Based on the body static equilibrium

$$\sum F_x = 0 \Longrightarrow F = \frac{T}{n}$$

where n is the number of claws, and the maximum gripping force F^*_{max} per claws is

$$F^*_{max} = \mu_s N$$

where μ_s is the coefficient of static friction of the surfaces in contact, and N is the contact normal force and is also equal to C.

The radial compression forces C were determined using the individual claw free body diagram shown below in Figure 82. The pneumatic actuator opens and clamps the claws with a force A equal to

$$A = \pi b^2 p$$

where b is the bore of the cylinder, and p is the supplied air pressure. Based on the claw static equilibrium

$$\sum M_O = 0 \Longrightarrow P_y(s + a) + Fl_2 - Nl_1 = 0$$

where s is the pneumatic piston stroke, a, l_1, and l_2 are function of the mechanism geometry. P is the normal force transmitted to each claw by the pin attached to the pneumatic piston assembly

$$nP_x = A + T \Longrightarrow P_x = \frac{A + T}{n}$$

The normal force per claw is then

$$N = \frac{(s + a)}{n \tan \phi \, l_1}(A + T) + \frac{l_2}{l_1}F$$

Finally, the maximum total theoretical gripping force is

$$F_{max} = n \cdot \mu_s \left[\frac{(s + a)}{n \tan \phi \, l_1}(A + T) + \frac{l_2}{l_1}F\right]$$

or

$$F_{max} = \mu_s \left[\frac{(s+a)}{\tan\phi\, l_1}(\pi b^2 p + T) + \frac{l_2}{l_1} T\right]$$

where the angle ϕ is

$$\phi = \pi - (\beta + \theta)$$

The angle β is constant, and the angle θ can be calculated applying the Law of Sines to the triangle ΔOMW shown in Figure 82 as well

$$\frac{s+a}{\sin\beta} = \frac{x}{\sin\theta} \Rightarrow \theta = \sin^{-1}\left(\frac{x\sin\beta}{s+a}\right)$$

x can be also calculated applying the Law of Cosines to the same triangle ΔOMW

$$(a+s)^2 = x^2 + a^2 - 2ax\cos\beta$$

which leads to a second order polynomial equation

$$x^2 - 2a\cos\beta x + a^2 - (a+s)^2 = 0 \Rightarrow x = \frac{2a\cos\beta \pm \sqrt{(2a\cos\beta)^2 - 4[a^2 - (a+s)^2]}}{2}$$

the positive root is the solution for x.

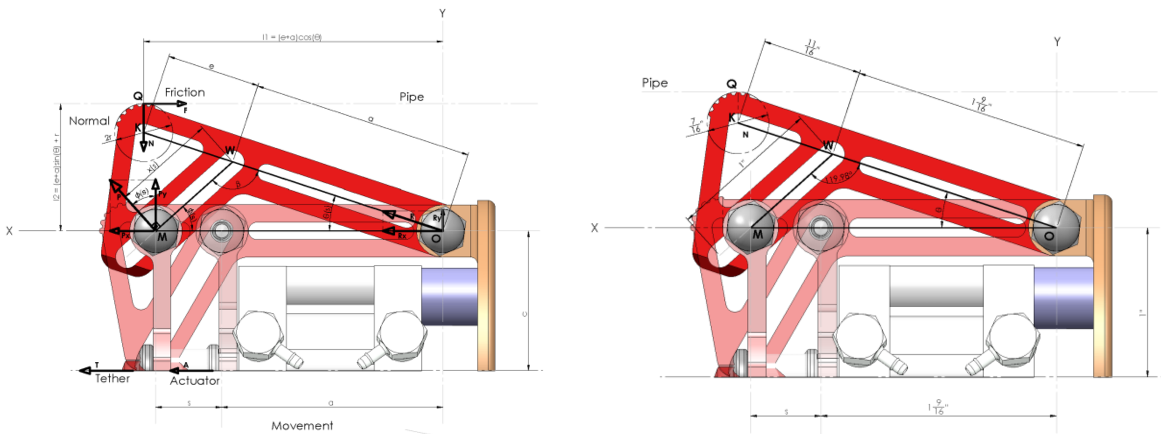

Figure 82. Pneumatic pipe crawler gripping mechanism forces and geometry.

The computed results of the maximum total theoretical gripping force are presented below in Figure 83. The preliminary results show, that using a claw with rubber coated tip, the gripping mechanism could hold a maximum tether force around 33 pounds in a pipe with 3 inches diameter, and around 110 pounds in a pipe with 4 inches diameter. These values need to be experimentally confirmed. A priori, they seem adequate for the proposed inspection at Hanford site.

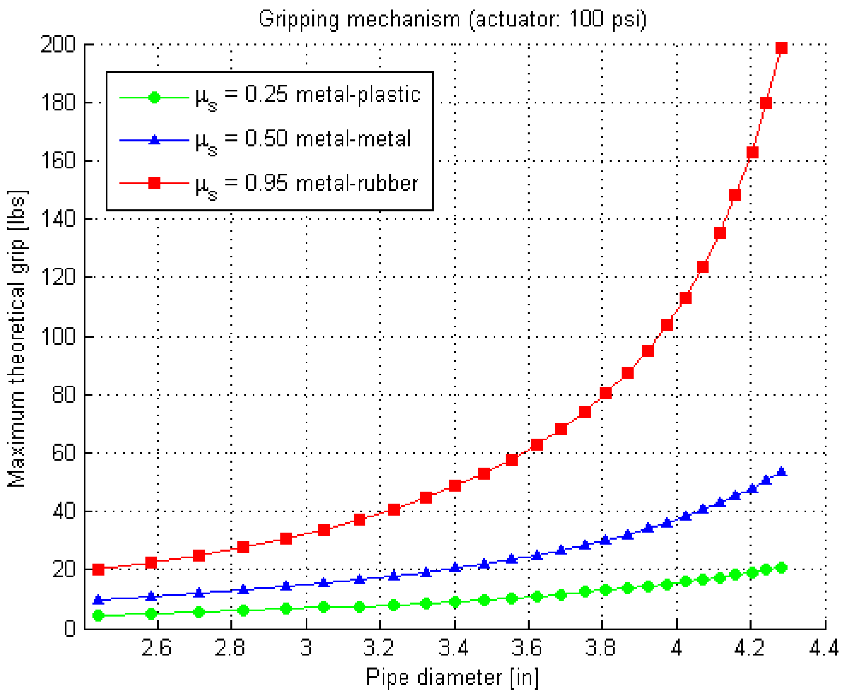

Figure 83. Pneumatic pipe crawler maximum theoretical gripping force.

Tether

The tether required for the proposed inspection is about 100 feet long, and it consists of:

- 8 pneumatic lines,
- 1 digital video feedback cable, and
- 1 retrieval steel cable.

During dragging, the retrieval cable will be responsible for carrying out the pulling load, relieving any tension in the other lines of the tether. The bundle will also be enclosed by an abrasion-resistant sleeve, which will reduce drag and protect the cables from wear and tear.

Camera

The front camera module carries a day-night 1.0 megapixel (720p) digital camera, with infrared cut-off filters and LEDs, illustrated by Figure 84. Being an independent module, the camera can be easily replaced accordingly to the specific application.

Figure 84. Pneumatic pipe crawler camera module.

Control System

An overall picture of the subsystems involved in the crawler operation is schematized in Figure 85 below. Further, the schematic of the portable control box is enlarged for better reading, in Figure 86. A portable control box will be suitable for the field deployment of the crawler. We envision the crawler being controlled remotely using any handheld device connected to its secure wireless private network, running a custom-made application which will make the inspection tool highly customizable, not having any dedicated control interface.

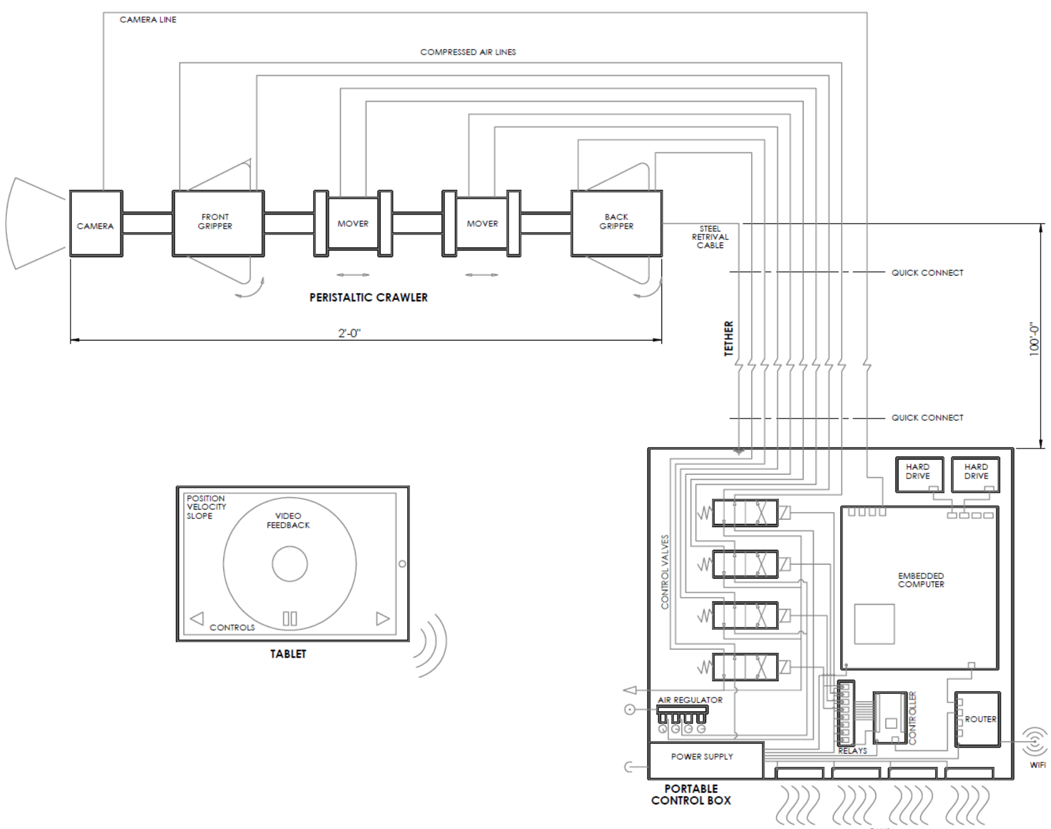

Figure 85. Schematic of the pneumatic pipe crawler control system.

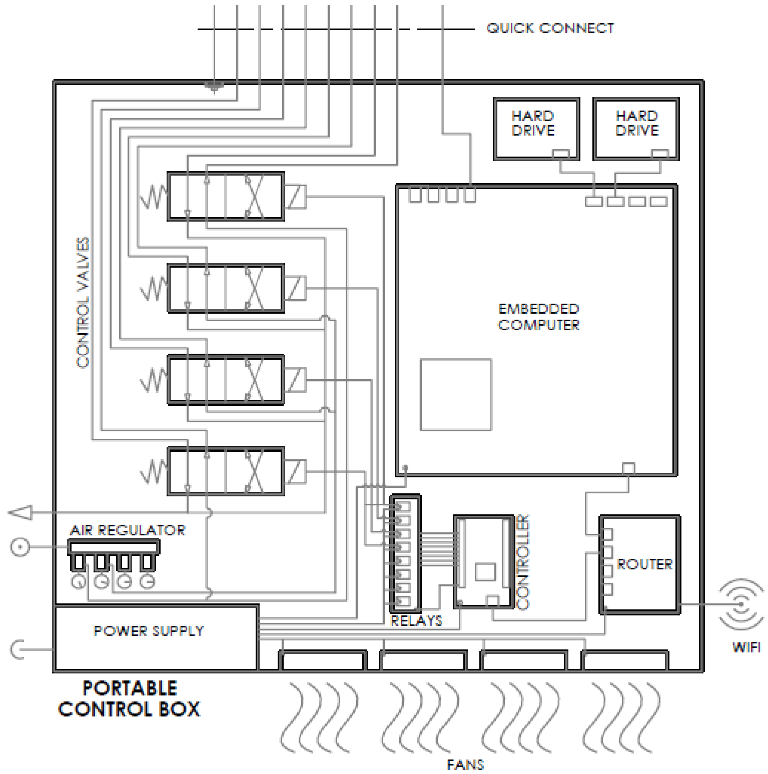

Figure 86. Schematic of the pneumatic pipe crawler portable control box.

The crawler motion system is fully automated. The system consists of:

- four pneumatic actuators,
- an air pressure regulator with four ports,
- four 120 volts pneumatic two-way control valves,
- a relay bank, and
- a dedicated microcontroller.

To produce the crawler peristaltic movement, the pneumatic actuators are controlled by valves connected to a relay bank, which is controlled by a dedicated microcontroller using digital ports.

Tests and Result

A functional crawler prototype was fully designed, built, assembled, and preliminarily tested. Figure 87 shows the most recent design of the crawler.

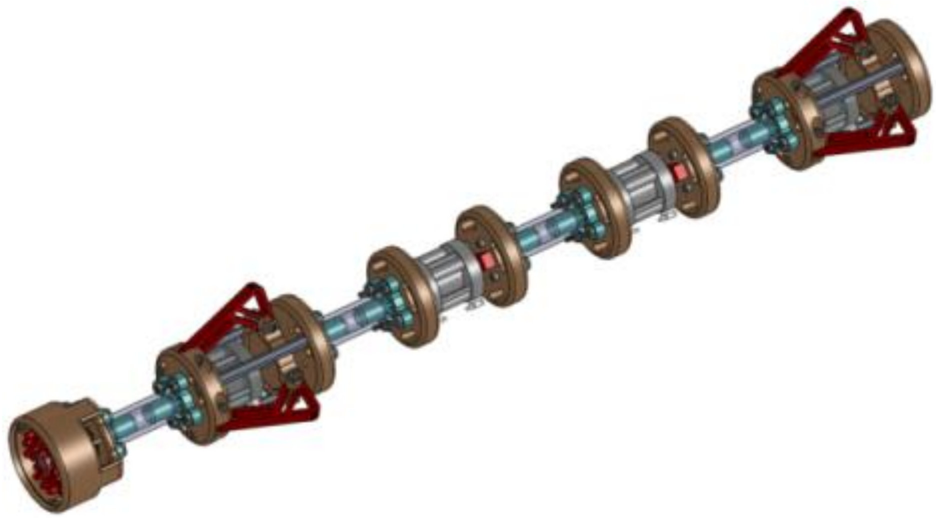

Figure 87. Most recent pneumatic pipe crawler design.

The 3D printed prototype, shown in Figure 88, not only was able to successfully crawl horizontally and vertically through pipes, with 3 and 4 inch nominal diameters, but was also able to negotiate through elbows.

Figure 88. Pneumatic pipe crawler prototype.

The crawler grip seems satisfactory in performing the proposed inspection task. Figure 89 shows preliminary pulling tests being executed using a hand scale. However, more elaborate and detailed tests will be conducted to experimentally verify the maximum gripping force, which was already theoretically predicted.

Figure 89. Pneumatic pipe crawler preliminary pulling tests.

In addition, the gripper mechanism structure was reinforced as shown below in Figure 90. The original gripper was designed to be manufactured in metal, and a 3D printed version of it is not strong enough to endure some preliminary tests. The use of thermoplastic 3D printed parts has expedited the design process of the new crawler.

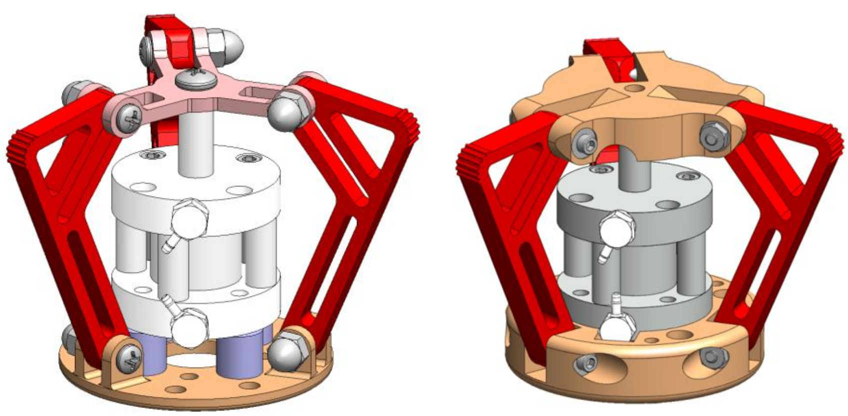

Figure 90 .Crawler gripper original design (left) and strengthened redesign (right).

Figure 91 shows the prototype complete setup including crawler, tether, valves, relay bank, and dedicated microcontroller. Currently, the crawler can be controlled remotely using any handheld device connected to its secure wireless network.

Figure 91. Pneumatic pipe crawler complete setup.

The path forward includes the execution of engineering scale mock up testing. In addition, several kinds of suspension mechanisms will be investigated with the objective of keeping the crawler at center while crawling through pipes and fittings. This will minimize the drag force and the bulldozer effect, which is the collection of debris in the front camera. Finally, additional design modifications will be implemented, as needed.

CONCLUSIONS AND FUTURE WORK

A magnetic miniature inspection tool was designed to be capable of traveling through the refractory cooling channels and provide live video feedback of the channels and tank floor of AY-102.

Lab-scale mock up tests revealed a few modifications that can be implemented to improve the robustness of the current design. Some of these modifications include: (1) a redesigned clamp system for securing the motors, (2) a rearrangement of the magnets for better attachment to the tank floor, (3) the use of a press fit or sliding mechanism for fastening of the magnets, (4) the use of an ultra-thin USB camera cable for tether drag reduction, (5) redesigning of the wheels for improved obstacle avoidance, and (6) a reduction of the overall width of the device. Options for deploying the unit through an annulus riser are also being investigated.

The path forward for this inspection tool will include validation of the aforementioned design modifications by conducting tests on more realistic mock up testbeds. These testbeds will be generated with the assistance of site engineers at WRPS.

A pneumatic pipe crawler that will carry out the robotic inspection of the ventilation header piping of the AY-102 tank was also successfully designed. The device will provide live visual feedback, but plans for carrying other instruments are being considered. A functional prototype was successfully built, and the preliminarily tests were satisfactory.

A path forward includes the execution of engineering scale mock up testing, in which, the pneumatic pipe crawler will be able to carry out automatic pipe inspections. In addition, several kinds of suspension mechanisms will be investigated with the objective of keeping the crawler at center while crawling through pipes and fittings, which will also minimize the dragging and the bulldozer effect, the collection of debris, in the front camera. Finally, design modifications will be implemented as needed.

TASK 19.1 PIPELINE CORROSION AND EROSION EVALUATION (FIU YEAR 5)

EXECUTIVE SUMMARY

Washington River Protection Solutions (WRPS) has implemented a fitness-for-service program which will evaluate the degraded condition of the tank farm waste transfer system. The Tank Farms Waste Transfer System Fitness-for-Service Requirements and Recommendations, includes a requirement to inspect primary piping, encasements, and jumpers for corrosion/erosion. In years past, the 242-A Evaporator pump room was upgraded by adding instrumentation to the feed and return jumpers, prior to running the next campaign. As part of this campaign, five jumpers were selected for ultrasonic thickness (UT) inspection. The jumpers selected were the following: 18-4, C-4&5, J-13A, 13-K, and 19-5. All of these jumpers were removed permanently except for jumper 19-5 which will be reinstalled for further service. As part of this study, several jumpers from the AW-02E Feed Pit were also removed for disposal and two were selected for UT inspection. The jumpers selected were the 1-4 and B-2 which were packaged and sent to the 222-S Laboratory for UT assessments. All of the thickness measurements were evaluated and estimated remaining useful life (ERUL) values were obtained.

In continuing with this effort, this year's task focused on evaluating nozzles from the POR104 valve box. The POR104 is a portable valve box located in the C-Tank Farm at Hanford. It contains four floor nozzles that are comprised of 2-in Schedule 40 ASTM A312 TP 304L stainless steel pipes and elbows joined with Chem-Joints. A 2-in. Purex nozzle was also welded to the other end of the elbows. The POR104 transferred approximately 7.27 million gallons of supernatant and 7.83 million gallons of slurry waste through the four floor nozzles- B, C, E, and F. Nozzles B and E were used to transfer slurry tank waste and nozzles C and F were used to transfer supernatant tank waste

This report includes details of each waste transfer component comprised in the nozzles that are evaluated in the POR104 valve box. As done previously, UT measurements for each floor nozzle were obtained by engineers at Hanford and that data was provided to FIU for analysis. In analyzing the data, trends are assessed for each component using radial and longitudinal thickness averages. The data indicates that minimal wear has occurred on these components and the ERUL will far exceed the life expectancy of WTP.

Additionally, effort this year focused on evaluating various UT sensors for obtaining real time thickness data on components in the HLW transfer system. Previous efforts by WRPS were not successful in obtaining reliable real time thickness data. Thus, our task also focused on understanding the state-of-the-art in UT sensors and identifying technical gaps that exist for obtaining this type of data.

INTRODUCTION

Washington River Protection Solutions (WRPS) has implemented a fitness-for-service program which will evaluate the degraded condition of the tank farm waste transfer system. The Tank Farms Waste Transfer System Fitness-for-Service Requirements and Recommendations [1], includes a requirement to inspect primary piping, encasements, and jumpers for corrosion/erosion. FIU-ARC engineers have worked closely with key Hanford HLW personnel on analyzing the data from various system components, determining wear rates and identifying key parameters that contribute to the wear rates.

Previous efforts have included the evaluation of five jumpers from the 242-A Evaporator Pump room using ultrasonic thickness (UT) inspection. These included jumpers 18-4, C-4&5, J-13A, 13-K, and 19-5. All of these jumpers were removed permanently except for jumper 19-5 which will be reinstalled for further service. The UT measurements collected from jumper 19-5 will assist in future 242-A integrity assessments. As part of this study, several jumpers from the AW-02E Feed Pit were also removed for disposal and two were selected UT inspection. The jumpers selected were the 1-4 and B-2 which were packaged and sent to the 222-S Laboratory for UT assessments.

During FIU Year 5 (FY14), efforts for this task focused on evaluating nozzles from the POR104 valve box. The POR104 is a portable valve box located in the C-Tank Farm at Hanford. It contains four floor nozzles that are comprised of 2-in Schedule 40 ASTM A312 TP 304L stainless steel pipes and elbows joined with Chem-Joints. A 2-in. Purex nozzle was also welded to the other end of the elbows. The POR104 transferred approximately 7.27 million gallons of supernatant and 7.83 million gallons of slurry waste through the four floor nozzles- B, C, E, and F. Nozzles B and E were used to transfer slurry tank waste and nozzles C and F were used to transfer supernatant tank waste. Figure 92 shows drawings of the POR104 valve box indicating the layout and position of the four floor nozzles.

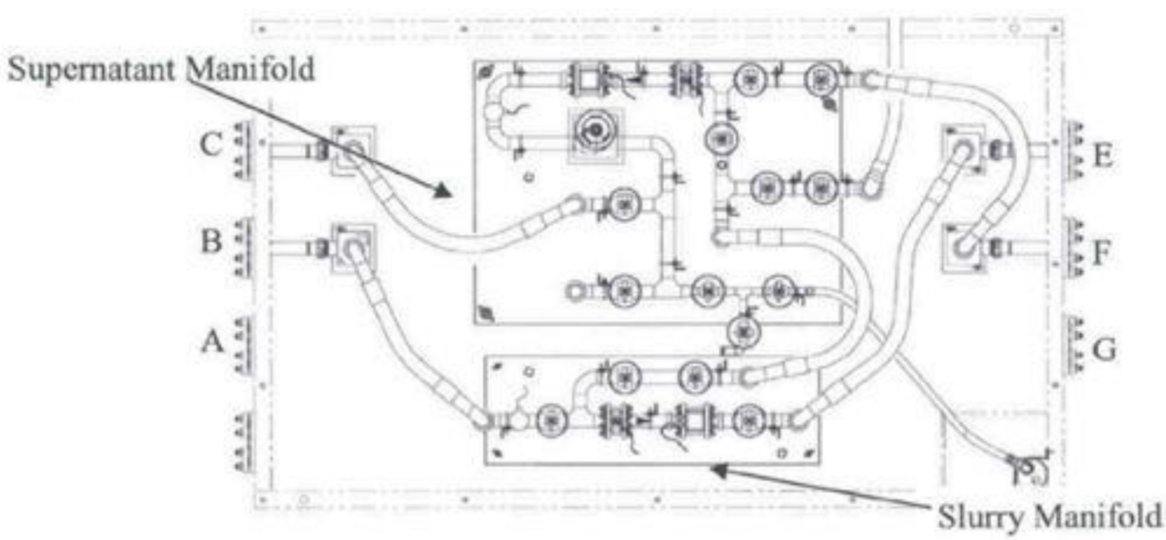

Figure 92. Layout of POR 104 valve box.

This section first provides the detailed procedure for how the data is measured and analyzed using the information obtained from Nozzle B. Similar procedures were used for the three additional nozzles but only a summary of the data is presented.

Efforts this year also focused on evaluating ultrasonic transducers that can provide real-time thickness measurements of transfer system components. Previous work at WRPS utilized a pipe wrap system that had UT sensor imbedded in a polymer wrap. Variations in installation procedures demonstrated that this system did not provide reliable data. In some cases, the installation of the system caused failure in the sensors. Thus, FIU has taken on the task of determining the state-of-the-art of the UTs and their applicability to real time measurements.

POR104 VALVE BOX

Nozzle B

Nozzle B of the POR104 valve box was fabricated with a 2” schedule 40 pipe made of ASTM A312 TP 304L stainless steel. It was installed in 2004 and transferred approximately 7.83 million gallons of slurry waste. The nozzles served as connection points between the C-Tank Farm hose-in-hose transfer lines and the valve manifolds which allowed the routing of single-shell tank (SST) waste to the recipient double-shell tank (DST) 241-AN-106. A CAD illustration of the jumper is provided in Figure 93.

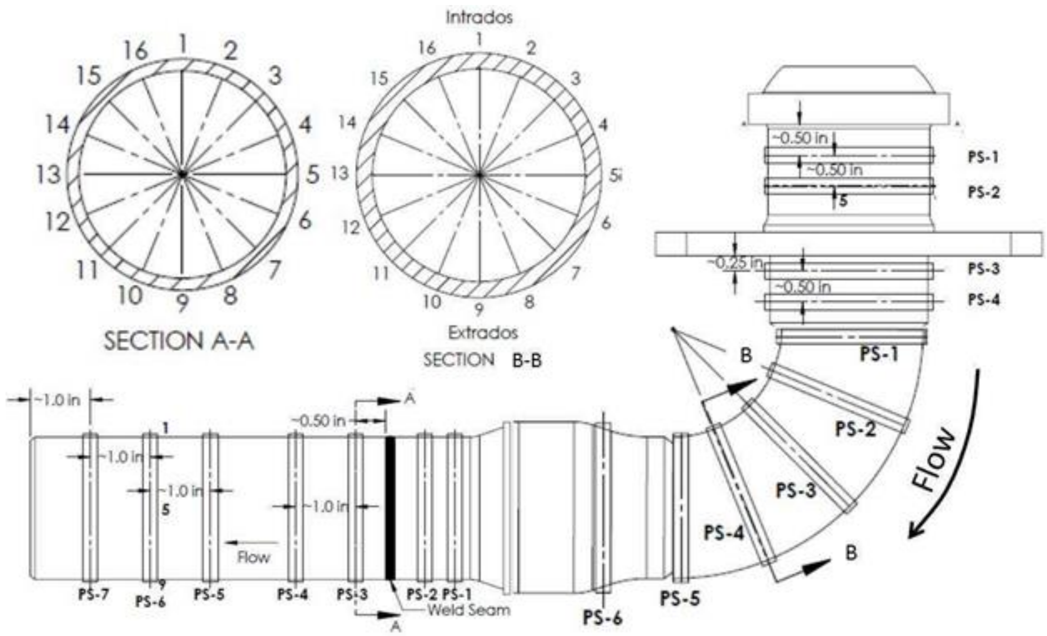

Figure 93. POR104 Nozzle B CAD drawing.

Thickness measurements for each nozzle were taken with an ultrasonic transducer (Manufacturer: Krautkramer, Model: USN-52L) around the outside diameter of the pipe at the straight sections, elbows, and Purex nozzles. The ultrasonic transducer thickness measurements are plotted and trends are assessed based on the volume of fluid transferred.

Elbow-B (90 degree long radius bend)

A 3D CAD drawing of the floor nozzle with Elbow-B circled is provided in Figure 94. The figure also provides the positions at which measurements were taken. The grid was labeled 1 through 16 around the outer diameter of the pipe and PS-1 to PS-6 running horizontally along the length of the pipe. The sixteen measurements along the outer diameter were taken every 22.5° as shown in Section A-A of the figure. The results of the thickness measurements are shown in Table 12.

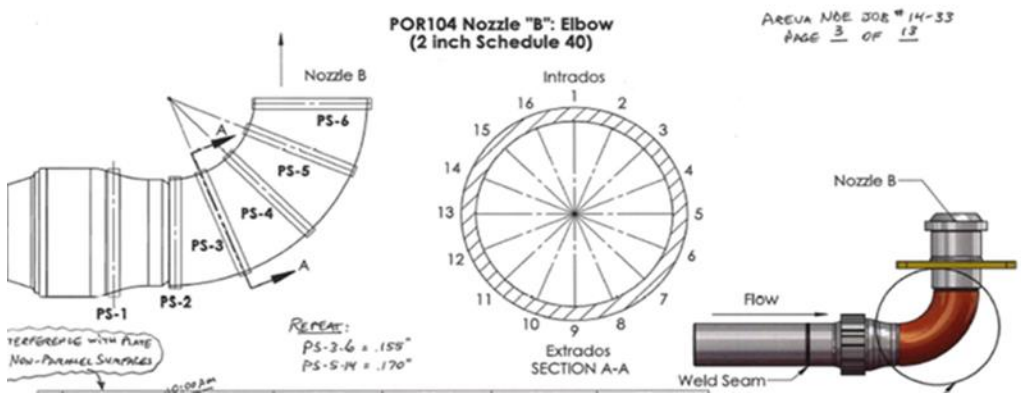

Figure 94. Position of UT Measurements around Elbow-B of POR104.

Table 12. UT Measurements for Elbow-B of POR104 (in)

Location	PS-1	PS-2	PS-3	PS-4	PS-5	PS-6
1	NR	NR	0.177	0.200	0.201	NR
2	NR	NR	0.181	0.199	0.196	NR
3	NR	NR	0.180	0.189	0.185	NR
4	NR	NR	0.177	0.173	0.169	NR
5	NR	NR	0.168	0.163	0.163	NR
6	NR	NR	0.155	0.156	0.160	NR
7	NR	0.163	0.153	0.153	0.159	0.175
8	NR	0.157	0.146	0.145	0.155	0.17
9	NR	0.154	0.142	0.139	0.151	0.172
10	NR	0.156	0.144	0.141	0.149	0.169
11	NR	0.160	0.148	0.147	0.157	0.168
12	NR	NR	0.155	0.157	0.160	NR
13	NR	NR	0.165	0.162	0.162	NR
14	NR	NR	0.170	0.168	0.170	NR
15	NR	NR	0.180	0.182	0.182	NR
16	NR	NR	0.178	0.193	0.199	NR

A summary of the wall thickness measurements and calculations for Elbow-B is shown in Table 13 which includes the average thickness and standard deviations. Nominal, maximum and minimum manufacturing thicknesses are not provided for elbows in current standards so the thicknesses for straight pipe sections are provided for comparison. These manufacturing thicknesses were obtained using information for 2-in Stainless Steel Schedule 40 pipes. Nominal and minimum thicknesses for straight pipe sections were obtained from ASTM A312/A312M-12 Table X1.1 [2]. The maximum manufacturing thickness for straight sections, however, was not provided in the tables and was determined following the guidelines from ASTM A53-1972a Paragraph 14.2[3]. This paragraph states that the outside diameter should not vary more than 1%

from the standard specified. For the 2-inch schedule 40 pipe, a manufacturing maximum thickness of 0.185 in is obtained.

Long radius bend elbows are typicallySome elbows are manufactured using a rotary draw bending technique in which a straight pipe section is bent over a rotating bending die. During this process, the thickness at the extrados of the pipe is reduced and the thickness at the intrados has a corresponding thickening [4]. Various standards provide guidelines for the percentage of thinning at the extrados from the nominal thickness of the straight section. ASME B31.1 Section 102.4.5 states that a minimum thickness prior to bending is 1.08 times the nominal thickness of the straight section (for a 5D bend radius elbow) [5]. The Piping Handbook provides guidelines for determining the thickness reduction of the extrados [6]. For this elbow, the reduction is 10.6% from the nominal thickness.

Table 13. Summary of Elbow for Nozzle B Thickness Measurements (in)

Overall Average Wall Thickness Measurements	0.169
Overall Standard Deviation	0.016
Average -2 Standard Deviation	0.137
Average +2 Standard Deviation	0.201
Manufacturer Nominal Thickness	0.154
Minimum Manufacturing Thickness	0.135
Maximum Manufacturing Thickness	0.185
Amount of Slurry Transferred	7.83M gal
Note: Nominal thickness based on Stainless Steel, 2" Diameter, Schedule 40	

To determine how the thickness varies along the circumference, the average longitudinal thickness measurements are plotted at each radial location (Figure 95). The average thickness, nominal thickness (straight section), and the manufacturing minimum and maximum thickness (straight section) are also plotted. Additionally, a compensated thickness is plotted to incorporate thinning at the extrados and provide a better understanding of the potential thinning due to erosion. This curve was created by adding 10% of the average thickness of Radial Positions 5 and 13 to the thickness at the extrados (Radial Position 9). Similarly, 7.5% of the average thickness of Positions 5 and 13 was added to Positions 8 and 10, 5% was added at Positions 7 and 11, and 2.5% was added at Positions 6 and 12. Radial Positions 5 and 13 are on the top and bottom of the pipe and should not have a change in thickness due to the bending process. Positions 1 and 9 are actually on the intrados and extrados of the pipe, respectively, so values have been subtracted to account for the corresponding thickening.

For this data set, the average thickness measurements show a decreasing trend as the radial position varies from 1 to 9. The minimum thickness occurs at Radial Position 9 and Radial Position 10 and the maximum thickness occurs at Radial Position 1. The difference between the maximum and minimum longitudinal averages is approximately 0.041 inch. The data for the compensated thickness shows a decrease from the intrados to the extrados and an increase from the extrados back to the intrados.

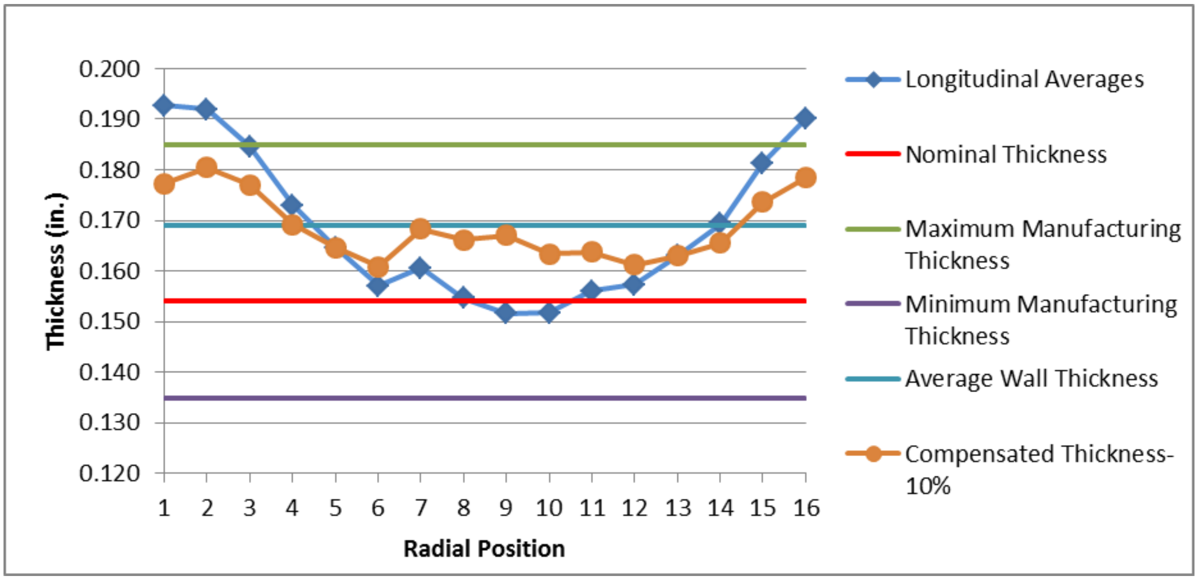

Figure 95. Floor Nozzle B longitudinal average measurements grouped by radial position (Elbow-B).

The average radial measurements are plotted at each longitudinal position to determine how the thickness in the pipe varies along the longitudinal position (Figure 96). The average thickness, nominal thickness, and the manufacturing minimum and maximum thicknesses (for straight sections) are also plotted. The average radial measurements along the longitude of the pipe slightly increase from Positions PS-2 to PS-6. This difference is likely due to the manufacturing process although flow through the elbow could cause more erosion at PS-2 and less at PS-6 due to the flow impinging on the outer wall.

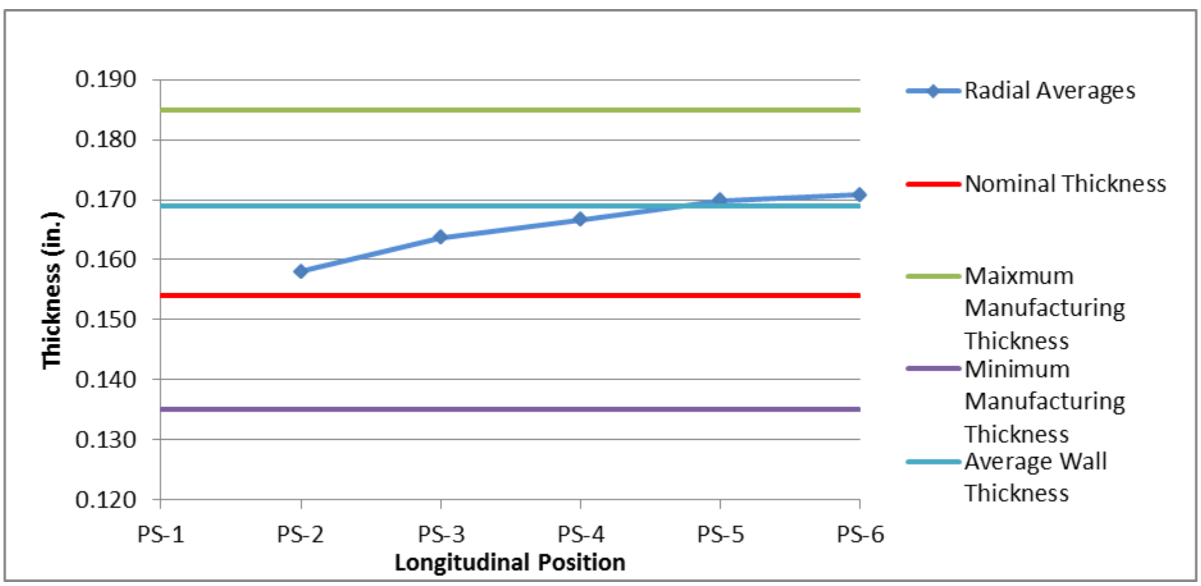

Figure 96. Floor Nozzle B radial average measurements grouped by longitudinal position (Elbow-B).

These graphs demonstrate that the average wall thickness is greater than the nominal wall thickness. This suggests that the initial thickness of Elbow-B was greater than the nominal thickness. Unfortunately, there is no record of the original thickness prior to installation and the only baseline for comparison of these thickness measurements is the nominal thickness of a 2-in Stainless Steel Schedule 40 pipe. Thus, there is no detectable wear in this component and a life expectancy analysis based on the manufacturing nominal wall thickness and present wall thickness is not practical.

Straight-B

A 3D CAD drawing of the floor nozzle with Straight-B circled is provided in Figure 97. The figure also provides the positions at which measurements were taken. The grid was labeled 1 through 16 around the outer diameter of the pipe and PS-1 to PS-7 running horizontally along the length of the pipe. The sixteen measurements along the outer diameter were taken every 22.5° as shown in Section A-A of the figure. The results of the thickness measurements are shown in Table 14.

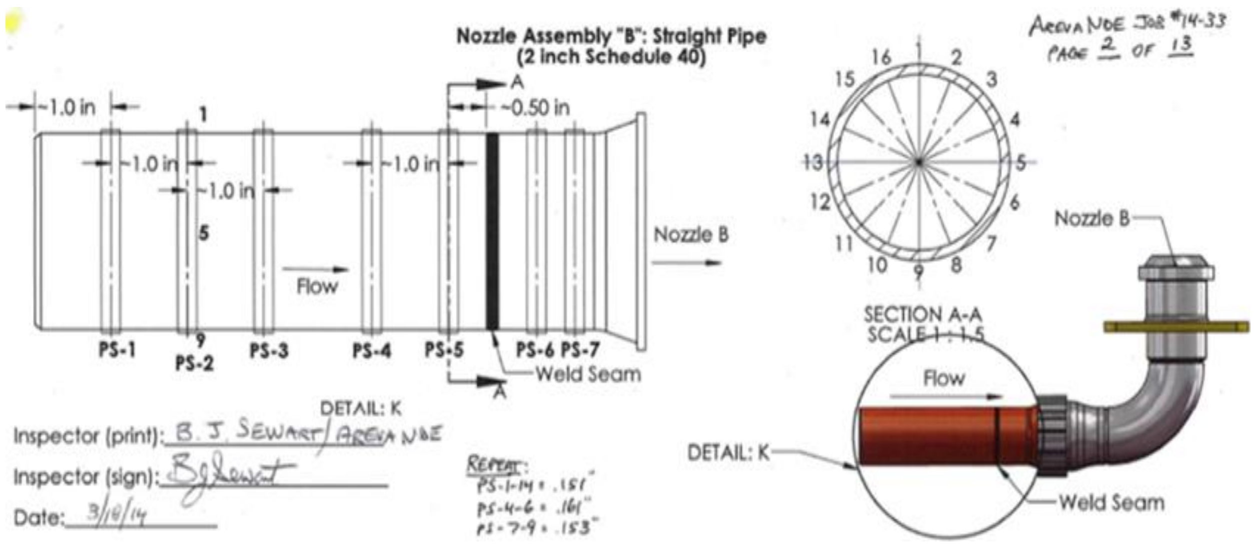

Figure 97. Position of UT Measurements around Straight-B of POR104.

Table 14. UT Measurements for Straight-B of POR104 (in)

Location	PS-1	PS-2	PS-3	PS-4	PS-5	PS-6	PS-7
1	0.145	0.142	0.146	0.142	0.147	0.166	0.161
2	0.144	0.146	0.145	0.141	0.145	0.160	0.159
3	0.148	0.148	0.148	0.147	0.146	0.156	0.156
4	0.151	0.152	0.151	0.151	0.152	0.154	0.154
5	0.154	0.156	0.154	0.155	0.153	0.150	0.154
6	0.165	0.162	0.160	0.162	0.165	0.149	0.149
7	0.165	0.165	0.163	0.166	0.170	0.151	0.150
8	0.165	0.166	0.170	0.169	0.169	0.152	0.155
9	0.165	0.167	0.167	0.166	0.168	0.169	0.155
10	0.165	0.165	0.169	0.165	0.165	0.175	0.163
11	0.163	0.163	0.165	0.163	0.163	0.158	0.158
12	0.158	0.159	0.160	0.159	0.159	0.157	0.159

13	0.154	0.156	0.156	0.156	0.154	0.159	0.163
14	0.152	0.151	0.153	0.153	0.149	0.162	0.161
15	0.146	0.147	0.147	0.149	0.147	0.162	0.161
16	0.143	0.145	0.143	0.144	0.145	0.163	0.163

A summary of the wall thickness measurements and calculations for Straight-B is shown in Table 15. The average and standard deviations were calculated and the nominal, maximum and minimum manufacturing thicknesses are listed. The manufacturing thicknesses obtained were based on 2-in Stainless Steel Schedule 40 pipes. Nominal and minimum thicknesses for straight pipe sections were obtained from ASTM A312/A312M-12 Table X1.1 [2]. The maximum manufacturing thickness for straight sections, however, was not provided in the tables and was determined following the guidelines from ASTM A53-1972a Paragraph 14.2[3]. This paragraph states that the outside diameter should not vary more than 1% from the standard specified. For the 2-inch schedule 40 pipe, a manufacturing maximum thickness of 0.185 in is obtained.

Table 15. Summary of Straight Section for Nozzle B Thickness Measurements

Overall Average Wall Thickness Measurements	0.156
Overall Standard Deviation	0.008
Average -2 Standard Deviation	0.140
Average +2 Standard Deviation	0.173
Manufacturer Nominal Thickness	0.154
Minimum Manufacturing Thickness	0.135
Maximum Manufacturing Thickness	0.185
Amount of Slurry Transferred	7.83M gal
Note: Nominal thickness based on Stainless Steel, 2" Diameter, Schedule 40	

To determine how the thickness varies along the circumference, the average longitudinal thickness measurements are plotted at each radial location (Figure 98). The average thickness, nominal thickness, and the manufacturing minimum and maximum thicknesses are also plotted. For this data set, the average thickness measurements show an oscillatory trend rotating clockwise around the circumference. The minimum thickness is found at location 2 and the maximum thickness is found to be at location 10. The difference between the maximum and minimum longitudinal averages is 0.028 inches and is likely due to the manufacturing process and not erosion.

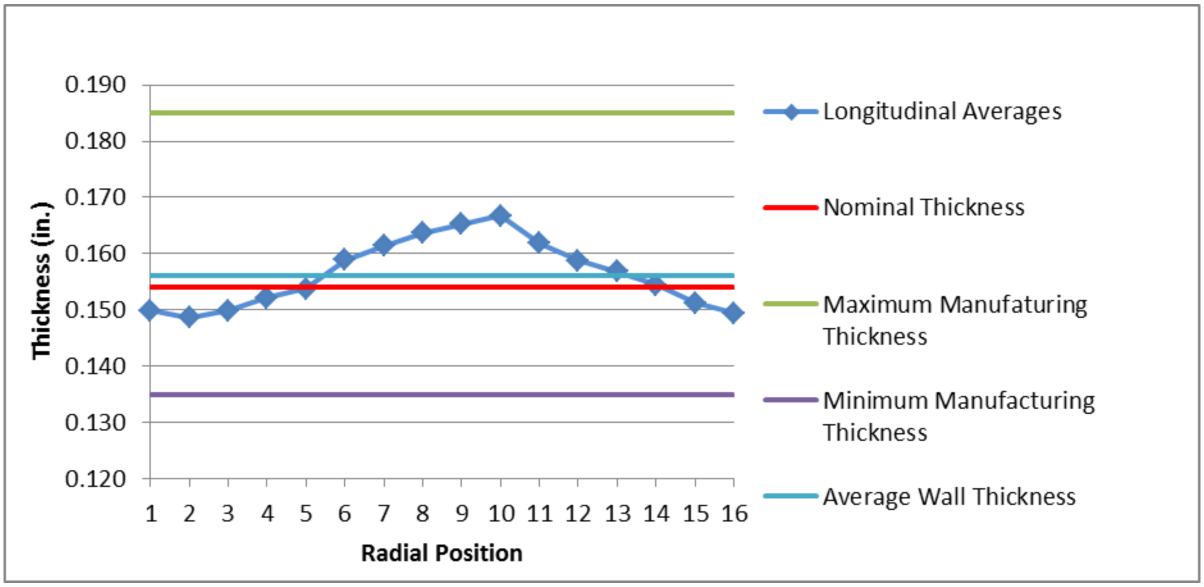

Figure 98. Floor Nozzle B longitudinal average measurements grouped by radial position (Straight-B).

The average radial measurements are plotted at each longitudinal position to determine how the thickness in the pipe varies along the longitudinal position (Figure 99). The average thickness, nominal thickness, and the manufacturing minimum and maximum thicknesses are also plotted. The average radial measurements along the longitude of the pipe are consistent except for a slight increase at Position PS-6. This difference is likely due to the manufacturing process although flow through the elbow could cause more erosion at PS-6 due to the flow impinging on the outer wall as a result of it being the first position after the weld seam.

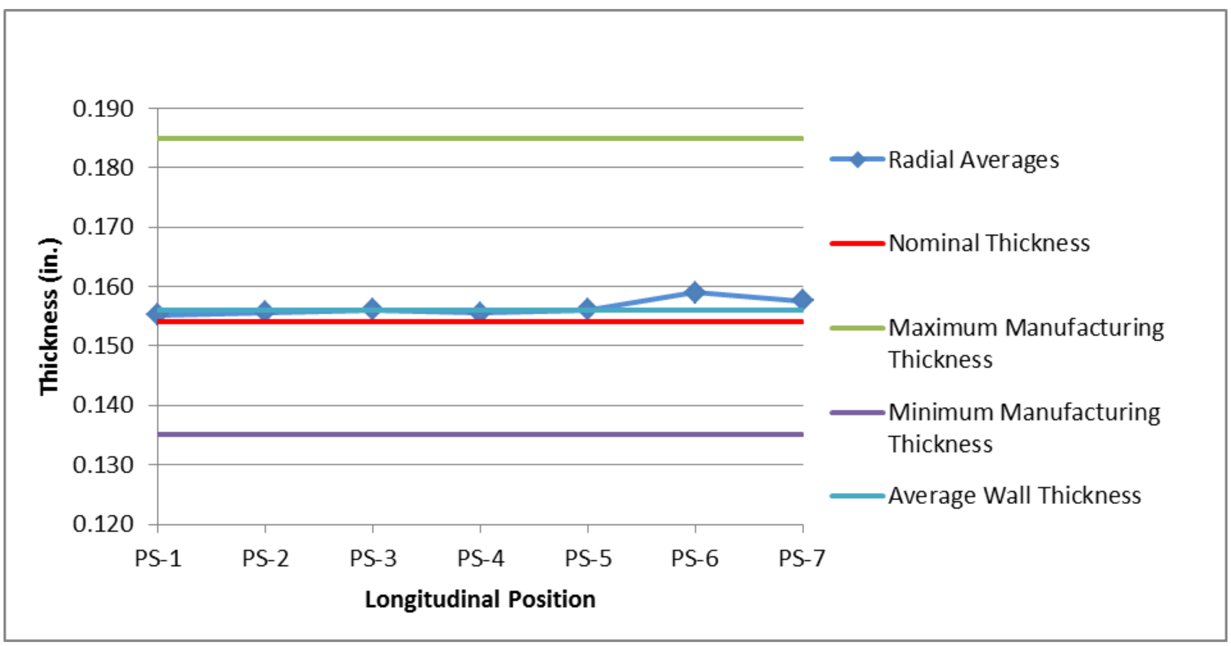

Figure 99. Floor Nozzle B radial average measurements grouped by longitudinal position (Straight-B).

These graphs demonstrate that the average wall thickness is greater than the nominal wall thickness. This suggests that the initial thickness of Straight-B was greater than the nominal thickness. Unfortunately, there is no record of the original thickness prior to installation and the only baseline for comparison of these thickness measurements is the nominal thickness of a 2-in Stainless Steel Schedule 40 pipe. Thus, there is no detectable wear in this component and a life expectancy analysis based on the manufacturing nominal wall thickness and present wall thickness is not practical.

Purex Nozzle-B

A 3D CAD drawing of the floor nozzle with Purex Nozzle-B circled is provided in Figure 100. The figure also provides the positions at which measurements were taken. The grid was labeled 1 through 16 around the outer diameter of the pipe and PS-1 to PS-4 running horizontally along the length of the Purex Nozzle. The sixteen measurements along the outer diameter were taken every 22.5° as shown in Section A-A of the figure. An extra radial position (17) was added *in situ*. The results of the thickness measurements below the kick plate are shown in Table 16.

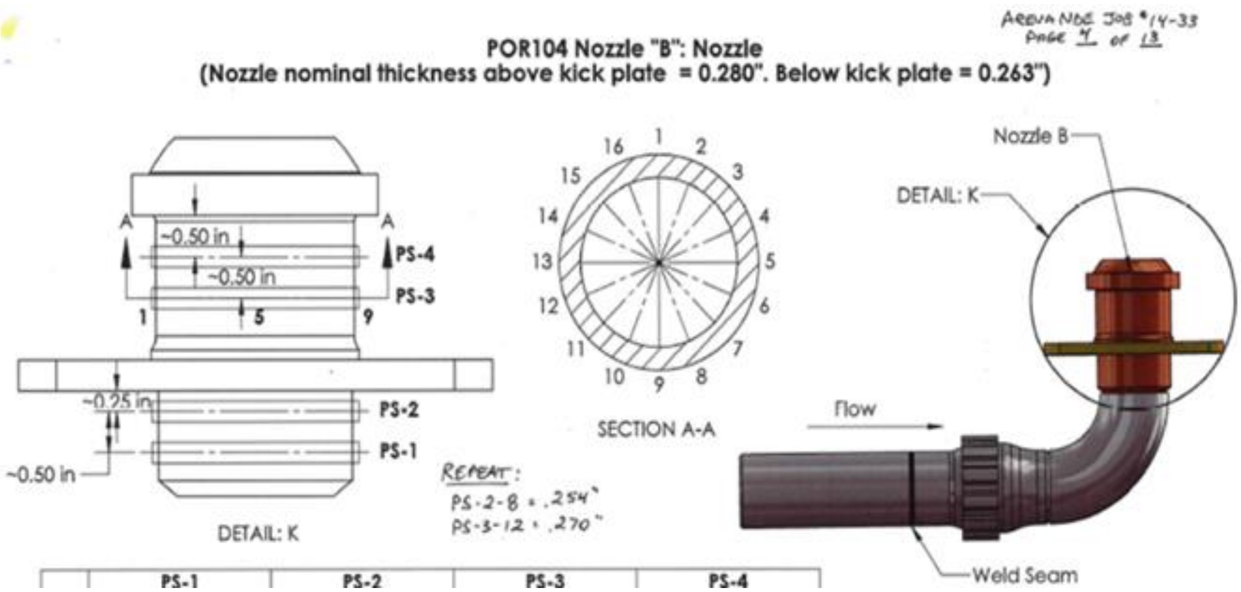

Figure 100. Position of UT Measurements around Purex Nozzle-B of POR104.

Purex Nozzle-B (Below Kick Plate)

Table 16. UT Measurements for Purex Nozzle-B of POR104 below the Kick Plate (in)

Location	PS-1	PS-2
1	0.257	0.268
2	0.254	NR
3	NR	NR
4	0.258	0.254
5	0.260	0.257
6	0.259	0.252
7	0.269	0.259
8	0.258	0.254
9	0.257	0.253
10	0.260	0.248
11	0.254	NR
12	0.253	NR
13	0.269	NR
14	0.275	0.280
15	0.263	0.267
16	0.263	0.267
17	0.265	0.268

A summary of the wall thickness measurements and calculations for Purex Nozzle-B below the kick plate is shown in Table 17. The average and standard deviations were calculated and the nominal, maximum and minimum manufacturing thicknesses are listed. The manufacturing thicknesses obtained were based on 2-in Stainless Steel Schedule 40 pipes. The Purex nozzle was a cast stainless steel (ASTM A995 Grade 1B), machined to 0.263 in below the kick plate. Maximum and minimum manufacturing thicknesses were obtained from drawings provided by site engineers.

Table 17. Summary of Purex Nozzle for Nozzle B Thickness Measurements (Below Kick Plate)

Overall Average Wall Thickness Measurements	0.260
Overall Standard Deviation	0.008
Average -2 Standard Deviation	0.245
Average +2 Standard Deviation	0.275
Manufacturer Nominal Thickness	0.263
Minimum Manufacturing Thickness	0.2275
Maximum Manufacturing Thickness	0.2975
Amount of Slurry Transferred	7.83M gal
Note: Nominal thickness base on Stainless Steel, 2" Diameter, Schedule 40	

To determine how the thickness varies along the circumference, the average longitudinal thickness measurements are plotted at each radial location (Figure 101). The average thickness, nominal thickness, and the manufacturing minimum and maximum thicknesses are also plotted. For this data set, the average thickness measurements were fairly constant until radial position 13, where a slight increase is observed. The minimum thickness is found at location 12 and the maximum thickness is found to be at location 14. The difference between the maximum and minimum longitudinal averages is 0.025 inches and is likely due to the manufacturing process and not erosion.

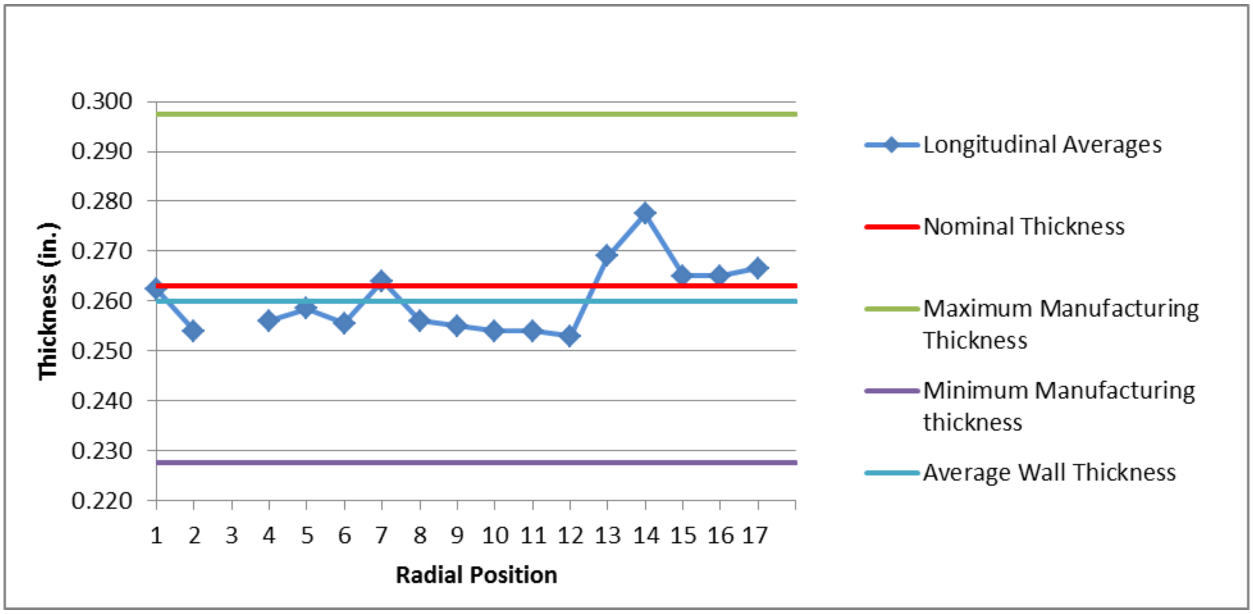

Figure 101. Floor Nozzle B longitudinal average measurements grouped by radial position (Purex Nozzle-B, below kick plate).

The average radial measurements are plotted at each longitudinal position to determine how the thickness in the pipe varies along the longitudinal position (Figure 102). The average thickness, nominal thickness, and the manufacturing minimum and maximum thicknesses are also plotted. The average radial measurements along the longitude of the pipe show a very slight decrease from position PS-1 to position PS-2.

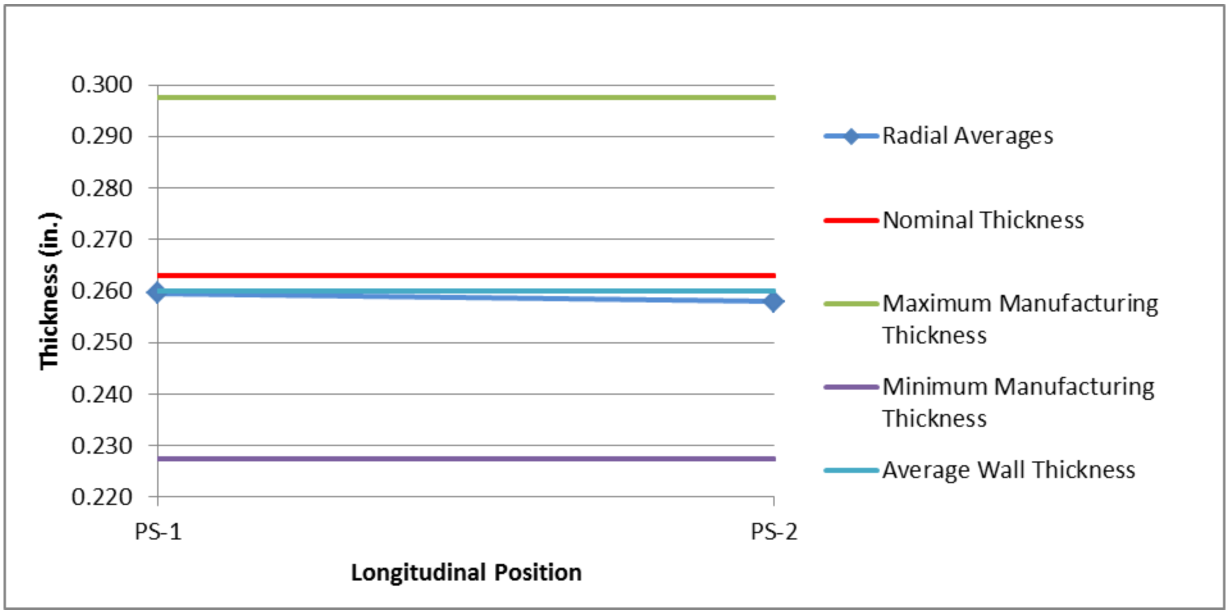

Figure 102. Floor Nozzle B radial average measurements grouped by longitudinal position (Purex Nozzle-B, below kick plate).

These graphs demonstrate that the average wall thickness is just slightly less than the nominal wall thickness. Unfortunately, there is no record of the original thickness prior to installation and the only baseline for comparison of these thickness measurements is the nominal thickness of a 2-in Stainless Steel Schedule 40 Purex Nozzle. Based on the volume of fluid transferred and the 0.003 in difference in the average and nominal thickness, the wear rate is negligible. The component's remaining useful life would easily extends past the life needed for WTP.

Purex Nozzle-B (Above Kick Plate)

Thickness measurements were also taken above the kick plate at two longitudinal positions and 17 radial positions. Results are provided in Table 18.

Table 18. UT Measurements for Purex Nozzle B of POR104 above the Kick Plate

Location	PS-3	PS-4
1	0.276	0.278
2	0.270	0.285
3	0.284	0.268
4	0.276	0.285
5	0.261	0.27
6	0.269	0.275
7	0.273	0.276
8	0.274	0.273
9	0.286	0.278
10	0.293	0.289
11	0.268	0.281
12	0.271	0.273
13	0.272	0.273
14	0.263	0.273
15	0.270	0.267
16	0.271	0.266
17	0.268	0.267

A summary of the wall thickness measurements and calculations for Purex Nozzle-B above the kick plate is shown in Table 19. The average and standard deviations were calculated and the nominal, maximum and minimum manufacturing thicknesses are listed. The Purex nozzle was a cast stainless steel (ASTM A995 Grade 1B), machined to 0.280 in above the kick plate. Maximum and minimum manufacturing thicknesses were obtained from drawings provided by site engineers.

Table 19. Summary of Purex Nozzle for Nozzle B Thickness Measurements (Above Kick Plate)

Overall Average Wall Thickness Measurements	0.275
Overall Standard Deviation	0.007
Average -2 Standard Deviation	0.261
Average +2 Standard Deviation	0.290
Manufacturer Nominal Thickness	0.280
Minimum Manufacturing Thickness	0.240
Maximum Manufacturing Thickness	0.320
Amount of Slurry Transferred	7.83M gal
Note: Nominal thickness base on Stainless Steel, 2" Diameter, Schedule 40	

To determine how the thickness varies along the circumference, the average longitudinal thickness measurements are plotted at each radial location (Figure 103). The average thickness, nominal thickness, and the manufacturing minimum and maximum thicknesses are also plotted. For this data set, the average thickness measurements are fairly constant with a slight peak at position 10 near the bottom. The minimum thickness is found at location 5 and the maximum thickness is found to be at location 10. The difference between the maximum and minimum longitudinal averages is 0.025 inches and does not appear to be due to erosion.

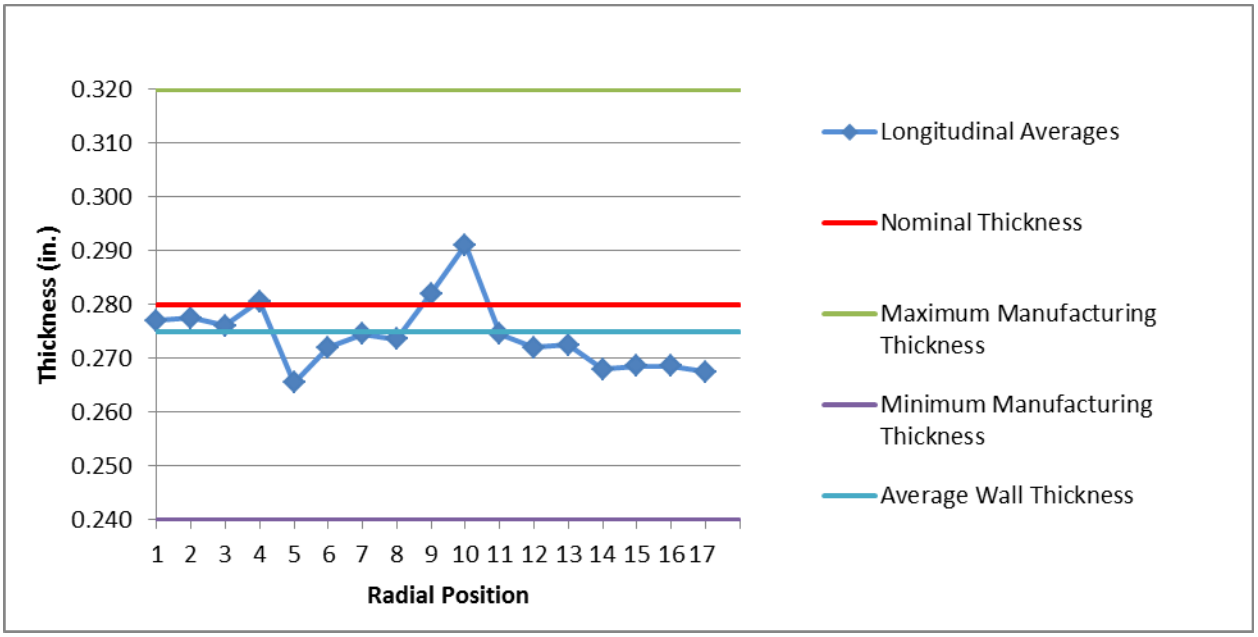

Figure 103. Floor Nozzle B longitudinal average measurements grouped by radial position (Purex Nozzle-B, above kick plate).

The average radial measurements are plotted at each longitudinal position to determine how the thickness in the pipe varies along the longitudinal position (Figure 104). The average thickness, nominal thickness, and the manufacturing minimum and maximum thicknesses are also plotted. The average radial measurements along the longitude of the pipe are fairly consistent, with a slight increase from position PS-3 to position PS-4.

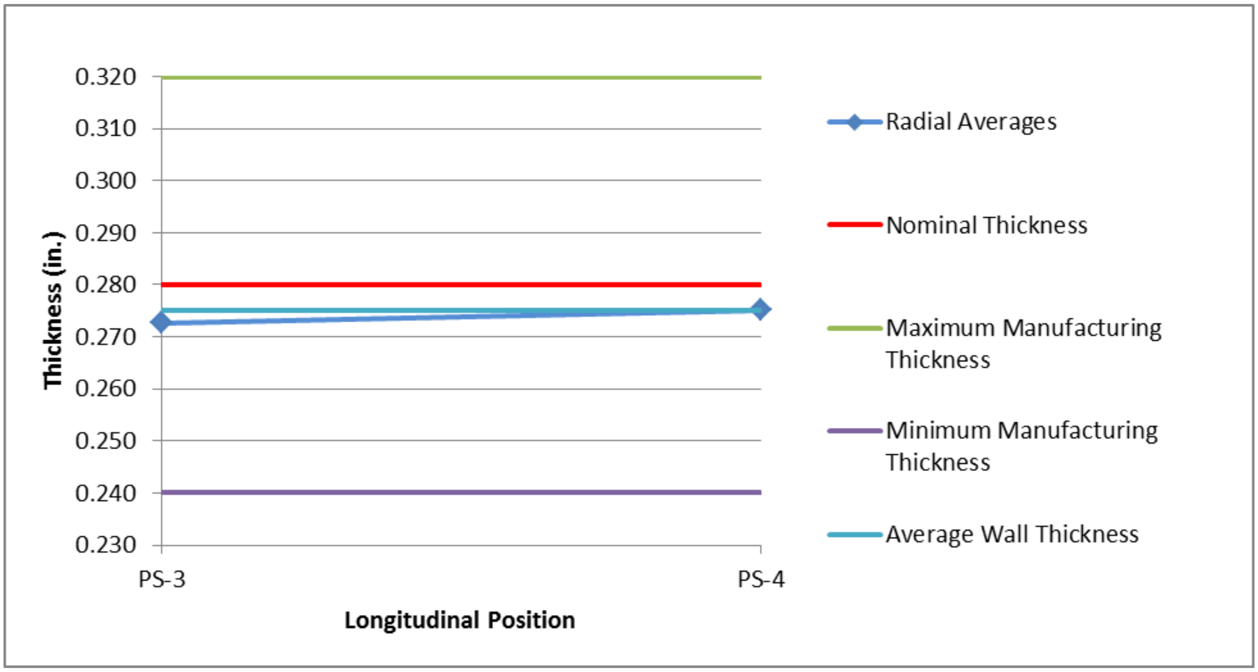

Figure 104. Floor Nozzle B radial average measurements grouped by longitudinal position (Purex Nozzle-B, above kick plate).

These graphs demonstrate that the average wall thickness is just slightly less than the nominal wall thickness. Unfortunately, there is no record of the original thickness prior to installation and the only baseline for comparison of these thickness measurements is the nominal thickness of a 2-in Stainless Steel Schedule 40 Purex Nozzle. Based on the volume of fluid transferred and the 0.005 in difference in the average and nominal thickness, the wear rate is negligible. The component's remaining useful life would easily extends past the life needed for WTP.

Overall Analysis for Nozzle B

Floor Nozzle B is a 2-in Schedule 40 ASTM A312 TP 304L stainless steel pipe located in the C-Tank Farm. From 2004 to 2011, it transferred approximately 7.83 Mgal of slurry. As part of the Tank Farms Waste Transfer System Fitness-for-Service Program, three sections of the floor nozzle have been evaluated via ultrasonic thickness measurements. These sections include Elbow-B, Straight-B and Purex Nozzle-B. Table 20 provides a summary of the average thicknesses measured for each section and the nominal and minimum manufacturing thickness. For the elbow and straight section, the average thickness was greater than the minimum thickness; however, for one of the kick plate, the average thickness was slightly less than the nominal thickness. There was no significant wear trend based on radial thickness averages for the straight sections. Radial thickness averages for the elbow were similar to other jumper elbows with a minor decrease at the edge. Additionally, the differences between the maximum and minimum thickness values were minimal, suggesting that any thicknesses below nominal values are due to variations from manufacturing.

Table 20. Thicknesses Summary for Each Section of Nozzle B

Section	Average Thickness (in)	Manufacturer's Nominal Thickness (in)	Minimum Manufacturing Thickness (in)
Elbow-B	0.169	0.154	0.135
Straight-B	0.156	0.154	0.135
Purex Nozzle-B (Below)	0.260	0.263	0.2275
Purex Nozzle-B (Above)	0.275	0.280	0.240

Summary for Nozzle C

Nozzle C of the POR104 valve box was fabricated with a 2" schedule 40 pipe made of ASTM A312 TP 304L stainless steel. It was installed in 2004 and transferred approximately 7.27 million gallons of supernatant waste. The nozzles served as connection points between the C-Tank Farm hose-in-hose transfer lines and the valve manifolds which allowed the routing of single-shell tank (SST) waste to the recipient double-shell tank (DST) 241-AN-106. A CAD illustration of the jumper is provided in Figure 105.

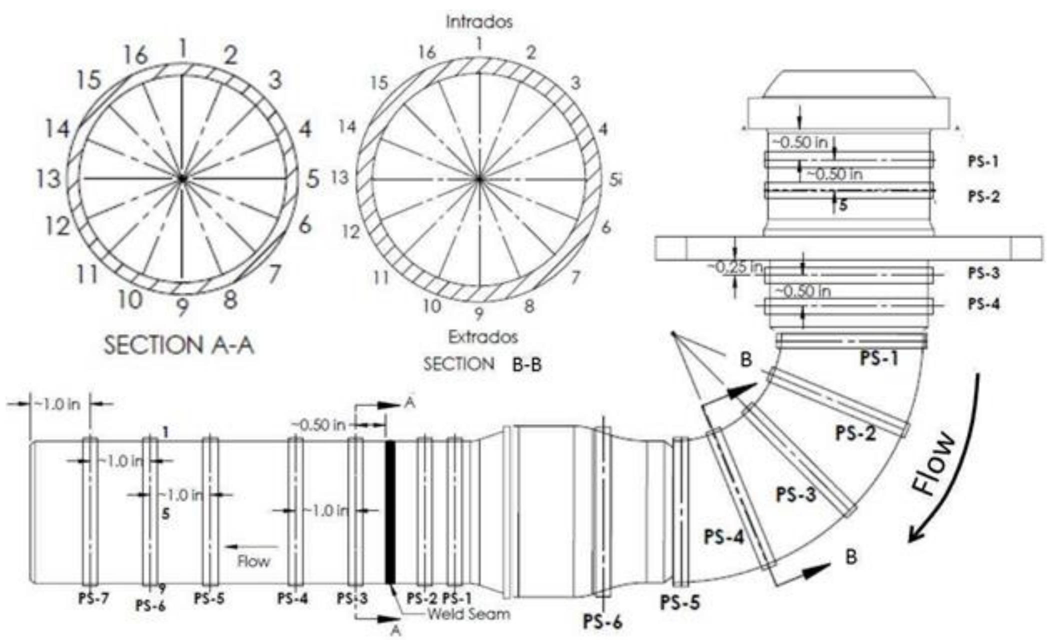

Figure 105. POR104 Nozzle C CAD drawing.

Table 21 provides a summary of the average thicknesses measured for each section and the nominal and minimum manufacturing thickness. In all cases, the average thickness was greater than the minimum thickness; however, for one of the three sections, the average thickness was less than the nominal thickness. For the elbow and straight section, the average thickness was greater than the minimum thickness; however, for one of the kick plate, the average thickness was slightly less than the nominal thickness. There was no significant wear trend based on radial thickness averages for the straight sections. Additionally, the differences between the maximum and minimum thickness values were minimal, suggesting that any thicknesses below nominal values are due to variations from manufacturing.

Table 21. Thicknesses Summary for Each Section of Nozzle C

Section	Average Thickness (in)	Manufacturer's Nominal Thickness (in)	Minimum Manufacturing Thickness (in)
Elbow-C	0.163	0.154	0.135
Straight-C	0.157	0.154	0.135
Purex Nozzle-C (Below)	0.261	0.263	0.2275
Purex Nozzle-C (Above)	0.271	0.280	0.240

Summary for Nozzle E

Nozzle E of the POR104 valve box was fabricated with a 2” schedule 40 pipe made of ASTM A312 TP 304L stainless steel. It was installed in 2004 and transferred approximately 7.83 million gallons of slurry waste. The nozzles served as connection points between the C-Tank Farm hose-in-hose transfer lines and the valve manifolds which allowed the routing of single-shell tank (SST) waste to the recipient double-shell tank (DST) 241-AN-106. A CAD illustration of the jumper is provided in Figure 106.

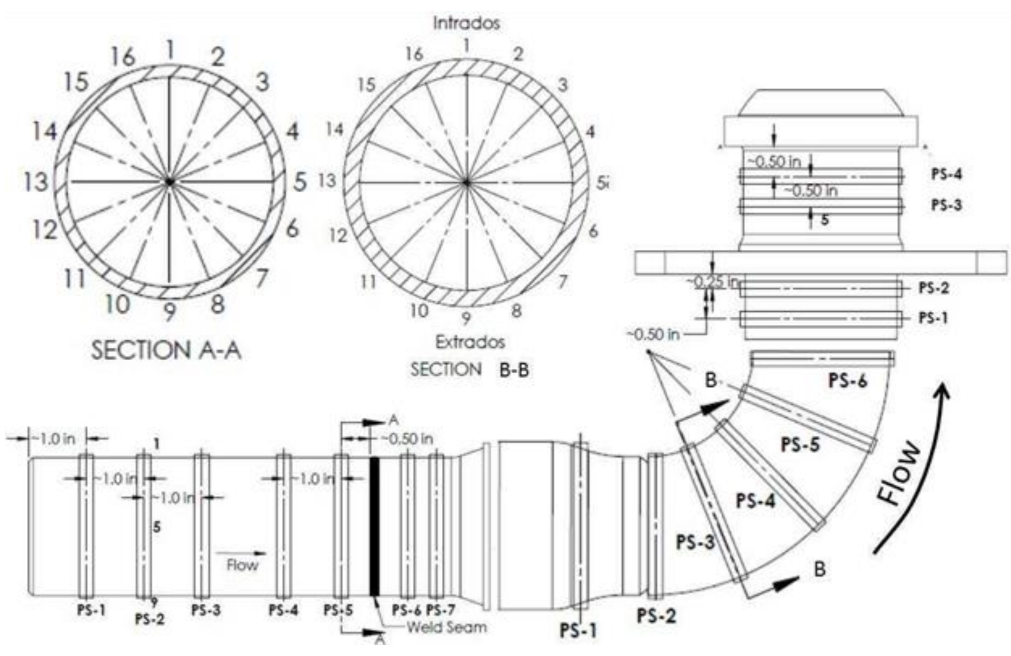

Figure 106. POR104 Nozzle E CAD drawing.

Table 22 provides a summary of the average thicknesses measured for each section and the nominal and minimum manufacturing thickness. In all cases, the average thickness was greater than the minimum thickness; however, for one of the three sections, the average thickness was less than the nominal thickness. For the elbow and straight section, the average thickness was greater than the minimum thickness; however, for one of the kick plate, the average thickness was slightly less than the nominal thickness. There was no significant wear trend based on radial thickness averages for the straight sections. Additionally, the differences between the maximum and minimum thickness values were minimal, suggesting that any thicknesses below nominal values are due to variations from manufacturing.

Table 22. Thicknesses Summary for Each Section of Nozzle E

Section	Average Thickness (in)	Manufacturer's Nominal Thickness (in)	Minimum Manufacturing Thickness (in)
Elbow-E	0.165	0.154	0.135
Straight-E	0.159	0.154	0.135
Purex Nozzle-E (Below)	0.262	0.263	0.2275
Purex Nozzle-E (Above)	0.278	0.280	0.240

Summary for Nozzle F

Nozzle F of the POR104 valve box was fabricated with a 2” schedule 40 pipe made of ASTM A312 TP 304L stainless steel. It was installed in 2004 and transferred approximately 7.27 million gallons of supernatant waste. The nozzles served as connection points between the C-Tank Farm hose-in-hose transfer lines and the valve manifolds which allowed the routing of single-shell tank (SST) waste to the recipient double-shell tank (DST) 241-AN-106. A CAD illustration of the jumper is provided in Figure 107 .

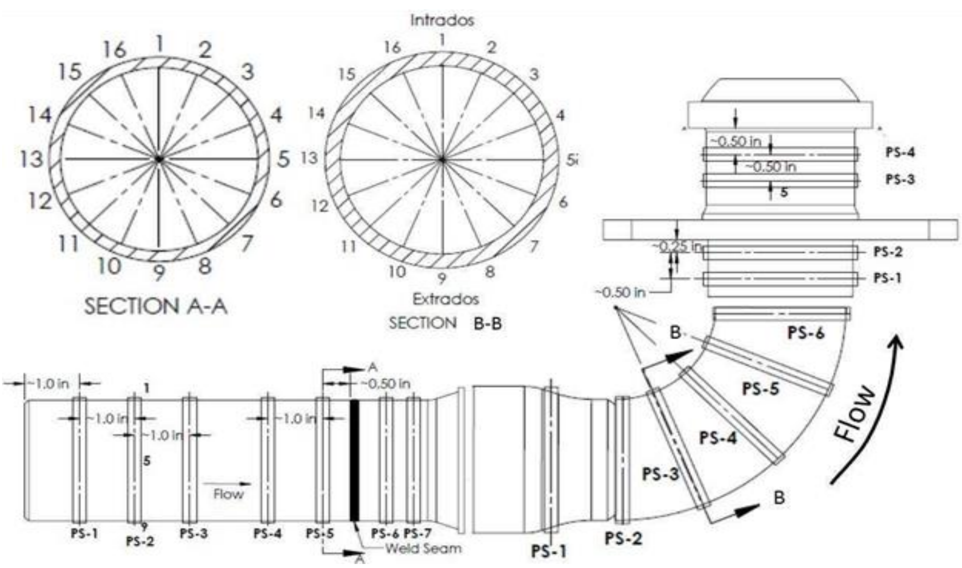

Figure 107. POR104 Nozzle F CAD drawing.

Table 23 provides a summary of the average thicknesses measured for each section and the nominal and minimum manufacturing thickness. In all cases, the average thickness was greater than the minimum thickness; however, for one of the three sections, the average thickness was less than the nominal thickness. For the elbow and straight section, the average thickness was greater than the minimum thickness; however, for one of the kick plate, the average thickness was slightly less than the nominal thickness. There was no significant wear trend based on radial thickness averages for the straight sections. Additionally, the differences between the maximum and minimum thickness values were minimal, suggesting that any thicknesses below nominal values are due to variations from manufacturing.

Table 23. Thicknesses Summary for Each Section of Nozzle F

Section	Average Thickness (in)	Manufacturer's Nominal Thickness (in)	Minimum Manufacturing Thickness (in)
Elbow-F	0.168	0.154	0.135
Straight-F	0.160	0.154	0.135
Purex Nozzle-F (Below)	0.259	0.263	0.2275
Purex Nozzle-F (Above)	0.277	0.280	0.240

SENSOR EVALUATION

After efforts by WRPS to obtain real time thickness measurements using a pipe wrap system were found to be difficult [7], FIU began investigating alternative approaches to obtaining the thickness measurements. Some of the operating parameters for the sensors have been loosely defined, however, the sensors would need to be able to take measurements via permanent mounting and be installed in confined spaces. To this end, FIU began investigating a variety of ultrasonic sensors and their couplants for measuring the thickness of 2- and 3-in diameter pipes. A majority of the companies that carry relevant transducers did not have products that met the site needs. In particular, most sensors evaluated required the use of a liquid couplant. For our application of long-term real-time measurements, a dry couplant is more practical.

After discussions with WRPS engineers and a number of vendors, FIU decided to purchase an Olympus 45MG Digital Ultrasonic Thickness Gage. The system is a dual crystal transducer that comes with a two-step reference block and a liquid couplant sample. Representatives of Olympus did not recommend the unit with dry couplant; however, a dry couplant was purchased for evaluation. Figure 108 shows the system being tested on a long radius, a short radius and Victaulic elbows. Preliminary measurements indicate that the liquid couplant provides accurate readings and errors are obtained with the dry couplant.

Figure 108. Ultrasonic sensor measurements of various elbows.

Dry couplant for the sensor – Market survey and initial experiments

Based on the recommendations from WRPS, the ultrasonic properties of new materials were investigated for potential use as dry couplants. A brief literature review along with a market survey was made and it is concluded that polymers and rubbers show promising options. Among the polymers, different hydrophilic polymers (water based polymers) are currently being investigated. These are a unique group of plastic materials characterized by compatibility with water. Water acts as a plasticizer and after swelling, they transform from a glass state to a high-elastic rubber like state. They exhibit high elasticity and flexibility and hence are suitable for complex geometries and surface roughness avoiding the air gaps in UT measurements. Swelling with water increases their acoustic properties to closely match with those of water and hence are suitable for high frequency ranges. These polymers with equilibrium water content ranging from 10% to 98 % by wet weight have been investigated for ultrasonic applications at frequencies ranging from 1MHz to 25 MHz. The potential hydrophilic polymers to be considered are: polyhydroxy ethyl methacrylate with 38% of water content, copolymer of N-vinyl pyrolidone and 2-hydroxy ethyl methacrylate with 42%of water content, poly hydroxyl ethyl methacrylate with 49% of water content, terpolymer based on glyceraol methacrylate with 59% of water content and copoplymer of N-vinyl pyrrolidone and methyl methacrylate with 75% of water content.

An elastomer couplant (in the form of aqualene) was tested as the first polymer-based dry couplant. Aqualene was purchased by FIU from Olympus. Various measurements were made on carbon steel and cast iron pipe elbows and a reducer section using the Olympus UT sensor (45MG digital ultrasonic thickness gauge – D790 SM). Both the liquid gel couplant and dry couplant were used and the readings were compared. Sample results are as tabulated in Table 24. The readings obtained from the gel were accurate whereas those obtained using the dry couplant had discrepancies. As shown in the table, the percentage error varied from 18.2 % to a maximum of 44.8%. Possible reasons could be the geometry, acoustic property mismatch, low signal attenuation through the material, air gaps and/or the pressure exerted on the sensor.

Table 24. Results of Thickness Measurements using UT Sensors and Couplants

	Gel Couplant (Glycerin)		Dry Couplant (Aqualene)		Error (%) (Aqualene)	
	Top	Extrodus	Top	Extrodus	Top	Extrodus
90° Elbow (carbon steel)	0.239	0.210	0.312	0.310	30.5	44.8
90° Elbow (cast iron)	0.265	0.250	0.320	0.320	20.8	26.4
	Diameter (Smaller)	Diameter (larger)	Diameter (Smaller)	Diameter (larger)	Diameter (Smaller)	Diameter (larger)
Reducer (carbon steel)	0.235	0.275	0.301	0.325	28.1	18.2

In addition to polymers, rubbers are potential materials to be used as dry couplants. A few options include nitrile rubber, polyisoprene rubber, and polymethyl methacrylate (PMMA) based rubbers. Of these, nitrile rubber material was investigated as a potential dry couplant. A sample thin sheet of nitrile rubber was used as a dry couplant to measure the thickness of a carbon steel pipe section of nominal diameter 3” and average thickness of 0.19”. It was observed that by using the nitrile rubber material alone, no signal was captured by the sensor, but the nitrile sheet along with the gel couplant (glycerene) provided by the manufacturer gave an exact reading. Also, as a next option, the nitrile rubber sheet was placed on top of the acqualene dry couplant and the combination was used to measure the thickness. In this case, a reading was observed but with an approximate error of 20%. It was concluded that nitrile rubber alone is not a feasible option but has potential when combined with acqualene since it does not interfere with the signals. We are currently further investigating this option.

Dry couplant for the sensor – Vacuum sealing technique

Vacuum sealing was investigated as a possible method for sealing dry couplants to avoid the air gap between the couplant and the test piece. Initial vacuum tests were conducted using a vacuum bag and also using a nitrile bag. The experimental set up for the vacuum sealing test conducted using a nitrile bag is shown in Figure 109. As seen in the figure, a sample of dry couplant - acqualene was placed on the test piece and air was pulled using a vinyl pipette tip and a tube combination. The UT sensor was placed on top of the set up and readings were taken. It was observed that the thickness readings did not have much influence from the vacuum sealing.

Figure 109. Vacuum bag sealing using a nitrile bag.

Initial vacuum tests were followed by standardized procedures. A vacuum bag and a sealant were used and a thin acqualene sample (0.02”) was vacuum sealed on a straight carbon steel pipe section of nominal diameter 3” and average thickness 0.19”. The experimental test set up is shown in Figure 110. The UT sensor was placed above the aqualene sample and readings were taken. The readings were similar to the previous case.

Figure 110. Standard vacuum bag sealing

Dry couplant for the sensor – Pressure/load testing

Some experiments showed that the thickness readings for each test piece were affected by the amount of pressure applied on the sensor when using the dry couplant (aqualene). To further investigate this effect, dead weights (in the form of readily available PVC and metallic components) were placed on the sensor and readings were observed. A sample test case is shown in Figure 111. As seen in the figure, dead weights are placed on the sensor (no contact with the test piece). It has a 0.02” aqualene sheet below it. The actual thickness of the aluminum sheet to be measured is 0.25”. Different sets of weights were placed until a signal was received. It is observed that once a fixed amount of weight (0.8454 lbs) is placed on the sensor, a signal was obtained. Also, no further change in readings is observed with increasing weights. Hence, it is concluded that for a certain threshold weight, enough pressure is exerted on the aqualene to get a reading for thickness.

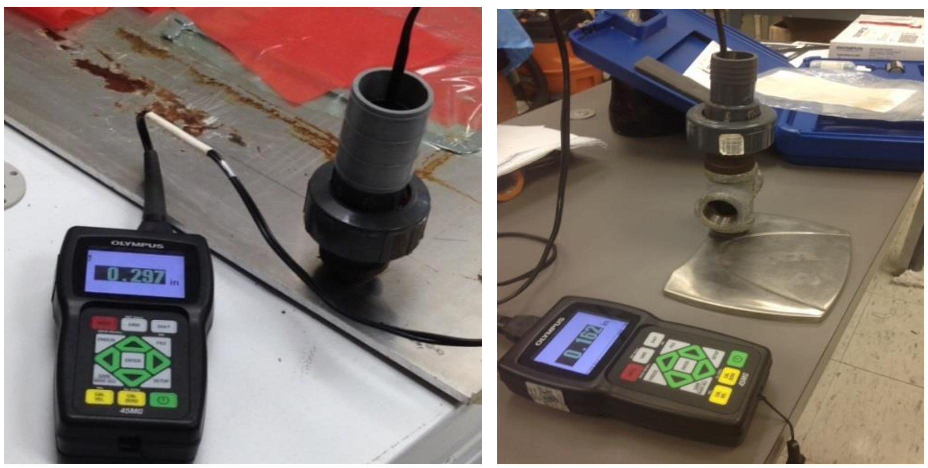

Figure 111. Experimental setup with loads on the sensor (aluminum (left) and stainless steel (right) test plates).

Also, it is observed that the amount of load/pressure required to obtain a reading (using aqualene), also depends on the type of the material. For this, a new sample made of carbon steel with a thickness of 0.25” was chosen. Similar to the previous case, dead weights were applied until a reading was observed. In this case, the threshold load for reading was 6.17 lbs.

A third test was based on the thickness of the material of the sample. A stainless steel sample with a thickness of 0.02” was taken as the test sample. Measurements were made by applying the weights to find the pressure required on the sensor. The test arrangement is shown in Figure 124(right). In this case, the threshold load for reading was 2.01 lbs. Also, based on the loads (weight), pressure (psi) exerted on the sensor was calculated using the cross section area (of contact) of the sensor.

A comparison of the reading for the sample cases is shown in Table 25. The thickness readings obtained in all the cases along with the corresponding percentage error is given in the same table. It is evident, that the readings are varying based on the type and thickness of the material. Hence, it is concluded that the readings with aqualene dry couplant are highly unstable and need further investigation.

Table 25. Thickness Measurements

Sample	Actual	Glycerin	Aqualene	Aqualene with weights	Weight (lbs)	Pressure (Psi)	% error Glycerine	% error Aqualene	% error Weight
Aluminum	0.25”	0.22”	0.29”	0.29”	0.84	6.93	12	16	16
Carbon Steel	0.25”	0.24”	0.31”	0.31”	6.17	50.75	4	24	24
Stainless Steel	0.02”	0.03”	0.16”	0.16”	2.01	16.53	50	700	700

CONCLUSIONS

To accommodate the Tank Farms Waste Transfer System Fitness-for-Service Requirements and Recommendations [1], four floor nozzles from the POR104 valve box in the C-Tank farm at Hanford have been evaluated via ultrasonic thickness measurements. Table 37 provides the type of material transferred, volume transferred, and the diameter of each nozzle.

Table 37. Summary of Jumper Information for the AW-02E Feed Pump Pit Jumpers

Nozzles	Material Transferred	Volume Transferred (Mgal)	Diameter (in)
B, E	Slurry Waste	7.83	2
C, F	Supernatant Waste	7.27	2

Nozzles B and E transferred at least 7.83 Mgal of slurry waste. Nozzles C and F transferred at least 7.27 Mgal of supernatant waste. Average thickness measurements for the sections analyzed for nozzles B, C, E, and F were above the manufacturer's nominal values. Similar trends were observed for the straight sections all four nozzles. Longitudinal averages around the circumference of the pipe had thickness trends that were alternating or oscillatory, but radial averages along the length of the pipe were fairly consistent. Of the three types of components analyzed, the straight sections had the least amount of thickness variation. This was also true for the floor nozzles. The average wall thickness measurements of the straight sections for the four floor nozzles in terms of longitudinal averages did not show any consistency. The radial averages for each of the straight sections were all consistent along the length of the pipe. The elbows showed consistent thickness trends for the four floor nozzles in terms of longitudinal averages. The radial averages for each of the elbows did not show any consistent thickness tends along the length of the pipe.

Currently, potential sensors along with the mounting systems are being examined for the purpose of obtaining real time thickness measurements. Samples of dry couplant materials made of rubbers, silicones and others are being considered for testing with different test pieces using the UT sensors. Additionally, the possibility of in-house manufacturing of certain hydrophilic polymers, to test as dry couplants, is being assessed.

REFERENCES

1. RPP-RPT-52206, 2012, Tank Farms Waste Transfer System Fitness-for Service Requirements and Recommendations, Bechtel Nuclear Services, Richland, Washington.
2. ASTM A312-77, Seamless and Welded Austenitic Stainless Steel Pipe, American National Standards, Institute.
3. ASTM A53-72a, Welded and Seamless Steel Pipe, American National Standards, Institute.
4. PFI Standard EW-24, Pipe Bending Methods, Tolerances, Process and Material Requirements, Pipe Fabrication Institute, New York, New York.
5. ASME B31.3-2012, 2012, Process Piping – ASME Code for Pressure Piping, B31, American Society of Mechanical Engineers, New York, New York.
6. M.L. Nayykar, Piping Handbook, Seventh Edition, McGraw-Hill.
7. RPP-RPT-55812, 2013, Engineering Evaluation of Remote Permanently Mounted Pipe Wall Ultrasonic Thickness Measurement Devices, WRPS, Richland, Washington.

TASK 19.2
EVALUATION OF NONMETALLIC COMPONENTS IN THE WASTE TRANSFER SYSTEM (FIU YEAR 5)

EXECUTIVE SUMMARY

Nonmetallic materials are used in the United States Department of Energy's Hanford Site Tank Farm waste transfer system. These materials include the inner primary hoses in the hose-in-hose transfer lines (HIHTLs), Teflon® gaskets, ethylene propylene diene monomer (EPDM) O-rings, and other nonmetallic materials. These nonmetallic materials are exposed to β and γ irradiation, caustic solutions as well as high temperatures and pressure stressors. How the nonmetallic components react to each of these stressors individually has been well established. However, simultaneous exposure of these stressors has not been evaluated and is of great concern to Hanford Site engineers.

FIU engineers have worked closely with key Hanford HLW personnel to develop an experimental test plan to determine how these nonmetallic components react to various simultaneous stressor exposures. More specifically, the initial phase of testing includes exposure of EPDM components to caustic material at various temperatures for varying lengths of exposure time. After the tests have been conducted and the data analyzed, additional testing phases will be conducted that may include the effects of elevated pressure and the use of different materials (Teflon and Tefzel).

The EPDM material tested will consist of EPDM material coupons, EPDM HIHTL inner hoses and EPDM O-rings. Coupons will be used to obtain a fundamental understanding of the relationship of the stressor with the material. Components (inner hoses and O-rings) will be used to determine the effect on the component being evaluated in an environment similar to its operational environment. The aging of the materials will involve exposing each sample to a NaOH solution at ambient (70^{o}F), operating (130^{o}F) and design temperatures (180^{o}F) for a duration of 60, 180 and 365 days. Tests will be conducted on both material coupons as well as in-service configuration assemblies. After aging/conditioning, the mechanical properties of the samples will again be measured as per ASTM standards.

An experimental test loop has been designed and is currently being assembled. The system can accommodate three coupons for each aging set (3 time lengths and 3 temperatures). Additionally, HIHTL coupons are currently be manufactured by Riverbend. The coupons will be approximately 30 inches in length with 26 inches being HIHTL and 4 inches of end fittings. Aging of the coupons will begin upon receipt from Riverbend.

INTRODUCTION

Nonmetallic materials are utilized in the waste transfer system at the Hanford tank farms; these include the inner hose of the hose-in-hose transfer lines (HIHTLs), Teflon® gaskets and ethylene propylene diene monomer (EPDM) O-rings. These materials are exposed to simultaneous stressors including β and γ radiation, elevated temperatures, caustic supernatant as well as high pressures during normal use. In 2011, the Defense Nuclear Facilities Safety Board recommended to the U.S. Department of Energy (DOE) to conduct post service examination of HIHTLs and Teflon gaskets to improve the existing technical basis for component service life. Suppliers of the nonmetallic components often provide information regarding the effects of some of the stressors, but information is not provided for simultaneous exposure. An extensive test plan was developed by Sandia National Laboratories to understand the simultaneous effects of the aforementioned stressors (1); however, this test plan was never executed. Additional studies conducted by Lieberman provides information on HIHTLs at elevated temperature and pressure but little information is gained regarding the synergistic effects with the caustic supernatant (2). Florida International University (FIU) has been tasked with supporting this effort by conducting multi stressor testing on typical nonmetallic materials used at the Hanford tank farms.

This report provides a description of the test plan for the initial phase of testing which includes exposure of EPDM components to caustic material at various temperatures for varying lengths of exposure time. After the tests have been conducted and the data analyzed, additional testing phases will be conducted that may include the effects of elevated pressure and the use of different materials (Teflon and Tefzel).

EPDM was selected for this phase of testing due to its use in multiple applications within the Hanford waste transfer system. The EPDM material tested will consist of EPDM material coupons, EPDM HIHTL inner hoses and EPDM O-rings. Coupons will be used to obtain a fundamental understanding of the relationship of the stressor with the material. Components (inner hoses and O-rings) will be used to determine the effect on the component being evaluated in an environment similar to its operational environment. Since material properties such as thickness and pressure ratings may vary with each supplier, FIU will work with site personnel to identify these properties and test parameters will be adjusted accordingly.

This report also includes a description of the experimental loop that will be used to age the EPDM material and descriptions of the HIHTL coupons that are being assembled by Riverbend.

TEST PLAN

All material samples will have their mechanical performance and properties tested as per ASTM standards prior to any exposure. Once the baseline properties have been determined, each material sample will be aged, which will involve exposing each sample to a chemical simulant at ambient (70^{o}F), operating (130^{o}F) and design temperatures (180^{o}F) for a duration of 60, 180 and 365 days. Tests will be conducted on both material coupons as well as in-service configuration assemblies. After aging/conditioning, the mechanical properties of the samples will again be measured as per ASTM standards.

Material Aging

The in-service configuration aging experimental setup will consist of 3 independent pumping loops with three manifold sections on each loop (Figure 112). Each of the 3 loops will be run at a different temperature (70^{o}F, 130^{o}F and 180^{o}F). Each manifold section can hold up to three test samples and be used for a corresponding exposure time of 60, 180 and 365 days. Three samples of the EPDM inner hose and three samples of the O-rings will be placed in a parallel manifold configuration. Isolation valves on each manifold will allow removal of samples without affecting the main loop and the rest of the samples. The temperature of the chemical solution circulating within each loop will be maintained at a preset temperature by an electronically controlled heating system. This configuration requires 9 test samples (for both the inner hose and O-rings) for each of the three test loops, requiring a minimum of 27 test samples of each for the inner hose and O-rings. A 25% sodium hydroxide solution will be used as a chemical stressor that will circulate in each of the loops. The chemical stressor will be changed out every 30 days to ensure that the concentration levels remain constant.

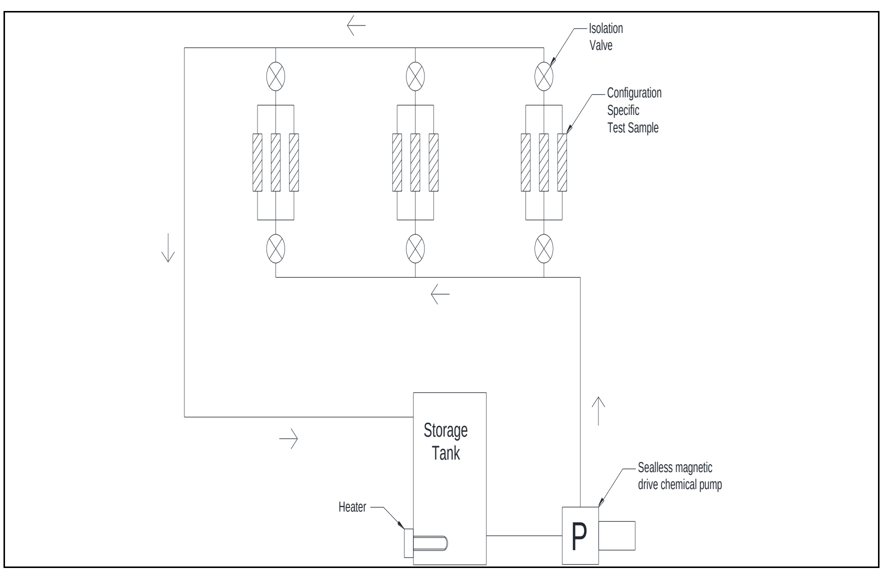

Figure 112. In-service component aging loop.

The coupon aging experiment setup will consist of 3 temperature controlled circulating fluid baths. Each bath will be maintained at a different temperature (70^{o}F, 130^{o}F and 180^{o}F). As in the in-service configuration tests, the circulating fluid will be a 25% sodium hydroxide solution. Each bath will have three racks with ten coupons suspended on each rack. Each rack will be submerged in the bath for a duration of 60, 180 and 365 days. In addition, samples will be tested that are not exposed or aged to generate a set of baseline data. Table 26 shows the test coupon aging matrix.

Table 26. Coupon Aging Matrix

Days Exposure	Ambient Temperature (70^oF)	Operating Temperature (130^oF)	Design Temperature (180^oF)	Baseline
0				10 coupon samples
30	10 coupon samples	10 coupon samples	10 coupon samples	
60	10 coupon samples	10 coupon samples	10 coupon samples	
180	10 coupon samples	10 coupon samples	10 coupon samples	

Quantification of Material Degradation

In order to quantify how each sample was affected by the exposure to the caustic stressor, post-exposure mechanical testing will be conducted. Post-exposure mechanical testing will include hose burst and O-ring leak tests as per ASTM D380-94 and ASTM F237-05, respectively. The tests will be conducted on the 27 aged test samples (9 from each test temperature with 3 at each exposure time). These results will be compared to the baseline mechanical testing results from un-aged samples.

Post-exposure mechanical testing of the coupons will include material property testing as per ASTM standards. Coupon properties to be evaluated include specific gravity, dimensions, mass, hardness, compression set, and tensile properties (tensile strength, ultimate elongation yield, and tensile stress). These properties will be evaluated using standardized test methods developed by ASTM International. For specific gravity measurements, ASTM D792 will be used, while ASTM D543 will be used for measuring dimensions and mass. For hardness measurements, ASTM D2240 will be used and ASTM D412 – Method A will be used for evaluating tensile properties.

Table 27 shows the coupon post exposure test matrix. Each of the sets of 10 coupon samples defined in Table 26 will be used to determine the material property changes described in the 6 tests listed in the table below.

Table 27. Coupon Post Exposure Tests

Test 1	Dimension change (ASTM 543)
Test 2	Specific gravity and mass change (ASTM D792, ASTM 543)
Test 3	Tensile strength (ASTM D412)
Test 4	Compression stress relaxation (ASTM D6147)
Test 5	Ultimate elongation (ASTM D412)
Test 6	Hardness measurements (ASTM 2240)

EXPERIMENTAL TESTBED

FIU efforts during FIU Year 5 (FY14) included design and selection of the experimental flow loop’s main components including the tanks, pumps and heaters. The three tanks, shown in Figure 113, will hold the caustic material at three separate temperatures (70°F, 130°F and 180°F) which will be regulated via thermostatically controlled tank heaters (Figure 114). The tanks will be held in a fume hood and placed on a spill containment skid for health and safety purposes. Three separate loops will be manufactured containing sections of a HIHTLs and gaskets and O-rings. Separate specimens will also be placed directly in the tanks for aging and subsequently tested for degradation of material properties.

Figure 113. Tanks and pumps on spill containment skid.

Figure 114. Thermostatically controlled tank heater.

Additional efforts this year focused on procuring HIHTL specimens. Previous correspondence with Riverbend indicated that their price for the couplings and their installation would be significantly greater than the allowable budget. Various elements such as lower quality assurance of the couplings and the use of carbon steel will reduce the cost significantly. Even with the cost reduction, modifications to the test plan will likely have to be made. The test plan calls for the aging of 27 HIHTL specimens, with approximately 5 additional needed for baseline and initial testing. It is likely that the number of specimens for the 60 day aging will be reduced, with primarily the 180 and 360 day exposures with three operating temperatures. Some specimens may be used at the upper temperature limit for 60 days to determine if 60 days of aging causes any reduction in strength. If so, potential tests in the future could be used to complete the test matrix.

Representatives at WRPS were able to locate a 864 in. HIHTL that will be used to create our specimens (see Figure 1-42). After discussions with representatives from Riverbend, it was decided that FIU will use 26-inch specimens with the fitting adding another 2 inches on each side. The HIHTL sample does have a kink in the line that extends approximately 18 inches which leaves 846 in. of usable line. Although FIU would potentially be able to manufacture 32 specimens from this length, limitations in the budget will allow for only 24 test specimens. FIU has shipped the HIHTL to Riverbend to be cut and fitted with the fittings.

Figure 115. Hanford HIHTL to be used to create test specimens.

After continued discussions with representatives from Riverbend, a quote was finally issued for 24 test coupons with a 2-inch Safe-T-Chem hose with SST, MNPT swaged end fittings. Riverbend will hydro-test each coupon up to 850 psi to ensure integrity. The final length of the specimens will ultimately depend on the usable hose obtained by WRPS.

CONCLUSIONS AND FUTURE WORK

FIU engineers are working closely with Hanford engineers to evaluate nonmetallic components that are subjected to various stressors. A test plan has been developed that includes exposure of EPDM components to caustic material at various temperatures for varying lengths of exposure time. Coupons of the material will be aged to obtain a fundamental understanding of how material properties change. Additionally, EPDM HIHTL specimens, gaskets and O-rings will be aged in system-specific configurations. For both the coupons and the system specific specimens, baseline testing will be conducted and compared with data obtained from the aged specimens.

An experimental test loop has been designed and is currently being assembled. An exemplar HIHTL has been identified and is being used to manufacture a number of specimens that are 30 inches in length. Aging of the specimens will commence as soon as they are received from Riverbend.

After the tests have been conducted and the data analyzed, additional testing phases may be considered. This may include the effects of elevated pressure in addition to elevated temperature and exposure to caustic solutions. Additional material may also be evaluated including the use Teflon and Tefzel.

REFERENCES

1. H Brush, C. O. (2013). Test Plan for the Irradiation of Nonmetallic Materials. Albuquerque, New Mexico: Sandia National Laboratories.
2. Lieberman, P. (2004). Banded (Band-It) and Swaged Hose-In-Hose (HIHTL) Assembly Service Life Verification Program. Santa Clarita, California: National Technical Systems.